國立臺灣大學理學院地質科學研究所

博士論文

Department of Geosciences

College of Science

National Taiwan University

Doctoral Dissertation

利用噪訊成像法以及 Ps 接收函數探究日本東北之地殼構造

Crustal Seismic Structure of Northeast Japan Revealed by

Ambient Noise Tomography and Ps Receiver Functions

陳凱勛

Kai-Xun Chen

指導教授：龔源成 博士、郭本垣 博士

Advisors: Yuancheng Gung, Ph.D.; Ban-Yuan Kuo, Ph.D.

中華民國 109 年 6 月

June, 2020

口試委員會審定書
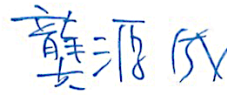
國立臺灣大學博士學位論文
口試委員會審定書

利用噪訊成像法以及 Ps 接收函數探究
日本東北之地殼構造

Crustal Seismic Structure of Northeast Japan Revealed by Ambient Noise Tomography and Ps Receiver Functions

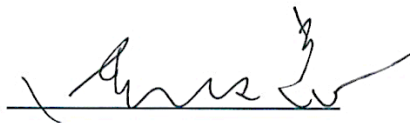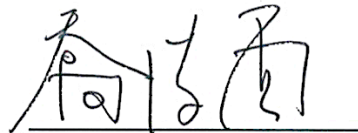本論文係陳凱勛君（D04224005）在國立臺灣大學地質學系、所完成之博士學位論文，於民國 109 年 06 月 23 日承下列考試委員審查通過及口試及格，特此證明

口試委員：

_____ 　_____ 　（簽名）

（指導教授）

_____ 　_____

_____ 　_____

系主任、所長 　_____ 　（簽名）

（是否須簽章依各院系所規定）

i

誌謝

能完成這篇論文並取得博士學位，特別感謝兩位指導教授龔源成與郭本垣老師在五年間的提攜與指導，引領我完成博士學位，在學術、待人處事甚至是人生觀上皆有莫大的幫助。龔老師讓我們在相當自由的學術環境中摸索與嘗試，並適時地提點以激發我們思考，對學生的關心得以讓我在博士班期間放鬆片刻、享受生活。郭老師面對科學議題時的熱愛、解決問題的執著都是令我相當敬佩的，也讓我體會並學習科學家應該具備的思維與能力，時刻提醒我不能滿足於現狀，也因為老師的牽線讓我得以在千里馬期間前往布朗大學與 Karen Fisher、Donald Forsyth 等教授學習，在布朗的一年間我從兩位老師身上看到了他們面對科學議題時的思路與做法，他們以高標準的門檻促使研究的深度與廣度都達到盡善盡美的程度，這難得的經驗無疑大大的影響了我。此外，也感謝梁文宗老師在近十年來的關心，自參與老師的地球所暑期研習計畫後已過許久，但還是能夠時常收到老師的支持勉勵與叮嚀。謝謝洪淑蕙和曾泰琳老師在地震學專題討論時的指點與教導，透過研讀不同領域的文獻後著實擴展了眼界與想像。謝謝喬凌雲老師在逆推和論證方面嚴謹的教導，並且抽空詳細地向我說明。同時也謝謝實驗室每一位成員對我的支持與鼓勵。

學術圈外，我要感謝我的家人長期以來給予的鼓勵，總是提醒我多休息，讓我無後顧之憂地走在選擇的道路上，並且完成學位。謝謝立宸一路以來的陪伴，當我面對挫折與茫然時給予能量與鼓勵。在人生最後的求學階段中，各種挑戰相繼而來，但也因此成長不少，覺得與五年前剛踏進椰林大道相比成熟了不少，感謝一路以來指導過、幫助過我的恩人們。

中文摘要

日本東北是日本各地區當中構造單純的區域，在此地區的研究結果是往後研究其他受板塊隱沒與岩漿活動區域的基石。在這裡，太平洋板塊向西隱沒到歐亞板塊下，島的東側由兩個相當古老的岩塊組成，中間有多座活火山，西側由零星的活火山以及第三紀、第四紀沈積物組成。相較於過去三四十年的研究多著重在地慢的構造，近期受惠於資料品質的提升以及技術方法的演進，地殼尺度的相關研究也逐漸增加中。

我們使用佈設於此區一百個左右 Hi-net 測站之連續噪訊紀錄，計算兩測站間的交相關函數，這些廣佈的高品質測站交織出相當密集的波線路徑，進而將擷取出的基態表面波訊號用於建立高解析的地殼剪力波速度與方位非均向的模型。在三維的剪力波速度模型中，幾乎所有的火山下方都在 5-18 公里的深度間表現出顯著的低速異常，而在 9-13 公里深的速度異常更是可以高達將近-10%。而三維的非均向性模型顯示日本東北的地殼是由兩個不同的變形機制所構成，其中淺部 5 公里的快方向主要為南北向，平行島嶼走向，推斷是岩石受應力後而產生的排列方式；20 公里以下的快軸主要是東西向的板塊聚合方向，成因可能是受到在地慢楔因隱沒的二維地慢楔流場所帶動的剪力所導致；另一種成因可能是這地區在上一次的日本海張裂時期就已經形成並冷卻殘餘留下的非均向性；在這兩層之間的非均向性則呈現強度減弱、快方向排列不一致的結果，顯示火山下方的震波速度明顯受到火成活動影響。

另外，遠震的接收函數也被用來探討地殼內不連續面的分佈與可能的成因，在分析將近 15 年總計約 1800 個的遠震資料後，我們發現接收函數中負相位的訊號

多集中在火山附近約 8-10 公里深，先前的研究多將這類訊號歸因於地殼內的非均向性，不過我們在反覆確認計算結果、並利用合成波型來測試後，發現單純用地殼內非均向性來解釋所觀察到的負相位強度是遠遠不夠的，同時，這些負相位訊號在我們的剪力波速度模型上正巧是處於低速異常的上邊界，意味著該處可能是因為火山熔體堆積在整個儲集區的頂部而產生的速度下降，經計算後得知約有 5~10% 的熔體含量，而零星分佈在下部地殼的負異常訊號可能是反應另一個較深處熔體儲集區的上邊界。

以上兩個研究使用了地震學中不同的分析方法，不但能夠相互驗證與解釋，與火山構造的吻合也將單純的速度分佈賦予了火山構造的含義，使我們對這地區的地殼構造能夠有進一步的認識。

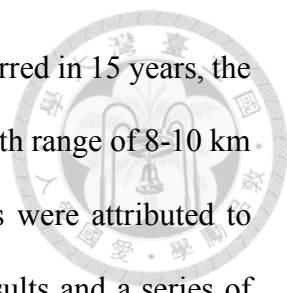關鍵字：日本東北、周遭噪訊層析成像、地殼速度、地殼非均向性、分層變形、熔體儲集區、接收函數、速度降、熔體含量

ABSTRACT

Northeast Japan, or the Tohoku region, is the "simplest" area in Japan archipelago for fundamental study of subduction-magmatism system that will be the basis for the other similar regions. Here, the Pacific plate westward subducts beneath the Eurasian plate, the east two mountains are composed of Cretaceous rocks, and Holocene arc volcanoes dominate in the central belt and lie more sporadically in the west. The seismic structure of Tohoku, particularly in the mantle was broadly investigated in the past few decades. In contrast, crustal-scale study is increasing in recent years, contributing to the improvements in data quality and analysis method.

In the first part of this thesis, continuous records from 123 Hi-net stations were used to construct cross-correlation functions between each potential station-pair. These high-quality, widely-deployed borehole stations yield a data set of fundamental-mode surface wave with a dense path coverage, allowing us to simultaneously inverts for high-resolution shear velocity and azimuthal anisotropy crustal models. In the Vs structure, under most of the active volcanoes, low velocity zones are more common in the upper crust and are strong at a depth of 9-13 km with anomaly up to -10%. In azimuthal anisotropy, a crustal two-layer pattern is resolved, which a near N-S, island-parallel fast direction in shallow 5 km depth that may map structural fabrics of crustal deformation, and a near E-W, convergence-parallel fast direction in lower crust that may result from shearing either imposed by the return flow in the mantle wedge or frozen-in from the last stage of extension of the continental margin. Between these two layers, coherent crustal fabrics collapse and anisotropy turns to a chaotic state, suggesting that continuous volcanic activities disrupt the otherwise consistent fabrics.

In the second part of this thesis, Ps receiver functions were used to investigate crustal

discontinuities and their origins. From ~1800 teleseismic events occurred in 15 years, the calculated receiver functions show prevalent negative phases at a depth range of 8-10 km near the active volcanoes. In a previous study, the negative phases were attributed to crustal azimuthal anisotropy. However, after a closer look at the results and a series of tests with synthetic seismograms, we inferred that azimuthal anisotropy is insufficient to explain the strong negative phases. These pronounced phases correlate well with the upper margins of low velocity zones beneath volcanoes, which this feature is consistent with model for crustal melt storage where the highest concentrations of melt are localized at the top the mush column, implying a 5-10% melt fractions across the Tohoku. Some groups of deeper negative Ps phases may reflect the upper boundary of melt storage at greater depths.

In this thesis, observations from ambient noise tomography and Ps receiver function could explain well with each other and correlate well with surface geology that provides seismic velocity more implication in volcanic structure, letting us move forward in crustal structure of Tohoku.
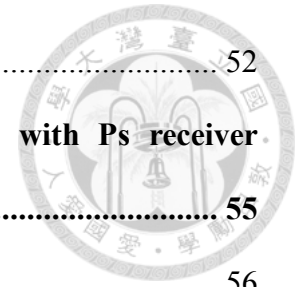

Keywords: Northeast Japan, ambient noise tomography, crustal shear velocity, crustal azimuthal anisotropy, layered-deformation, melt storage, Ps receiver function, velocity drop, melt fraction

Table of Contents

LIST OF FIGURES

Chapter 1 Introduction

The Japanese archipelago which lies within the Pacific ring of fire suffers from frequent earthquakes and magmatic activities that seriously endanger human life. To monitor such natural hazards, several dense and high-quality seismic arrays, for example, F-net, Hi-net, and V-net were deployed in the whole archipelago. These data are not only for the early warning but also allowing us to decipher seismic structure beneath this place.

Northeast Japan, or the Tohoku region, is the "simplest" area in such a tectonically complex area for fundamental study of subduction-magmatism system that will be the basis for the other similar regions. Here, the Pacific plate westward subducts beneath the Eurasian plate with a speed rate of 8-9 cm/yr and Holocene arc volcanoes dominate in the central belt and lie more sporadically in the west. In northeastern and southeastern Tohoku, the Kitakami and the Abukuma mountains are composed of Cretaceous sedimentary and plutonic rocks. The seismic structure of Tohoku was broadly investigated in the past few decades, particularly in the mantle. In contrast, crustal-scale study is increasing in recent years, contributing to the improvements in data quality and analysis method.

In the first part of this thesis, both crustal shear velocity and azimuthal anisotropy in Tohoku are investigated for crustal magmatism and deformation fabrics by ambient noise tomography (ANT) method. Comparing to traditional body-wave travel-time tomography, this popular method that benefits from short-to-intermediate period surface wave dispersion improves constraint in crustal resolution.
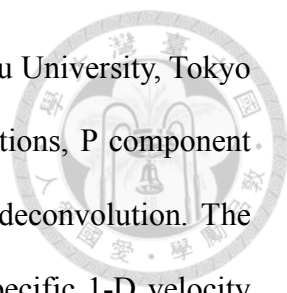
Here, continuous record from 123 NIED Hi-net stations were used to construct empirical Green's functions (EGFs) between each potential station-pair, and then Rayleigh wave dispersions measured in 3-16 s period from these provide a data set with

1

a very dense path coverage, allowing us to resolve high-resolution crustal structure by a 3-D, one-step, wavelet-based multiscale inversion that simultaneously inverts for both shear velocity and azimuthal anisotropy models.

The resolved structure shows prevalent low velocity zones with anomaly up to -10% at a depth of 9-13 km beneath most of the Holocene volcanoes in the central belt and the west, suggesting that magmatism affects the upper crust. In contrast, in northeastern and southeastern Tohoku the Kitakami and Abukuma mountains composed of Cretaceous sedimentary and plutonic rocks both show high anomalies in the whole crust. In crustal azimuthal anisotropy, a two-layer pattern is resolved, which a near N-S, island-parallel fast direction in upper crust that may map structural fabrics of crustal deformation, and a near E-W, convergence-parallel fast direction in lower crust that may result from shearing either imposed by the return flow in the mantle wedge or frozen-in from the last stage of extension of the continental margin. Between these two layers, at a depth of 5-15 km, where melt storages are thought to reside, coherent crustal fabrics collapse and anisotropy turns to a chaotic state, demonstrating that continuous volcanic activities and magma ponding disrupt the otherwise consistent fabrics. This work has been published on Journal of Geophysical Research at 2018 (Chen et al., 2018) and is introduced in Chapter 2.

In the second part of this thesis, crustal structure related to melt storage was investigated from Ps converted waves across Tohoku. The converted body wave phases have potential to image localized vertical velocity gradients, comparing to velocity model from body wave or surface wave dataset. A better understanding of structure and behavior in crustal magmatic systems, particularly in upper crust, is key to deciphering the last stages of magma evolution and transport before volcanic eruption.

We collected 1773 teleseismic event data that occurred from October 2004 to July 2018 recorded by 127 permanent stations maintained by multiple seismic networks

2

(including NIED Hi-net, JMA volcanic seismometer network, Tohoku University, Tokyo University, and Hirosaki University). To calculate Ps receiver functions, P component was deconvolved from SV component with iterative time-domain deconvolution. The resulting receiver functions were migrated to depth using station-specific 1-D velocity model that incorporated a number of geophysical observations, including seismic reflection survey, shallow earthquake travel-time data, previous receiver function result, regional body wave tomography, and ambient noise tomography. Then, both positive and negative phases on the migrated receiver functions were extracted to decipher their origins by collaborating with crustal shear velocity model.

In northeastern and southeastern regions, the Cretaceous mountains show that negative phase amplitudes are typically small or phases are absent at depths of 5-15 km. In contrast, in central and western Tohoku, negative Ps phases are prevalent at a depth range of 5-10 km and correlate with the upper margins of localized low velocity zones beneath volcanoes, which this feature is consistent with model for crustal melt storage where the highest concentrations of melt are localized at the top the mush column. For these negative phases, waveform modeling of Ps receiver function indicates a variation in shear velocity drop at depths of 5-10 km, implying a variety of melt fractions across the Tohoku. The geographic distribution of apparent melt fraction suggests that in some cases the same upper crustal source can supply multiple adjacent volcanoes, and in a few other high melt fraction zones are significantly laterally offset from the nearest volcano. This work has been published on Earth and Planetary Science Letters at 2020 (Chen et al., 2020) and is introduced in Chapter 3.

4

Chapter 2   Crustal Magmatism and Deformation Fabrics in Northeast Japan Revealed by Ambient Noise Tomography

Mapping both isotropic and anisotropic velocity structures of the crust provides insight into the dominant mechanisms that produce the deformation. We performed ambient noise tomography for shear velocity Vs in the Tohoku region, Japan, where plate kinematics remains simple as the Pacific plate is subducting under the Okhotsk plate. Cross-correlation functions were retrieved from Hi-net recordings and phase velocities of 3-16 s were measured, followed by a one-step, wavelet-based multiscale inversion for both Vs and its azimuthal anisotropy. The isotropic model shows that high Vs anomalies underlie the Cretaceous aged Kitakami and Abukuma Mountains from shallow crust to lower crust. Low Vs is found to track the active volcanoes with the strongest anomalies concentrated at roughly 10 km depth, which we interpret as the shallow magma reservoirs of the Quaternary magmatic system. The resolved azimuthal anisotropy exhibits a switch of anisotropy in the upper crust from island-parallel to a random or suppressed state in 5-15 km depth interval, and back to island-parallel. The island-parallel fast direction may map the structural fabrics of the crustal deformation, and the spatial correlation between velocity and anisotropy patterns suggests that continuous volcanic activities and magma ponding disrupt the otherwise consistent fabrics in the upper crust. Below 20 km depth, the anisotropy turns to convergence-parallel, which may result from shearing either imposed by the return flow in the mantle wedge or frozen-in from the last stage of extension of the continental margin that opened the Sea of Japan. This abstract and the following subchapters are from Chen et al. (2018).

5

2.1 Introduction

The Japanese archipelago stretches over a convergent boundary zone in the northeast Asian continent involving multiple plates, i.e., the Pacific, the Okhotsk (North American), the Eurasian, and the Philippine Sea plates (Figure 2.1). The transpression, accretion, and magmatism due to the interactions among these plates have continuously deformed the crust of the Japan islands and changed its composition and structures. During the opening of the sea of Japan basin since 20 Ma that has eventually settled the islands in its current position, these plate boundaries have evolved drastically with crustal block rotation, plate boundary migration and opening of new oceanic basins (Jovilet et al., 1994; Taira, 2001). The oblique subduction of the Pacific plate under the Kuril trench created the Hidaka collision zone in Hokkaido (Komatsu et al., 1989), and the collision of the Izu-Bonin arc with the Honshu resulted in the Izu collision zone in central Honshu. The latter event together with the oblique subduction of the Philippine Sea plate under the Nankai trough activated the right-lateral slipping Median Tectonic Line (Kaneko, 1966; Fitch, 1972) which runs from central Honshu southward to Kyushu (e.g., Taira, 2001). Northern Honshu, or the Tohoku region, however, has remained relatively simple in plate kinematics and subduction process and free from the large-scale collisions to the north and south. In this region, the Pacific plate subduction has remained steady since 17 Ma (Kano et al., 1991). At present, the normal subduction is taking place at a rate of ~8–9 cm/yr. Tohoku is an ideal venue for the study of the fundamental processes of the subduction-magmatism system.
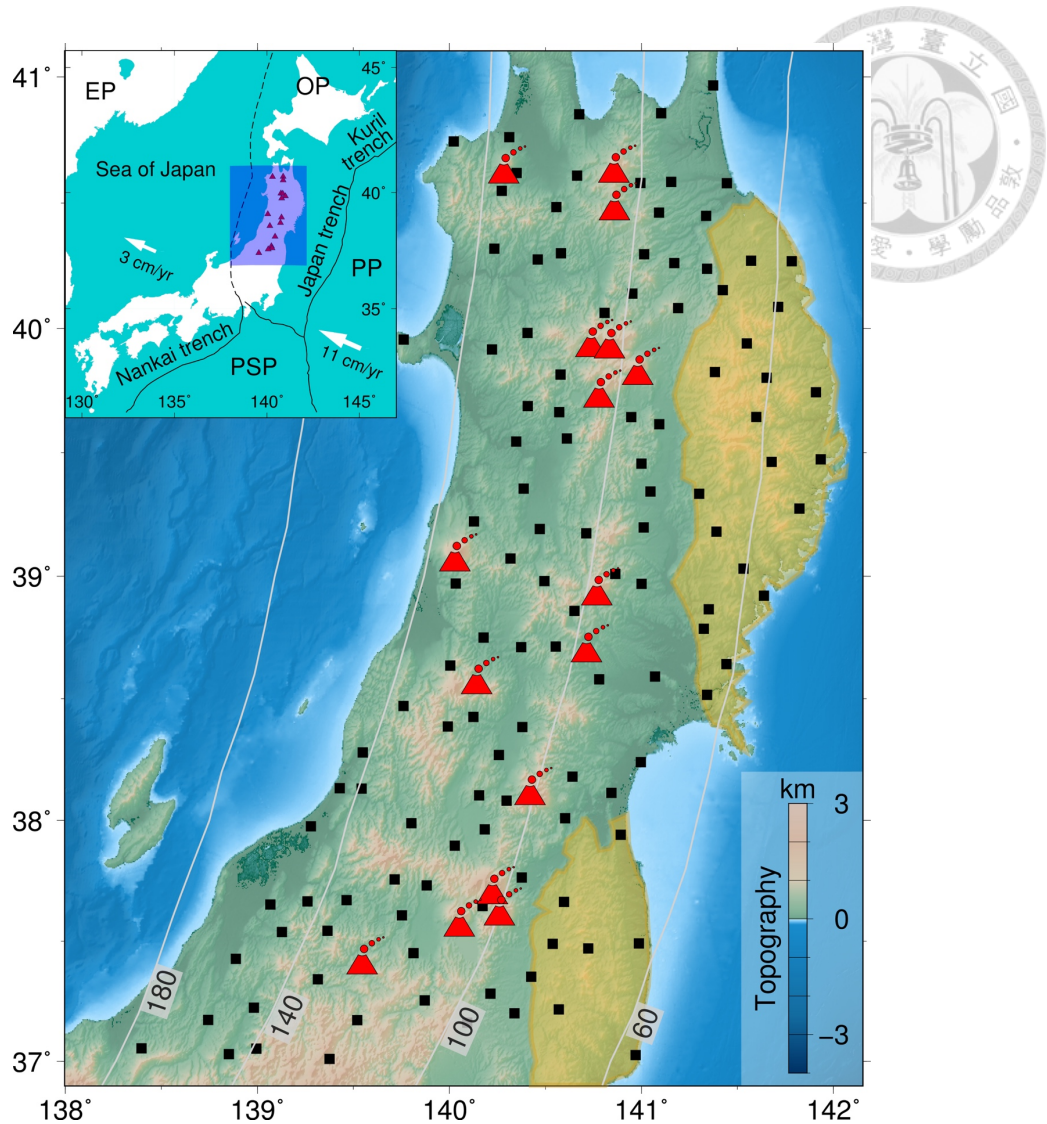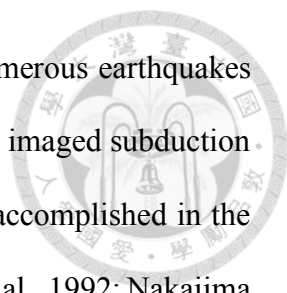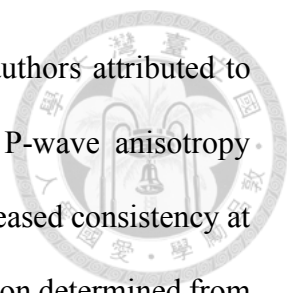
Figure 2.1. The Tohoku region and the relevant tectonic elements. Quaternary active volcanoes are denoted by red triangles. Depth contours in km of the Pacific slab are adopted from Zhao et al. (1997) and Zhao et al. (2012). Black squares denote NIED Hi-net stations (Obara et al., 2005) used in this study. Two yellow semitransparent patches along the east coast are the Kitakami and the Abukuma mountain ranges composed of Cretaceous sedimentary and plutonic rocks. In the inset, the Pacific plate (PP), the Okhotsk plate (OP), the Eurasian plate (EP) and the Philippine Sea plate (PSP) are labelled. The Okhotsk-Eurasian plate boundary is denoted by dashed line. Arrows in white indicate absolute plate motion vectors of the Pacific plate and the Eurasian plate (DeMets et al., 2010).

Aided by the existence of high density seismic stations and numerous earthquakes in the subducting Pacific slab, the Tohoku region is arguably the best imaged subduction system in the world celebrated with many fundamental discoveries accomplished in the past that bear global significance (e.g., Hasagawa et al., 1978; Zhao et al., 1992; Nakajima et al., 2001; Hasagawa and Nakajima, 2004; Zhao et al., 2015). For the crust part of Tohoku, regional-scale, P- and S-wave tomography illustrated the spatial correlation between low Vs and the present-day arc or the volcanic front (Zhao et al., 1992; Nakajima et al., 2001; Zhao et al., 2015). While the low Vs anomalies can be linked from the mantle wedge all the way to the volcanic activities on the surface, the resolution of these models is not high enough to establish detailed Vs -volcano spatial relationship in the crust. In contrast, Nishida et al. (2008) presented ambient noise tomography with short-period tiltmeter data that clearly depicts low Vs patches correlated with active volcanoes. A similar approach using longer period data also demonstrates similar features of volcanoes clustering around low Vs (Guo et al., 2013). Both of these models show that the Mesozoic mountains on eastern Tohoku is underlain by high Vs.
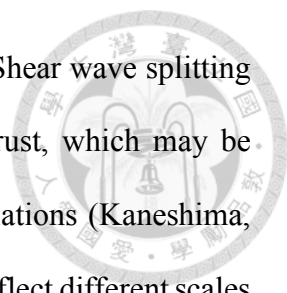
The anisotropy properties of the crust or mantle provide a means to infer the dominant mechanisms of deformation. Shear-wave splitting for slab events in the Tohoku region show fast polarization directions ϕ rotating from trench-parallel in the forearc (east of the active volcanoes) to convergence-parallel in the back arc (west of the active volcanoes) (e.g., Nakajima and Hasagawa, 2004; Nakajima et al., 2006). Larger-scale Rayleigh wave inversion bolsters this pattern in the mantle wedge (Liu and Zhao, 2016), supporting the hypothesis that the lattice-preferred orientation (LPO) of A-type and B-type olivine, respectively, aligned by the shear flow driven by subduction is the main mechanism (Karato, 2008). Compared with the pattern revealed using slab events, the anisotropy of the upper crust is much less systematic, with a more or less trench-parallel

8

ϕ dominating the fore arc region (Iidaka et al., 2013), which the authors attributed to accumulated extensional stress in the upper crust. Similarly, the P-wave anisotropy tomography displays trench-parallelism in the forearc crust with increased consistency at depths (Wang and Zhao, 2013). In the shallowest crust, the fast direction determined from interferometry between surface and borehole data is convergence-parallel in a remarkably systematic fashion throughout middle-northern Honshu, with no distinction between backarc and forearc (Nakata and Snieder, 2012). This near-surface anisotropy is likely controlled by the cracks opened by the compressional stress associated with the plate convergence (Crampin and McGonigle, 1981). This is very similar to the results from the coda-wave interferometry in western Taiwan (Chen et al., 2017).

While it is well known that slab events detect integrated effect of mantle wedge, lithosphere, and the crust, it is difficult to isolate crustal anisotropy by independently sampling the entire crust due to the sparsity of earthquakes in the lower crust. Huang et al. (2011a) took advantage of the low-frequency earthquakes in the lower crust to separate crustal and mantle anisotropy. The authors reported that ϕ in the lower crust is roughly NE-SW, and ultimately inferred that the uppermost mantle is dominated by convergence-parallel ϕ caused by the return flow. This tacitly assumes that the shear flow that generates LPO in the mantle wedge (Katayama, 2009) is extended from the asthenosphere to the top of the mantle lithosphere of the overriding Okhotsk plate. This scenario may be critical to the interpretation of this study but remains to be tested independently.
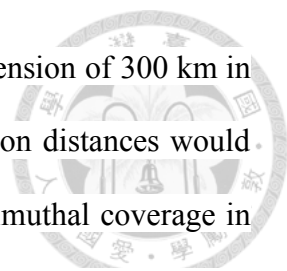
To better characterize the deformation of the crust of Tohoku, both isotropy and anisotropy are required. The former reflects thermal or compositional effect and the latter delineates the deformation fabrics, both linked to tectonic and magmatic evolution. As described above, despite that the earthquake-receiver combination in both number and geometry is favorable in the Tohoku region, tomographic imaging and shear wave

9

splitting measurements have been conducted separately in the past. Shear wave splitting observations have shown scattered patterns of anisotropy in the crust, which may be derived from layering of distinct fabrics and small-scale lateral variations (Kaneshima, 1990). The frequency-dependency of splitting parameters proves to reflect different scales of deformation at different depths (Huang et al., 2011b), which implies a depth sensitivity. In this study, we perform tomographic inversion simultaneously for both Vs and its azimuthal anisotropy for the crust of the Tohoku region from Rayleigh waves. To circumvent the restriction from earthquake-station pairing and to focus sensitivity on the crust, we employ ambient noise tomography that has proven effective in providing improved constraint on crustal structures (e.g., Shapiro et al., 2005; Yang et al., 2008; Huang, Gung, et al., 2015). From this tomographic model, the relationship between Vs anomalies, azimuthal anisotropy, and volcanic activities are examined in the context of the subduction-magmatism tectonics in the Tohoku region.

2.2 Data and Method

The vertical component, continuous records in the year 2006 from Hi-net stations were used to construct the empirical Green's function (EGF) data set. The Hi-net stations, maintained by National Research Institute for Earth Science and Disaster Resilience (NIED), are equipped with short-period velocity sensors with natural frequency at around 1 Hz and deployed in boreholes with depths at least 100 m from the surface to suppress the interference from culture noise (Obara et al., 2005). There are about 800 Hi-net stations in Japan, and 123 of them are distributed in the Tohoku region. With these 123 stations, we are able to construct a data set with very dense path coverage of short to intermediate period surface waves, which allows us to resolve high resolution models for both Vs and Vs azimuthal anisotropy. In this study, not all possible station pairs in the

10

Tohoku region were considered. Because the study region has a dimension of 300 km in the E-W direction and 600 km in the N-S direction, long inter-station distances would preferentially align in the N-S. To maintain overall homogenous azimuthal coverage in the inversion for Vs azimuthal anisotropy, only those station pairs with inter-station distances shorter than 300 km were analyzed.

As the vertical component of the data is used to derive the cross-correlation functions (CCFs), the major signals in the resulting EGFs are dominated by fundamental mode Rayleigh waves (e.g., Shapiro et al., 2005). To prepare the EGFs, we adopted the procedure used in Chen et al. (2016a, 2016b). The Welch's method (Seats et al., 2011) was implemented to improve the EGF quality. In this procedure, each daily record is partitioned into 440-1280 s long segments, based on the criterion that inter-station distances are at least three times of the wavelength of interest (e.g. Bensen et al., 2007). 90% of each segment is overlapped with the adjacent segment in the daily record. To avoid the resulting EGFs from being biased by the unwanted signals, e.g., large earthquake signals or instrument glitches, segments with root-mean-square amplitude larger than 1.1 times of that of the corresponding daily record are removed first. The CCFs were then calculated for all possible combinations of two segments before being stacked to yield the daily CCF. The cross correlation was performed in frequency domain with spectrum whitening. Taking the stack of all daily CCFs as the reference CCF for each station pair, we calculated the correlation coefficients between each daily CCF and the reference CCF, and only those daily CCFs with correlation coefficients larger than 0.5 are retained. This routine deleted about 11% of the daily CCFs. The remaining CCFs were stacked and folded to generate the EGF for each station pairs. The binning stacks of CCFs used in this study are shown in Figure 2.2.
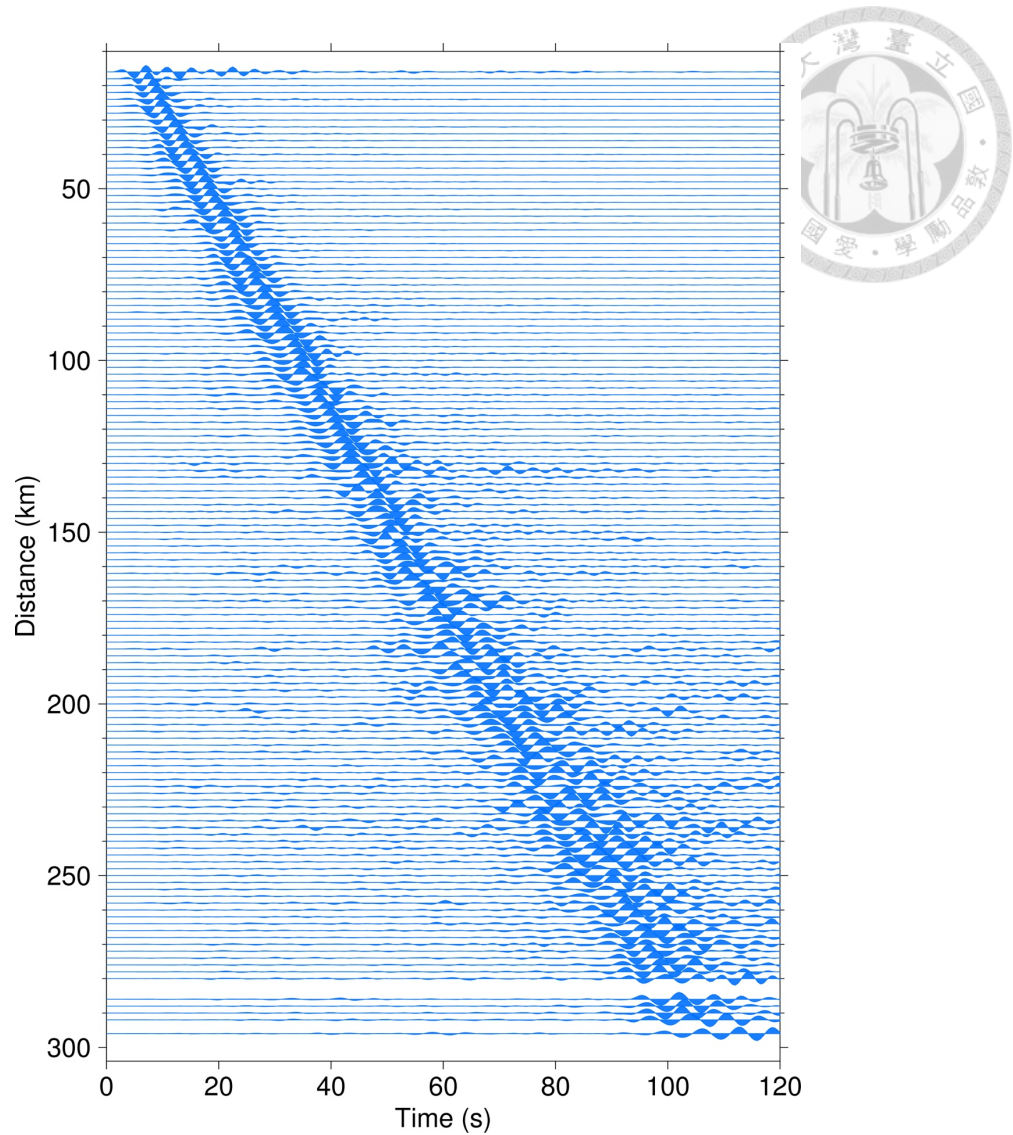
Figure 2.2. Binning stacks of the 4635 cross-correlation functions (CCFs) used in this study. The bin width is 2 km, and the traces are band-pass filtered between 3 and 16 s. These stacks show arrivals of seismic energy, rather than details of waveforms, because CCFs with similar inter-station distances sampling different regions are stacked in each bin.

We applied the frequency-time analysis (e.g., Levshin et al., 1989) to measure the dispersion of phase velocity in the period range from 3 to a maximum of 16 s. Because the Hi-net data are short-period, it is difficult to obtain high-quality measurements at

12

longer periods. The 3 – 16 s period range is determined from an investigation of the signal to noise ratio (SNR) to sort out the range in which the SNR ratio is greater than 5. The SNR is calculated as the maximum amplitude of the envelope of the CCF between 4 km/s and 1 km/s divided by the root-mean-square amplitude of the envelope of the segment of the same length at the end of the daily CCF. The SNR criterion sorted out 4635 continuous dispersion curves between 3 and 16 s, from which phase velocities at discrete periods of 3, 6, 10, and 16 s were selected for the inversion to 3D Vs model. There are 2242, 3873, 3365, and 1933 phase velocity data for these periods, respectively. Figure 2.3 illustrates the spatial distribution of phase velocities along inter-station paths at 3, 6, and 16 s period.
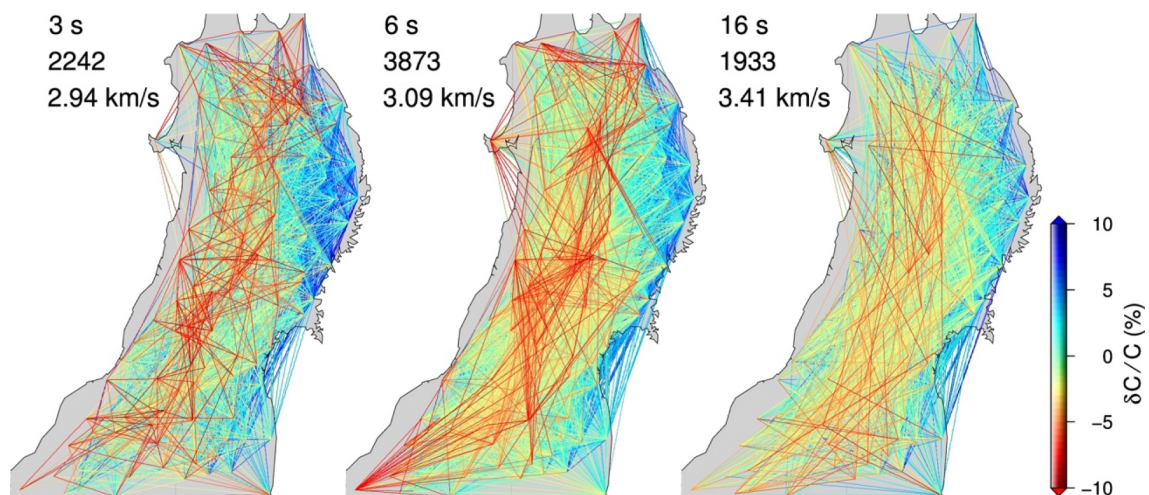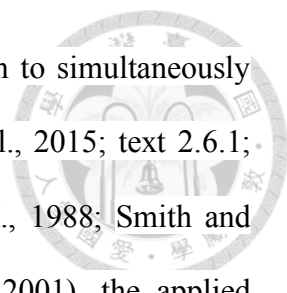
Figure 2.3. Examples of interstation paths and the along-path phase velocities used in the ambient noise tomography for periods of 3, 6, and 16 s. Shown on the upper left of each panel are the period, number of paths, and the average phase velocity for each period. The along-path phase velocities are color coded based on the scale on the lower right. The first order feature from this plot is the high Vs (blue) associated with the mountains in eastern Tohoku and the low Vs (red) along the arc area. Note that in northernmost Tohoku the EW-oriented paths are sparse so that the Vs at depth lacks sufficient constraints (also see checkerboard test in Figure A.3).

13

We perform a 3D, one-step, wavelet-based multiscale inversion to simultaneously invert for Vs and azimuthal anisotropy models (Huang, Gung, et al., 2015; text 2.6.1; Lawson and Hanson, 1974; Montagner and Nataf, 1986; Saito, M., 1988; Smith and Dahlen, 1973). In this multiscale tomography (Chiao and Kuo, 2001), the applied regularization will sort through the successive scales depending on the local data constraints and automatically achieve data-adaptive, spatially varying optimal resolution. Thus, both spatial localization and non-stationary model smoothing are assured (Chiao and Kuo, 2001). This technique has been applied to tomography on global scale (Chiao et al., 2006), plate scale (Gung et al., 2009) and regional and local scales (Chiao et al., 2010; Hung et al., 2011; Huang et al., 2012; Huang, Gung, et al., 2015; You et al., 2010).

In this study, the models are parameterized laterally using the wavelets up to degree (level) 7 in horizontal directions, for which the minimum resolution length is about 6 km (Figure 2.4). For the vertical parameterization, the JMA 2001 1-D velocity model (Ueno et al., 2002) were simplified into a 13 layered starting model, each spanning the depth range of 0-1, 1-3, 3-5, 5-8, 8-12, 12-16, 16-20, 20-24, 24-29, 29-34, 34-41, 41-51, and 51-66 km (Figure 2.5), but in the following we only present results of 9 layers between 1 and 34 km depth. Five iterations were conducted from this starting model with the depth sensitivity kernels updated at each iteration and damping weakening progressively. Following Huang, Gung, et al. (2015), anisotropy was introduced into the inversion at the fifth iteration.
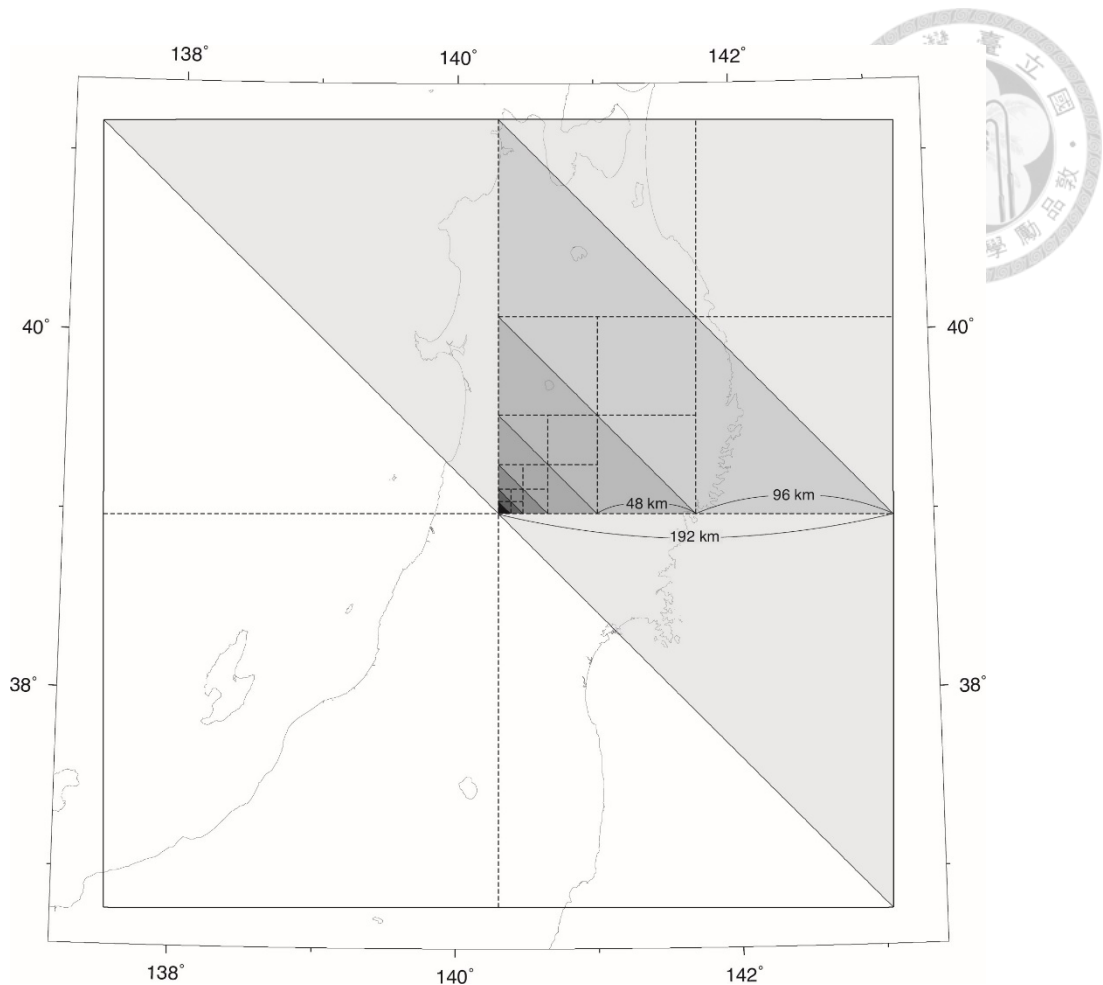
Figure 2.4. Illustration of the wavelet-based multiscale parameterization of the study region. The parametrization is node-based, with continuous velocity across the right-angle triangle (solid line) interpolated from the 3 nodes. Level 1 consists of two triangles on the upper right (lightly shaded) and lower left corner of the largest rectangle. The way how a rectangle is divided into two triangles is not critical because when more levels are added any artificial boundary will be modified and smoothed by the actual data coverage. Progressively smaller triangles for levels 2 – 7 are represented by shades with increasing tones. Grid spacings of 192, 96, and 48 km are illustrated for levels 2, 3, and 4, respectively, as example. The smallest spacing is 6 km for level 7. Triangles unsampled will remain a zero velocity perturbation, making no contribution to smaller scale features. Details of how the wavelet coefficients are constructed from the triangle scheme can be found in the references listed in the text 2.2.

15
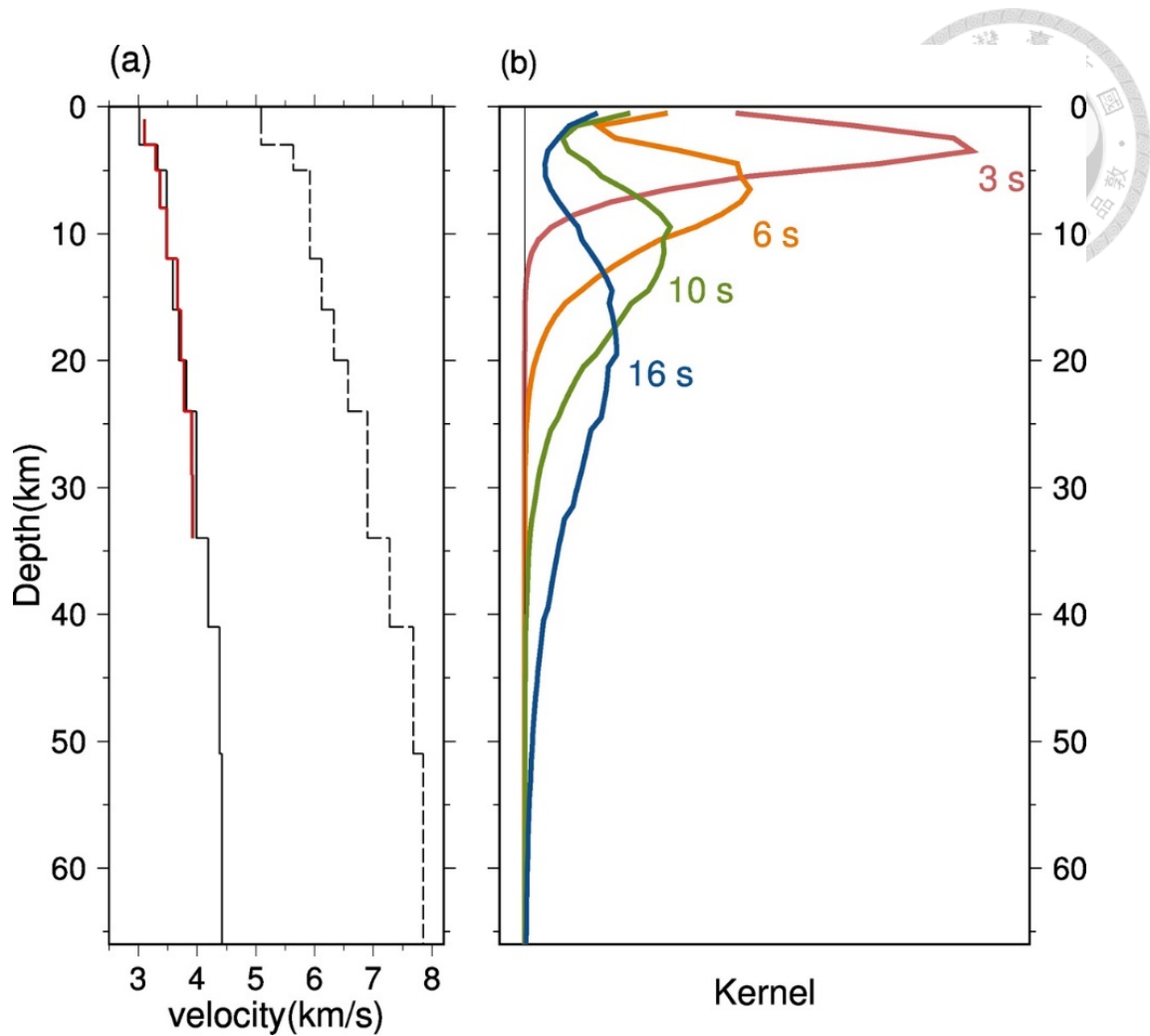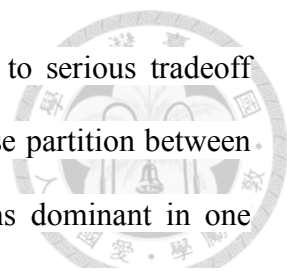
Figure 2.5. (a) JMA2001 1-D velocity structure (Vs: solid line; Vp: dashed line), interpolated to the layering of our model as the initial model. There are 13 layers in the model, but only the layers spanning the depth range of 1-3, 3-5, 5-8, 8-12, 12-16, 16-20, 20-24, 24-29, and 29-34 are shown from the study. The average Vs of these 9 layers from the final model are denoted by red solid lines. (b) Sensitivity kernels for 3, 6, 10, 16 s periods for the initial model. These kernels will be used in the inversion and updated in each iteration. The JMA model does not have a Moho discontinuity, and Figure 2.11 demonstrates that the surface wave model is insensitive to the presence of the Moho discontinuity.

16

Poor azimuthal coverage of Rayleigh wave paths could lead to serious tradeoff between isotropy and anisotropy components of the model. The false partition between these two components usually occurs in regions sampled by paths dominant in one direction so that heterogeneity can be misinterpreted as anisotropy and vice versa. This is hardly the case for the Tohoku region, and, as a reference, the Taiwan orogen. Our experience in Taiwan through vigorous tests (Supplementary Materials of Huang, Gung, et al., 2015) demonstrates that the spatial and azimuthal variations of Vs can be distinguished with confidence in the ambient noise tomography. In the Tohoku region, the area is slightly larger but the station coverage is considerably denser and more even geographically than in Taiwan. In this study, the recovery test (text 2.6.2, Figures A.1 and A.2) and the bootstrap test (Figure A.5) demonstrate that the anisotropy part can be recovered with the isotropic Vs coexisting. Furthermore, we calculated a model with anisotropy entering the inversion at the third iteration, where the isotropic model has not taken its final shape. The patterns of Vs and anisotropy between this test model and that who let the isotropic component fully develop without a chance of tradeoff until at the last iteration are essentially the same except the strength of anisotropy in the former is slightly larger. We thus concluded that the tradeoff between the anisotropy and isotropy components of our model for the Tohoku region is insignificant.

2.3 Results

Figure 2.6 shows the 3D Vs perturbation $\delta V_s/V_s$ and azimuthal anisotropy model for model layers from 1 to 34 km depth (see Figure 2.7 for the absolute-value model). The theoretical background for the multiscale inversion has been discussed in the work cited above. Here we demonstrate graphically how different scales of perturbation, parameterized by different degrees (levels) of wavelets, are synthesized towards the final

17

result. We take the 8-12 km layer as example because it hosts pronounced anomalies. In Figure 2.8a, the model evolves rapidly at lower levels and incrementally as approaching level 7. The multiscale model we used is node-based, and the velocity is continuous inside the triangles at each level. The model differences between the last four levels are illustrated in Figure 2.9 and the variance reduction in Figure 2.10. Figure 2.8b illustrates how the model takes shape with updated kernels through iterations. The variance reduction at each step of iterations increases as 20, 40, 50, 55, and 56%, respectively.

18
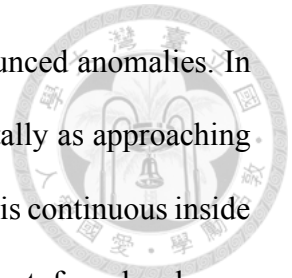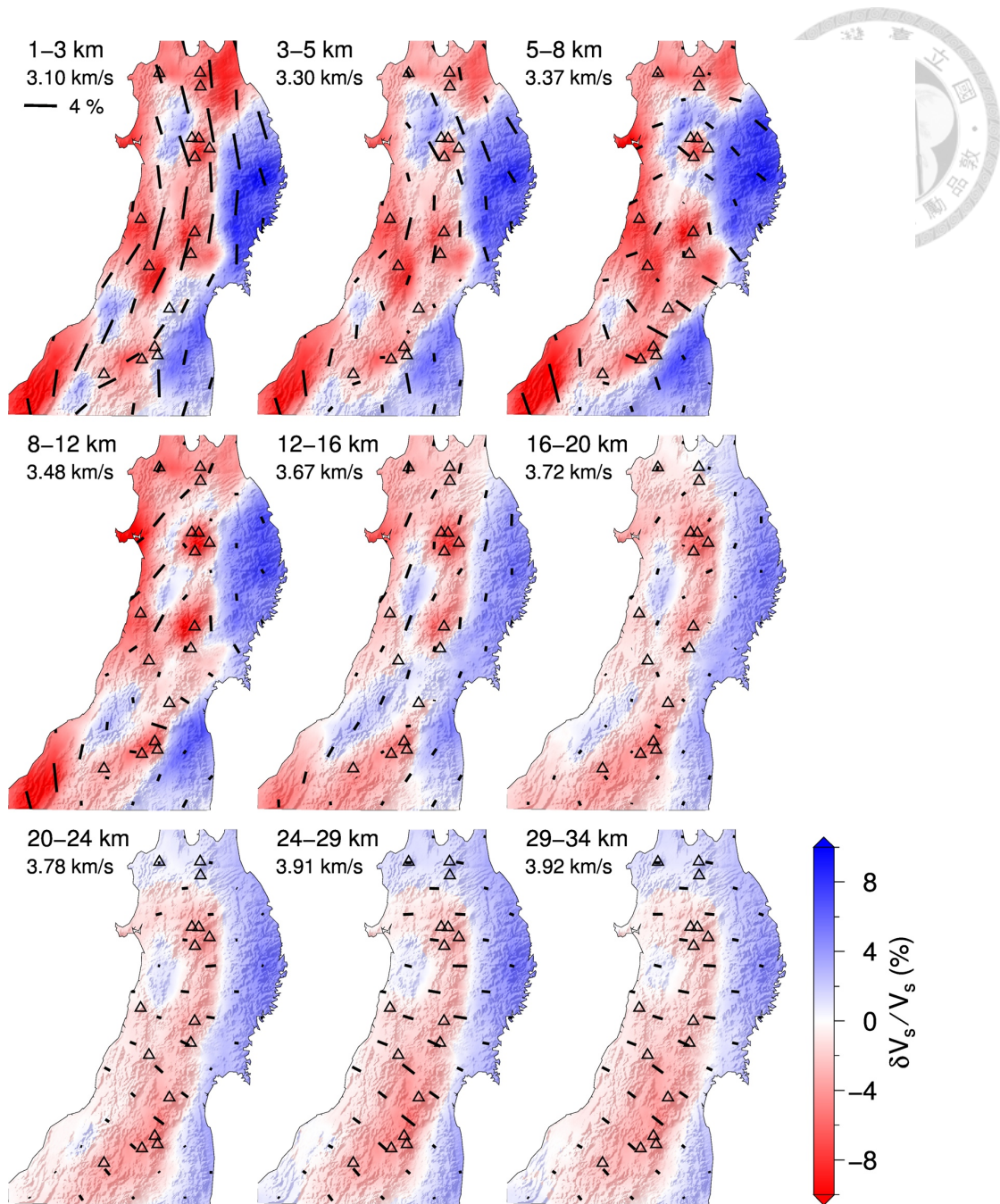
Figure 2.6. δVs/Vs and the azimuthal anisotropy models of this study. The depth range and average Vs of each model layer are shown on the upper left of each panel. Scale of the strength of anisotropy is shown in the upper left panel. Short bars on the map indicate the azimuth of the fast direction of anisotropy with the length proportional to the strength of anisotropy (%). Color scale for Vs perturbation are shown on the lower right of the figure.

19
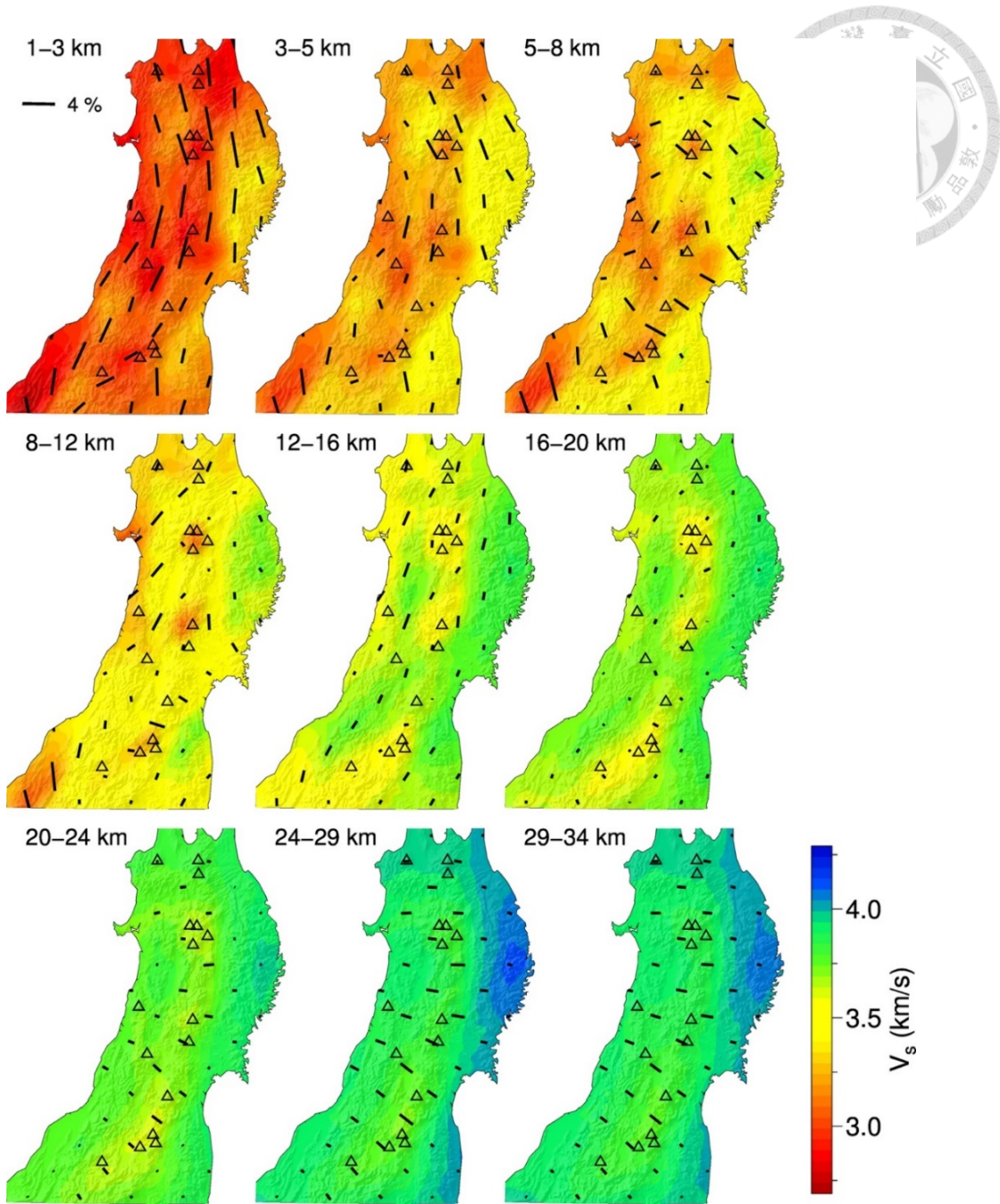
Figure 2.7. The same as Figure 2.6 except for Vs in absolute value.
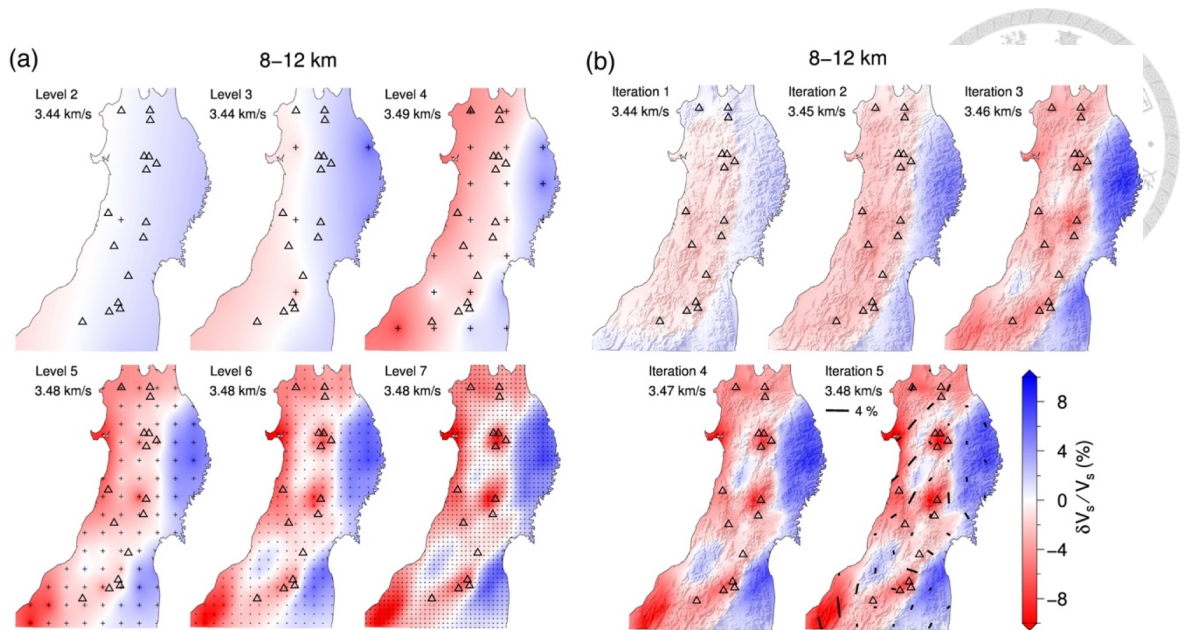
Figure 2.8. (a) Example of how multiscale inversion progressively captures structures on different scales. Each panel shows the model of 8-12 km synthesized from level 2 to higher levels. The highest level and the average velocity of each accumulative model are labeled at the upper left of each panel. Dots represent the nodes of the model at each level. The final model is robust with respect to the locations of lower level nodes. (b) Variations in $\delta Vs/Vs$ in the 8-12 km layer in 5 iterations. In this example, anisotropy is incorporated in the model at iteration 5, and is robust with respect to at which iteration it is incorporated.
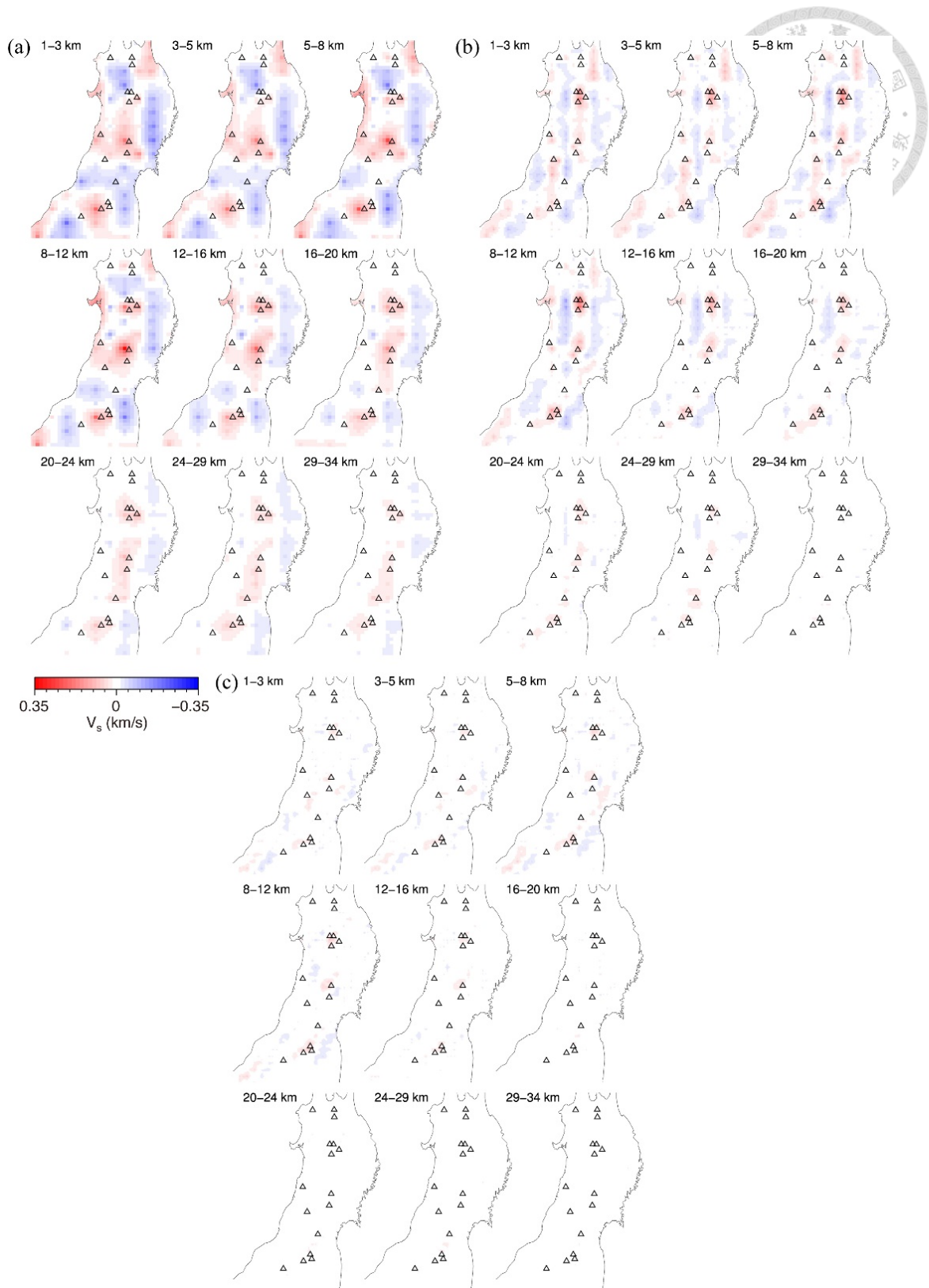
Figure 2.9. Model difference between levels 4, 5, 6, and 7. (a) Model level 5 with model level 4 subtracted (level 5 − level 4). (b) Level 6 − Level 5. (c) Level 7 − level 6. These figures demonstrate where higher level contributions are localized. These figures

22

should be deciphered together with Figure 2.8 and Figure 2.10. Because level 7 has very minor contributions, the model stops at this level.
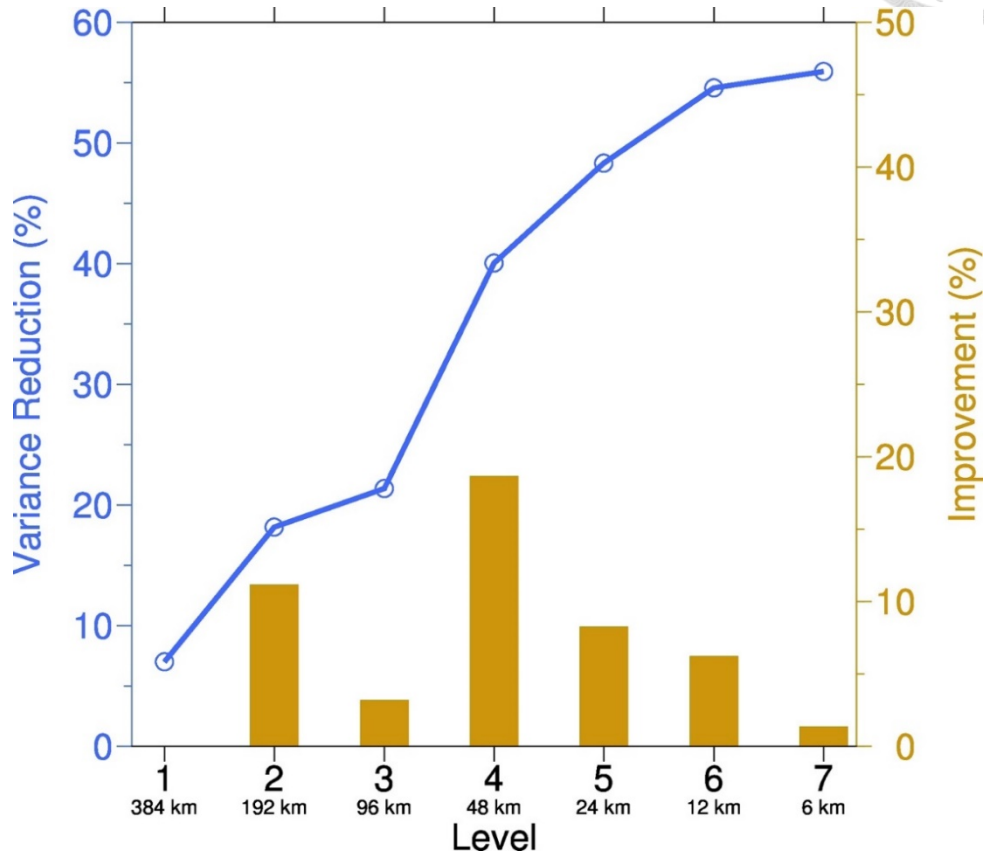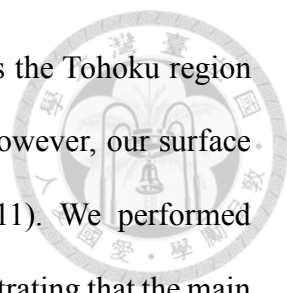
Figure 2.10. Macroscopic view of how multiscale inversion works. This diagram shows the variance reduction increase with increasing levels (circles and blue lines). The variance reduction reaches 56 % for the final model at level 7. Also shown is the variance reduction improvement by adding each level (orange vertical bars). The characteristic length of each level is labelled beneath the level number on the horizontal axis. Adding level 4 makes the largest contribution by reducing variation by 21% relative to level 3. The convergence towards a variance reduction of 56% at level 7 indicates that level 8 is unnecessary.

The depth to the Moho discontinuity varies around 30 km across the Tohoku region (e.g., Zhao et al., 1992; Nakajima et al., 2002; Katsumata, 2010). However, our surface wave model is insensitive to the Moho discontinuity (Figure 2.11). We performed representative recovery test and checkerboard resolution test, demonstrating that the main features in the upper crust is robust (Text 2.6.2, Figures A.1 and A.2, Text 2.6.3, Figure A.3). The Vs perturbations reach beyond $\pm 8\%$ in shallow crust, decreasing to $\pm 3\%$ in the lower crust, with some prominent features being coherent over depth. High Vs anomalies are associated with the Kitakami and the Abukuma Mountains in eastern Tohoku, which are composed of continental magmatic arc of Cretaceous ages (Ozawa et al., 1988; Finn, 1994). In the uppermost crust, these mountains are encircled by 2 to 3% Vs anomaly contours. The continuation of the positive anomalies into the lower layers of the model, although the outline blurs, indicates that these mountain ranges are not shallow structures and may extend to at least the lower crust. The high Vs -mountain correlation in shallow crust is also well defined in Nishida et al. (2008) using Hi-net tiltmeter data, but this correlation appears ambiguous in the nation-wide, F-net based ambient noise tomography model by Guo et al. (2013). While the two models using Hi-net, i.e., Nishida et al. (2008) and this study, share similar features in shallow crust, they diverge with depth, probably due to the differences in the type of data (tiltmeter Vs. velocity) and inversion methods, and, probably to a minor extent, the inclusion of azimuthal anisotropy in this study.

24
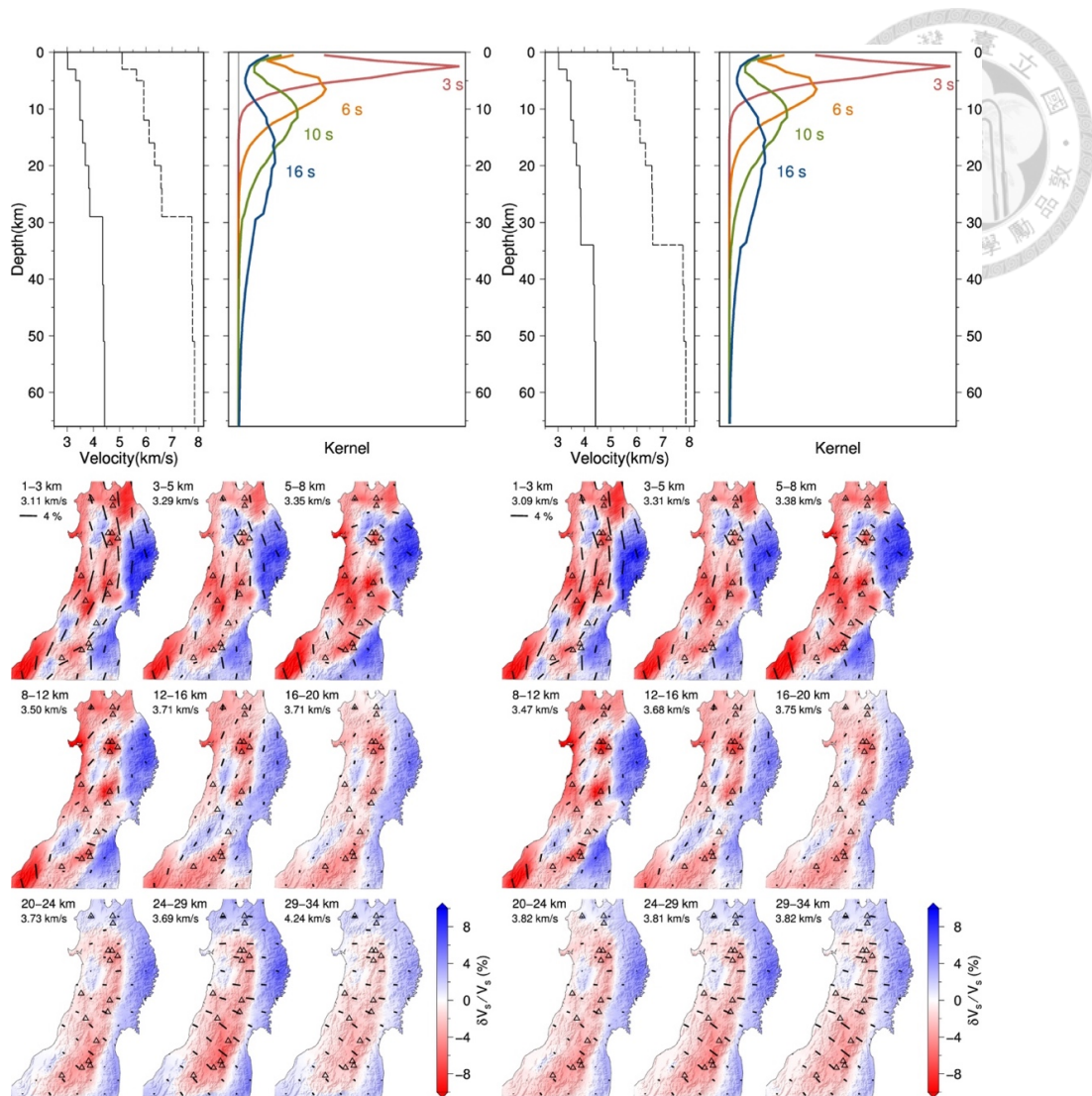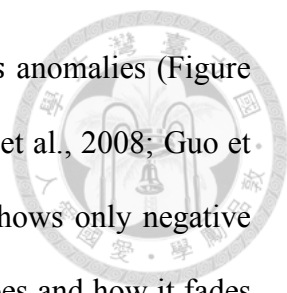
Figure 2.11. A test for the sensitivity of the model to the Moho discontinuity. Upper row: 1D velocity structures and the kernels. Lower row: Final models. Left column: Moho depth at 29 km. Right column: Moho depth at 34 km. The differences between these two models with our model without a particular velocity discontinuity at depth are negligible. The maximum root-mean-square difference in Vs is 0.2 km/s at 30 km depth. The differences in fast direction is less than 12°. The strengths of anisotropy differ by 0.5%. Because the Moho depth may be variable and the depth cannot be updated through iterations due to the insensitivity of the surface wave to this parameter, we chose to use a model with no particular velocity jump representing the presence of Moho.

25

Central and western Tohoku are characterized mostly by low Vs anomalies (Figure 2.6). This is a common feature in all previous studies (e.g., Nishida et al., 2008; Guo et al., 2013), whereas our model provides more details. Figure 2.12 shows only negative perturbations to illustrate the spatial tie between low Vs and volcanoes and how it fades away with depth. A statistical test is devoted to this subject below. We display Vs and anisotropy models in three vertical cross sections: two cutting along the short dimension of Tohoku and one along the long axis of the island. The azimuths of these cross sections are very similar to the trajectory of the maximum compression axes and its normal as shown in Kaneshima et al. (1987) which is based on Ando (1979). It is striking from these cross sections that each volcanic group is underlain by a low Vs anomaly body distributed over $5-15$ km, peaking at either the 5-8 km or the 8-12 km layer. Because the volcanoes are categorized as polygenic (Umeda et al., 2013), these bodies may represent the magma reservoirs which feed the volcanoes continuously over times. For the groups with multiple volcanoes the $\delta V_s/V_s$ reach -6 % or lower, compared with the isolated volcanoes with weak anomalies, such as the Zao volcano (Figure 2.12).

26
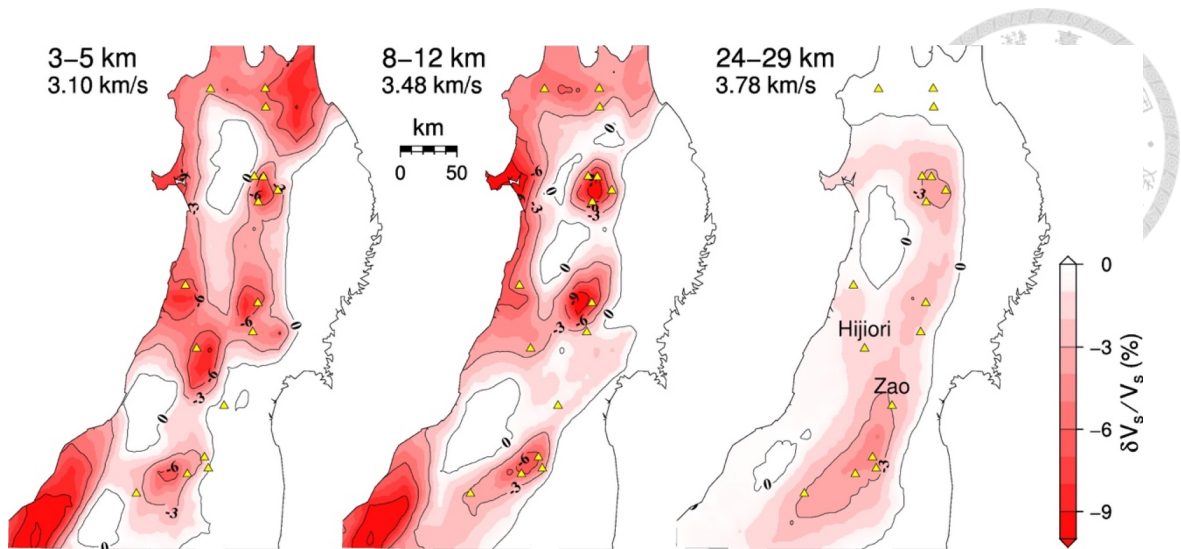
Figure 2.12. The same as Figure 2.6 but only with negative $\delta V_s/V_s$ for three example model layers. Volcanoes are in small yellow triangles. The correlation between volcanoes and low V_s extends to the bottom of the model. The northern Tohoku is poorly sampled with long-period waves in cross-island directions and the V_s there is not well constrained at depths. See Figure 2.3 for inter-station paths.

The azimuthal anisotropy displays systematic variation in 3D model (Figure 2.6). In shallow crust (1-5 km), the resolved fast directions ϕ are mostly parallel to the strike of the island, smoothly rotating from between NS and NE-SW to NNW-SSE from southern to northern Tohoku. The rotation angle seems to exceed that expected from the trajectory of maximum compression axes (Kaneshima et al., 1987) or the maximum compressional axes for both stress and strain rates (e.g., Iinuma et al., 2005). The consistent pattern in shallow crust, however, turns to a random regime in 5-8 and 8-12 km layers. Below this "chaotic" regime the anisotropy resumes its consistency with island-parallel ϕ and a highly subdued magnitude, but its existence is brief and only manifests in one model layer, i.e., 12-16 km. From 20 km downward, the anisotropy grows in strength and rotates to convergence-parallel down to the lower layers of the model. The strength of anisotropy

27

in the lower crust is only half to one third of that in the upper crust.

To help visualize the systematics of the anisotropy, a line along C-C' is considered as a reference line (Figure 2.13). The reference azimuth for each observation in the model is taken from the reference line at the location perpendicularly projected from the observation point. We removed from the observed ϕ the reference azimuth to obtain the corrected fast direction, or ϕ'. Cross sections in Figure 2.13 exhibit four zones of ϕ' with increasing depth: approximately 0° (1 – 5 km), "chaotic" (5 – 12 km), and 0° (12 – 16 km) (Figure 2.6) in the upper to middle crust, and approximately 90° in the lower crust. The deviation from this general pattern with depth is more pronounced in the lower crust in southern Tohoku, where ϕ' are trending at 110 - 120° (or -70 – -60°), rather than 90 (or -90°) from the reference line. Note that the anisotropy "chaotic" regime occurs in the depth range where strongly negative Vs anomalies, or the proposed magma reservoirs, reside. It suggests that the presence of the magma reservoir or the related magmatic activities largely disturb the consistent pattern of anisotropy.

28
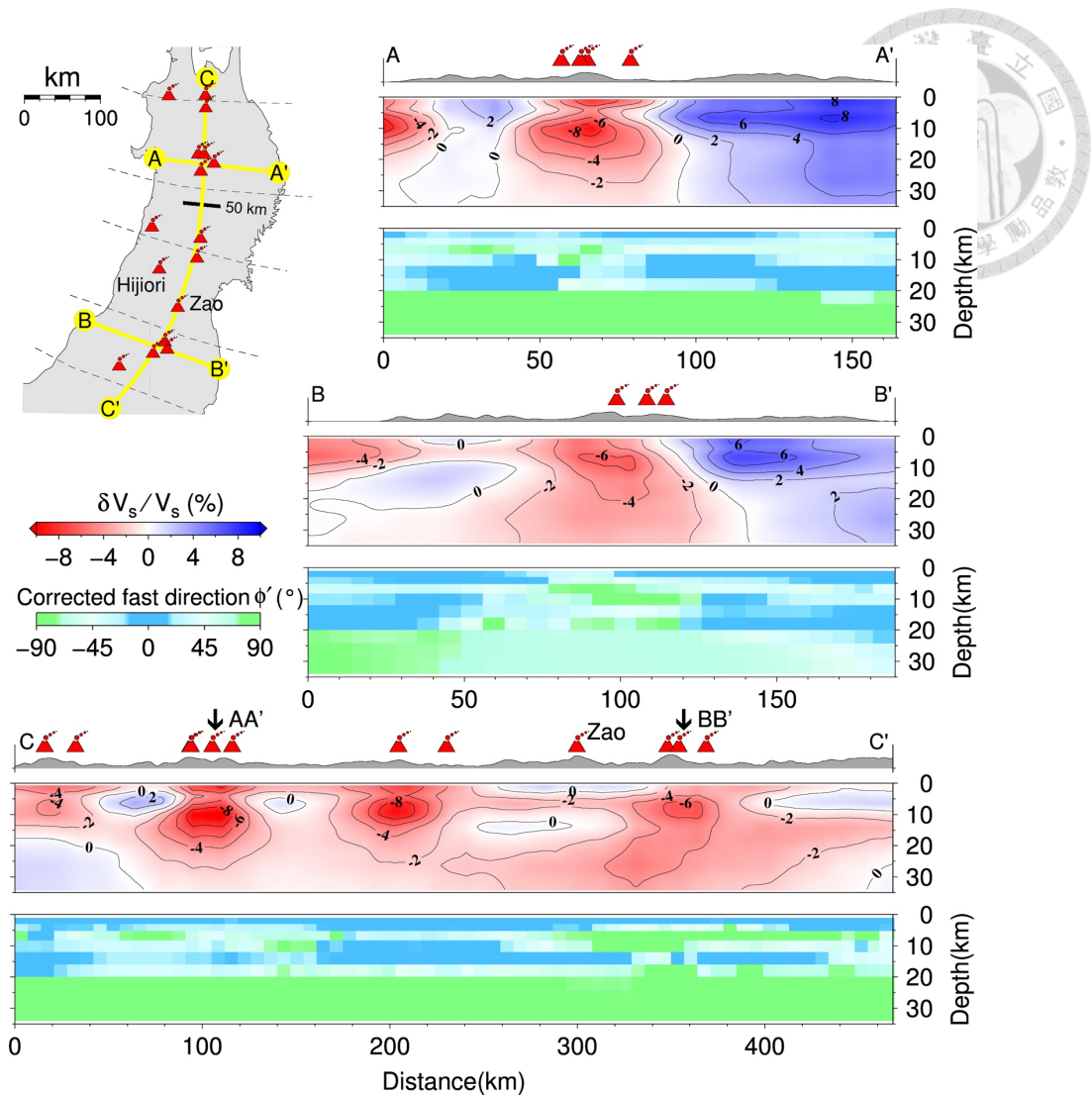
Figure 2.13. Cross-section illustration of Vs and anisotropy models. The upper left panel shows the locations of the cross sections (yellow lines) and the trajectory of maximum compression axes (dashed lines) (Kaneshima et al., 1987). In each cross section, two panels are Vs and corrected fast direction (ϕ'), with respective color scales on the central left. Cross sections AA' and BB' retain true horizontal/vertical ratio, but in cross section CC' the ratio is reduced to 0.7 for illustration purposes. The concentration of low Vs bodies beneath volcanoes is interpreted to represent magma reservoirs. ϕ' switch from nearly 0 (light blue) to random (mixed) to 0 (light blue) in the upper 16 km, and rotate to roughly 90 (light green) in the lower curst. The "chaotic" anisotropy correlates with the pervasive low Vs beneath volcanoes.

29

2.4 Discussion

2.4.1 Vs-Volcano Relationship

Whereas the Vs -volcano correlation in the upper crust is clearly visible from Figure 2.13, to what depth and strength of anomaly this correlation still holds confidently is worth to be quantified. To examine these phenomena, we undertake a binomial test by assuming that a volcano is a "success" if it is associated with low Vs anomalies (e.g., Ray and Anderson, 1994; Kuo and Wu, 1997). The null hypothesis in test is that volcanoes occur randomly in space, or equivalently that the probability of success is determined by the proportion of the area covered by negative anomalies in the whole area. We start with 50% success probability with $\delta V_s/V_s < -0.2$, which occupies half of the total area. We then decrease the success probability by increasing the threshold of low Vs, or $|\delta V_s/V_s|$. As $|\delta V_s/V_s|$ increases, the chance that volcanoes land on the dwindling area of low Vs decreases (Figure 2.12). If the null hypothesis is true, the observed number of success should deviate little from that defined by the ratio of area. We used t-test to examine whether the deviation is significant to reject the null hypothesis in favor of the alternative hypothesis that volcanoes and low Vs are related (Figure 2.6). This exercise is to find the limit of the Vs anomaly to which the Vs -volcano relationship holds as a function of depth (Text 2.6.4, Figure A.4).

Figure 2.14 shows that the limits of $|\delta V_s/V_s|$ for a correlation between Vs and volcano peak in the 1-3 km layer and the 8-12 km layer at -5.6% and almost -8%, respectively. The limits drop for layers in between due to the reduction of the maximum $|\delta V_s/V_s|$ itself. The limits decrease monotonically towards lower crust and hit the minimum of nearly -1% at the 29-34 km layer. The maximum limit in the 8-12 km layer is caused by the concentration of very low-Vs bodies at that depth (Figure 2.13). The tie

between the two phenomena in space as well as in strength in this depth range suggests strong genetic relationship between them. The binomial analysis also suggests that the Vs-volcano relationship extends even to the lower crust, implying that we may have resolved the widespread, low degree partial melting zones beneath the shallow magma reservoirs.
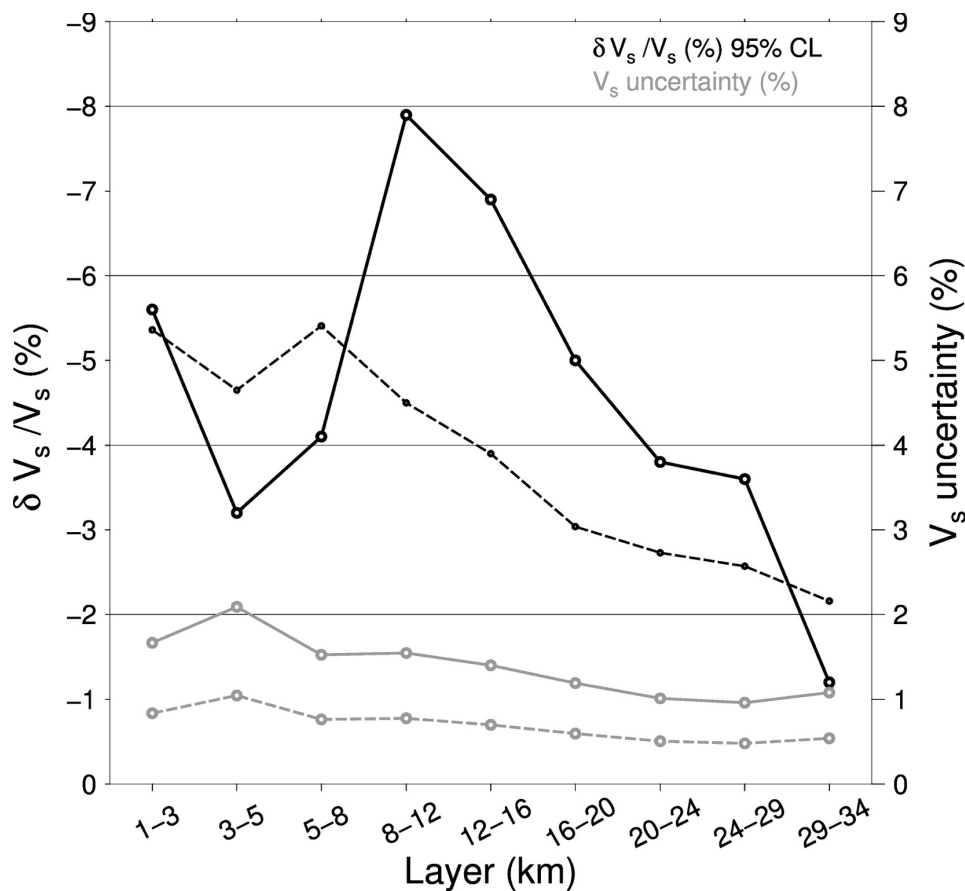
Figure 2.14. Results of the binomial test for the correlation between volcanoes and low Vs. Circles connected by thick lines are the lowest $\delta Vs/Vs$ of the model for the correlation between the volcanoes and negative $\delta Vs/Vs$ to hold true at the 95% confidence level. The relationship between the two variables is most significant at layer 8-12 km, which we interpret as the magma reservoirs being present in that layer. Small dots connected by dashed line is the velocity perturbations corresponding to p=0.1, and

31

the calculated limits are associated with p=0.084, 0.188, 0.178, 0.014, 0.005, 0.008, 0.018, 0.040, and 0.229, respectively, for layers from top to bottom. The errors (dotted grey line) of Vs in each layer were determined from 50 times of bootstrapping experiments (Text 2.6.5, Figure A.5), and the double of the errors (solid grey line) represent the 95% confidence interval of the resolved Vs. The limits of $\delta Vs/Vs$ are mostly way above the uncertainty of the model at each layer.

2.4.2   Anisotropy and Magma Reservoir

The nature of anisotropy also holds key information regarding the Vs-volcano issue. We define the average strength of anisotropy A, average fast direction $\bar{\phi}$, and the circular variance, or the randomness of anisotropy γ according to circular statistics (e.g., Mardia and Jupp, 2000; Audoine et al., 2004):

$$A = \sqrt{\left[\sum_{i=1,N} \sin(2\phi_i) \cdot a_i\right]^2 + \left[\sum_{i=1,N} \cos(2\phi_i) \cdot a_i\right]^2} / N \qquad (2.1)$$

$$\bar{\phi} = \frac{1}{2} tan^{-1}\left[\sum_{i=1,N} \sin(2\phi_i) / \sum_{i=1,N} \cos(2\phi_i)\right] \qquad (2.2)$$

$$\gamma = 1 - \sqrt{\left[\sum_{i=1,N} \sin(2\phi_i)\right]^2 + \left[\sum_{i=1,N} \cos(2\phi_i)\right]^2} / N \qquad (2.3)$$

where subscript i denotes the model parameters at node i, a_i is the strength of anisotropy, ϕ_i is the fast direction, and N is the number of nodes of interest in each layer. According to equation (1), A takes into account both direction and magnitude. γ is the circular variance with zero representing perfectly consistent and unity totally random, and thus is a good indicator of the randomness of ϕ.

To focus on the negative Vs anomalies in the calculations of (1)-(3), we only consider the anisotropy parameters of each layer at those model nodes whose $\delta Vs/Vs$ are within the top x percentage ranked from the most negative anomalies. This approach takes into

32

account the difference in the strength of Vs between layers and guarantees the same number of data for different layers, which facilitate a better statistical comparison. x = 20 and 50 were tested. The three anisotropy parameters defined in (1)-(3), along with the average of the top-ranked negative $\delta V_s/V_s$, are plotted as a function of depth in Figure 2.15.
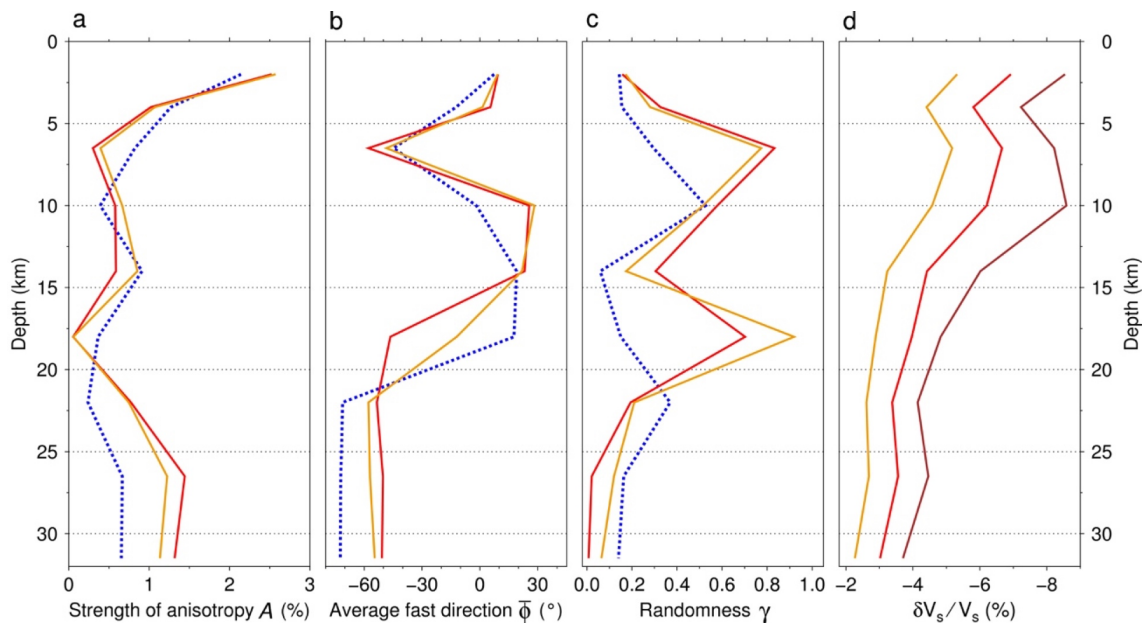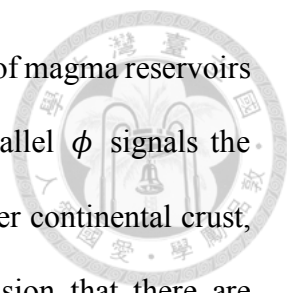
Figure 2.15. Summary of crustal parameters as a function of depth. Red line for top 20% and orange line for top 50% negative perturbations, and blue dotted line for all positive perturbations. (a): Strength of anisotropy, A; (b) Average fast direction, $\bar{\phi}$; (c) Randomness of anisotropy, γ; and (d) Magnitude of the negative Vs anomalies. Note that the correlation between the decreased A, the increased γ, and the increased magnitude of negative Vs anomalies in the upper crust suggests the presence of magma reservoirs between 5-15 km. Brown curve in (d) is for top 5% negative perturbations that implies that the strongest negative anomalies (top 5%) are concentrated in the model layer 8-12 km, where magma reservoirs may be centered. The mild anomalies are more spreading out (top 20 or 50%) above the model layer above it. Across the 15-20 km interval, high-

33

angle rotation of $\bar{\phi}$ is accompanied with a decreased A and an increased γ, marking the switch between two different mechanisms. See text for detailed explanations and implications.
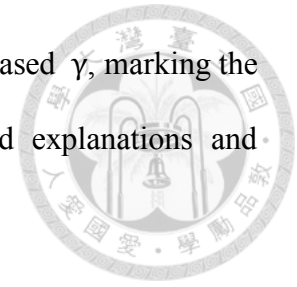
The four parameters in Figure 2.15 have to be deciphered together. A in general decreases with depth in the upper crust and increases mildly in the lower crust. $\bar{\phi}$ seems to vary conspicuously with depth. The first significant change in $\bar{\phi}$ above 16 km depth is not a rotation but rather a rapid switch from island-parallel ($\sim 0^{\circ}$) to a random state of anisotropy and back to island-parallel (Figure 2.6), with γ switching from 0.2-0.4 to 0.8 and back to low values. One can view this rapid change as a brief destruction of the alignment of ϕ in the 5-10 km depth interval, where a_i in equation (1) does not vanish (Figure 2.6) but A hits low because the vectors cancel out when they are randomly orientated. Anisotropy then experiences a significant rotation across the depth interval of 16-20 km (based on model layering) from island-parallel above to convergence-parallel below. During this rotation, γ approaches 1 and A is at the minimum of all. The strength of negative $\delta V_s/V_s$ decreases with depth, with a reverse in shallow crust caused by the concentration of strongly negative V_s anomalies beneath active volcanoes interpreted to represent magma reservoirs (Figure 2.13).
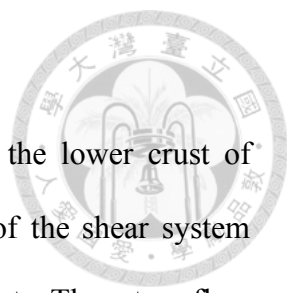
Based on Figure 2.15, we speculate that the deformation of the crust is shaped by contraction, magmatic activities, and shearing due to subduction and/or extension. In the upper crust, the island-parallel anisotropy reflects the presence of NS-oriented, near-vertical foliations or cleavages developed perpendicularly to the axes of maximum principle stress and strain rates (Kaneshima et al., 1987; Iinuma et al., 2005). As suggested by the correlation between A, $\bar{\phi}$, γ, and V_s anomalies (Figure 2.15), the systematic

34

foliation structures in the upper crust were decimated by the presence of magma reservoirs distributed in 5-15 km depths. In the lower crust, convergence-parallel ϕ signals the presence of shear strain that induces the LPO of minerals of the lower continental crust, such as amphiboles (Tatham et al., 2008). Overall, one can envision that there are essentially two layers of anisotropy caused by two dominant mechanisms with the upper layer partially disrupted by magmatic activities.
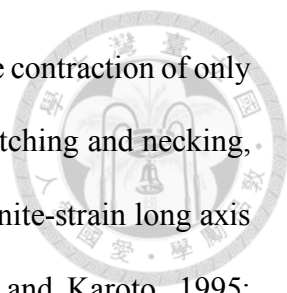
The two-layer deformation with nearly orthogonal anisotropy orientations has been documented for the Taiwan orogenic belt (Huang, Gung, et al., 2015), also constrained by ambient noise tomography. The top layer in Taiwan features orogen-parallel ϕ thought to reflect the rock fabrics developed under the arc-continent collision, and the bottom layer with convergence-parallel ϕ is interpreted to result from shearing induced by subduction of the Eurasian plate. Although the Ryukyu and the Manila subduction zones affect the Taiwan orogenic processes in many ways (Ko et al., 2012; Lin and Kuo, 2016), the magmatism from these subduction zones remains at the peripheral of the Taiwan orogenic belt and thus least intervenes the deformation of the crust (e.g., Wang et al., 2004; Yang et al., 1992). In the Taiwan orogen, γ peaks only at the transition between the two anisotropy domains, unlike in Japan where γ peaks twice. The orogen-parallel paired with convergence-parallel anisotropy at different depths is also observed in Tibet on a much larger vertical scale (Pandey et al., 2015). The mechanisms that caused the layered deformation in these regions may be entirely different, and are a subject beyond the scope of this study.

2.4.3 The Lower-Crustal Flow

We speculate on how the convergence-parallel anisotropy in the lower crust of Tohoku was formed. One scenario is that the lower crust is part of the shear system imposed by the return flow driven by the subduction of the Pacific plate. The return flow in the mantle wedge has long been thought to cause the convergence-parallel anisotropy beneath the back arc region detected using slab earthquakes (Nakajima et al., 2006; Liu and Zhao, 2016). This return flow in the mantle wedge would exert basal traction on the overriding plate to deform it (e.g., Holt et al., 2015). However, in the conceptual models in previous studies the mantle lithosphere of the Okhotsk plate is often omitted and the return flow is implied to directly apply on the bottom of the crust (e.g., Hasegawa and Nakajima, 2004; Huang et al., 2011a). If this is true, the return flow could drive the shear in the lower crust to produce convergence-parallel anisotropy. One possible mechanism to facilitate this scenario is the intrusion of partial melts into the overriding plate to lower the viscosity there, as suggested by low-Vs images in body-wave tomography (e.g., Hasagawa and Nakajima, 2004; Zhao et al., 2015). A series of such anomalous structures along the island, interpreted as "hot fingers" by Tamura et al. (2002), may thermally erode the mantle lithosphere and expand upward the ductile regime beneath the arc and backarc. How to build up finite strain in the lower crust is the key factor to be considered for this hypothetical model.

If the Okhotsk lithosphere survives the mantle flow and remains strong, the lower crust anisotropy needs other mechanisms to maintain. Another scenario considers the extensional strain preserved from the last episode of rifting of the Japan Sea and the island. Okada and Ikeda (2012) concluded that the crust of northeast Japan has experienced extension via a sub-horizontal major detachment and a series of normal faulting in the Miocene time prior to the contraction that shortened the crust since the late Pliocene. The

36

Miocene extension measures 30-60 km in the EW direction, versus the contraction of only 10-15 km. The lower crust may have reacted to the extension by stretching and necking, during which both pure-shear and simple shear with shear plane or finite-strain long axis oriented EW may give rise to the LPO (e.g., Ribe, 1992; Zhang and Karoto, 1995; Kaminski and Ribe, 2002) and ultimately a convergence-parallel fast direction. These fabrics could survive the short contraction (Okada and Ikeda, 2012). The detachment fault in Okada and Ideka's (2012) model is placed at 10 km depth, below which the presence of ductile flow is implied, while the ductile lower crust may begin at 15-20 km in our model.

2.4.4 More About Magma Reservoir

Our interpretation for the concentrated, low Vs bodies in the shallow crust as magma reservoirs for the volcanoes above them is supported by geochemical evidence. Zao and Hijiori volcanoes (See Figures 2.12 and 2.13 for their locations) are estimated by petrological analysis to tap shallow magma reservoirs within 10 km depth (Ban et al., 2008; Miyagi et al., 2007). The low Vs anomaly beneath Zao volcano is the weakest among all, which may be attributed to the short residence time and sluggish supply rate for its magma reservoir (Ban et al., 2008). In contrast, in the recent model by Niu et al. (2018), low Vs and high Poisson's ratio are found in the lower crust beneath the Zao volcano, and the low-frequency earthquakes, also in the lower crust, are located beneath the Zao (Figure 2.16). The difference between our ambient noise tomography and the body-wave tomography can be attributed to many factors, but mainly the former has enhanced sensitivity in the upper crust and degrading resolution with depth, while for the latter sensitivity is nearly constant along the path for short-period and local earthquakes. Both need cross-paths to build up 3D resolving power. Figure 2.16 shows that the magma

reservoirs resolved in this study and the crust above them for some volcano groups are riddled with high density seismicity (e.g., Kurikomayama and Naruko), whereas for others the seismicity is diffuse or offset laterally (also see Figure 2.17 for map view).
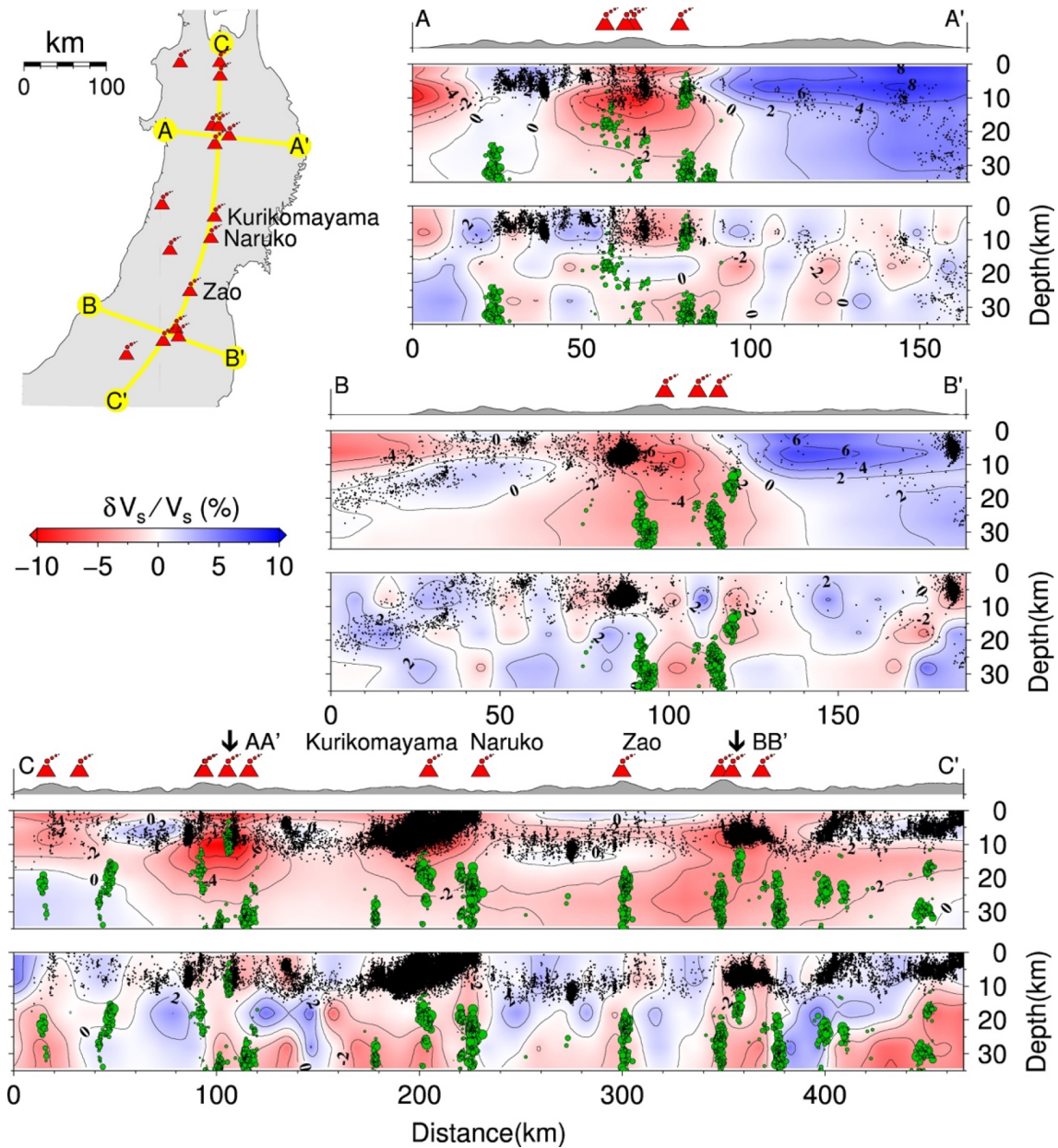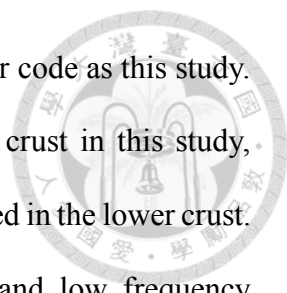
Figure 2.16. Comparison of $\delta Vs/Vs$ between this study and Niu et al. (2018) along the three cross sections used in Figure 2.13. In each cross section, top and bottom panels correspond to this study and Niu et al. (2018), respectively. Green circles denote the low frequency earthquakes and dots denote crustal seismicity, both data provided by Niu et al.

38

(2018). The model of Niu et al. (2018) is plotted using the same color code as this study. Low velocity anomalies are clustered with volcanoes in the upper crust in this study, compared with the low velocities in Niu et al. (2018) that are distributed in the lower crust. Zao volcano is underlain by local low Vs in Niu et al. (2018) and low frequency earthquakes in the lower crust, contrasting to the weak anomalies in the upper crust resolved in this study. High density seismicity is clustered closely with the magma reservoir and the crust above it for the volcano group of Kurikomayama and Naruko (see the upper-left panel for their positions), whereas seismicity widely spreads in the vicinity of other volcanoes.
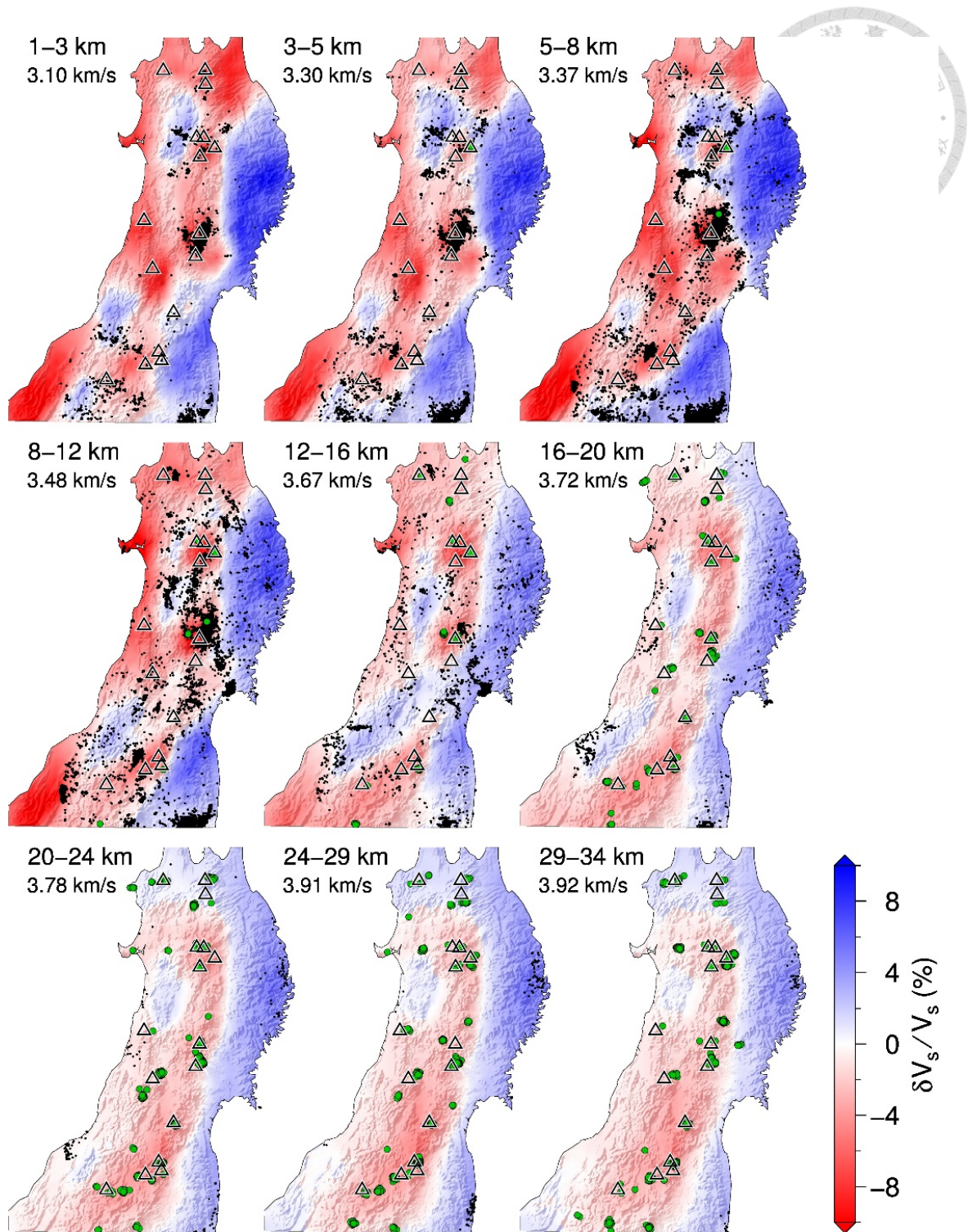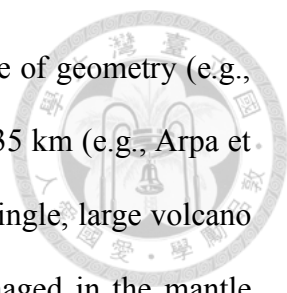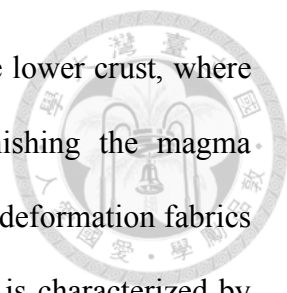
Figure 2.17. Map view of the superposition of crustal seismicity (dots in upper crust), low-frequency earthquakes (green circles in mid-lower crust), both provided by Niu et al. (2018), and the Vs model of this study. Volcanoes are denoted by triangles. The seismicity is clustered with some magma reservoirs but not all.

40

The magma plumbing system of volcanoes presents a wide range of geometry (e.g., Zellmer and Annen, 2008) with variable reservoir depths from 5 to 35 km (e.g., Arpa et al., 2017; Zellmer et al., 2016) or perhaps multiple reservoirs for a single, large volcano (Huang, Lin, et al., 2015). In Tohoku, the anomalously low Vs imaged in the mantle wedge by previous studies often intensify at the uppermost mantle (at ~ 30 km depth), which may signal the increased ponding of melts, and has been suggested to be the deep magma reservoirs that feed the shallow ones and the volcanic arcs (Nakajima et al., 2001). The P+PmP imaging of the crust in northern Tohoku by Xia et al. (2007) yields low Vs anomalies in the vicinity of the volcano cluster in both upper and lower crust, suggesting the possibility of interconnection between shallow and deep magma reservoirs. This image is different from our model in which magma reservoirs are mainly isolated in the upper crust (Figure 2.13). In addition to the inherent difference between surface wave and body wave described above, the PmP phase provides improved constraints on lower crust structures, but is also sensitive to the depth of the Moho prescribed in the model. These discrepancies between models call for a joint inversion in the future.

2.5   Conclusions

Northeast Japan, or the Tohoku region, is a typical subduction-magmatism domain along the Japan islands free from complex plate evolution. Ambient noise tomography with the high density seismic data from Hi-net allows us to map out the isotropic and anisotropic properties of the crust in this region. Our model illuminates the Cretaceous mountains in eastern Tohoku and their roots in the lower crust as relatively high Vs. Western Tohoku is characterized by low Vs, especially along the present-day volcanic arc. The active volcanoes are underlain by concentrated, low Vs bodies at approximately 10 km depth, which may represent magma reservoirs for these volcanoes. A binomial

statistic suggests that the low Vs -volcano relationship extends to the lower crust, where low-degree partial melts may be diffuse spatially before replenishing the magma reservoirs above. We interpret the observed azimuthal anisotropy as deformation fabrics of the crust produced by three factors. The bulk of the upper crust is characterized by island-parallel fast propagation direction probably caused by the geological fabrics developed in both extension and shortening stages. However, in the shallow crust where magma reservoirs are thought to reside, coherent crustal fabrics collapse and anisotropy turns to a chaotic state. The lower crust is dominated by convergence-parallel anisotropy caused by alignment of intrinsic anisotropic minerals by shearing in the ductile regime. We speculate that shearing may be driven by either the return flow in the mantle wedge or the last episode of extension of the Japan Sea that survived the incipient compression tectonics prevalent in the Tohoku region at present.

2.6 Appendix A

2.6.1 Inversion for Vs and anisotropy

Rayleigh wave phase velocity in media with slight elastic anisotropy can be expressed in terms of isotropic, 2θ and 4θ components with θ being the azimuth along the propagation path (Smith and Dahlen, 1973). Because the azimuthal dependence of Rayleigh waves is typically much more sensitive to the 2θ components than the 4θ components (Montagner and Nataf, 1986), for simplicity, only the azimuthal dependence with 2θ variations is considered in this study, and the corresponding SV component of shear wave, Vs, can be approximated by

$$V_s(z,\theta) = V_{s0}(z) + A(z)\cos 2\theta + B(z)\sin 2\theta \qquad (A.1)$$

where θ is the azimuth along the propagation path, z is the depth, V_{s0} is the

isotropic velocity, and A and B are the anisotropic terms. The strength of Vs anisotropy $a_{2\theta}$, and the associated fast polarization direction $\phi_{2\theta}$ at the depth z are given by

$$
\begin{cases}
a_{2\theta}(z) = \sqrt{A(z)^2 + B(z)^2} \\
\phi_{2\theta}(z) = \frac{1}{2}\arctan\left(\frac{B(z)}{A(z)}\right)
\end{cases}
\tag{A.2}
$$

Starting from an isotropic layered model, we invert for the 3-D variations of $V_{s0}(z)$, $A(z)$ and $B(z)$ using the phase velocity dispersion of fundamental mode Rayleigh waves.

The perturbed phase velocity C is related to the sensitivity kernels and the model parameters by

$$
\delta C = \int K_S(z)(\delta V_{s0}(z) + A(z)\cos2\theta + B(z)\sin2\theta)\,dz
\tag{A.3}
$$

Where the sensitivity kernel, $K_S(z)$, is defined by $K_S(z) = \frac{\partial C}{\partial V_s(z)}$, and can be calculated by using DISPER80 (Saito, 1988). Examples of depth kernels at representative periods are shown in Figure 2.5.

Specifically, in the inverse problem $\mathbf{d} = \mathbf{Gm}$, the data array $\mathbf{d}$ is composed of travel time residuals between the observed travel times evaluated from the measured phase velocities and those estimated from the starting reference models, $\mathbf{m}$ is composed of the model perturbations of $V_{s0}(z)$, $A(z)$ and $B(z)$, and $\mathbf{G}$ is the sensitivity matrix. Note that the travel time is linearly related to the propagation distance and the slowness of phase velocity, i.e., $S = 1/C$, and their perturbations are simply related by $\delta S = -\frac{1}{C^2}\delta C$. Thus, we have explicit linear relationship between the data array $\mathbf{d}$ and the model parameters $\mathbf{m}$, by which we may build up the sensitivity matrix $\mathbf{G}$ accordingly.

Prior to the inversion, we perform the wavelet transform by the efficient lifting scheme (Sweldens, 1996). In the wavelet domain, we may recast the inverse problem as

$$
(GW^{-1})(Wm) = d
\tag{A.4}
$$

43

where W represents the matrix that transforms the spatial variations from a locally defined function to wavelet domain. That is, we are now solving for wavelet coefficients for the multi-scale representation of the model. The solution of model estimates, $\widehat{m}$, can then be solved by the damped least squares (DLS) algorithm (e.g., Lawson and Hanson, 1974),

$$\widehat{m} = W^{-1}[(GW^{-1})^T(GW^{-1}) + \theta^2 I]^{-1}(GW^{-1})^T d \qquad (A.5)$$

Where θ^2 is the non-negative damping factor, and I is an identity matrix. The advantages and details of this techniques have been well documented in earlier work (e.g., Chiao et al, 2003; You et al., 2010; Huang et al., 2012).

In this study, we have also accounted for in the depth kernel the effects of Vp perturbations on the phase velocity by assuming a constant ratio Vp/Vs, and our tests have shown that the resulting models remain stable for a wide range of Vp/Vs, choices (1.7 - 2.0). This is expected, because Rayleigh waves are much more sensitive to Vs than to Vp structure.

2.6.2 Recovery test

We conducted a recovery test to evaluate the reliability of the model in resolving both Vs and its anisotropy. One test is to input a complete Vs and anisotropy model and check if the inversion procedure entertained in this study can recover these known structures. Here we take the final model of this study as the input model, calculate the inter-station traveltimes from the kernels exactly for the input model, and blend in random errors with amplitude 2.5% of the traveltimes. We invert this synthetic dispersion data as we did for the real data. In the input model, we inserted anisotropy that has 3 different patterns over depth. The input and output models are shown in Figures A.1 and A.2. The

44

conclusion is that the data set and the modeling technique used in this study allow us to resolve well the 3D structures of the Tohoku region.
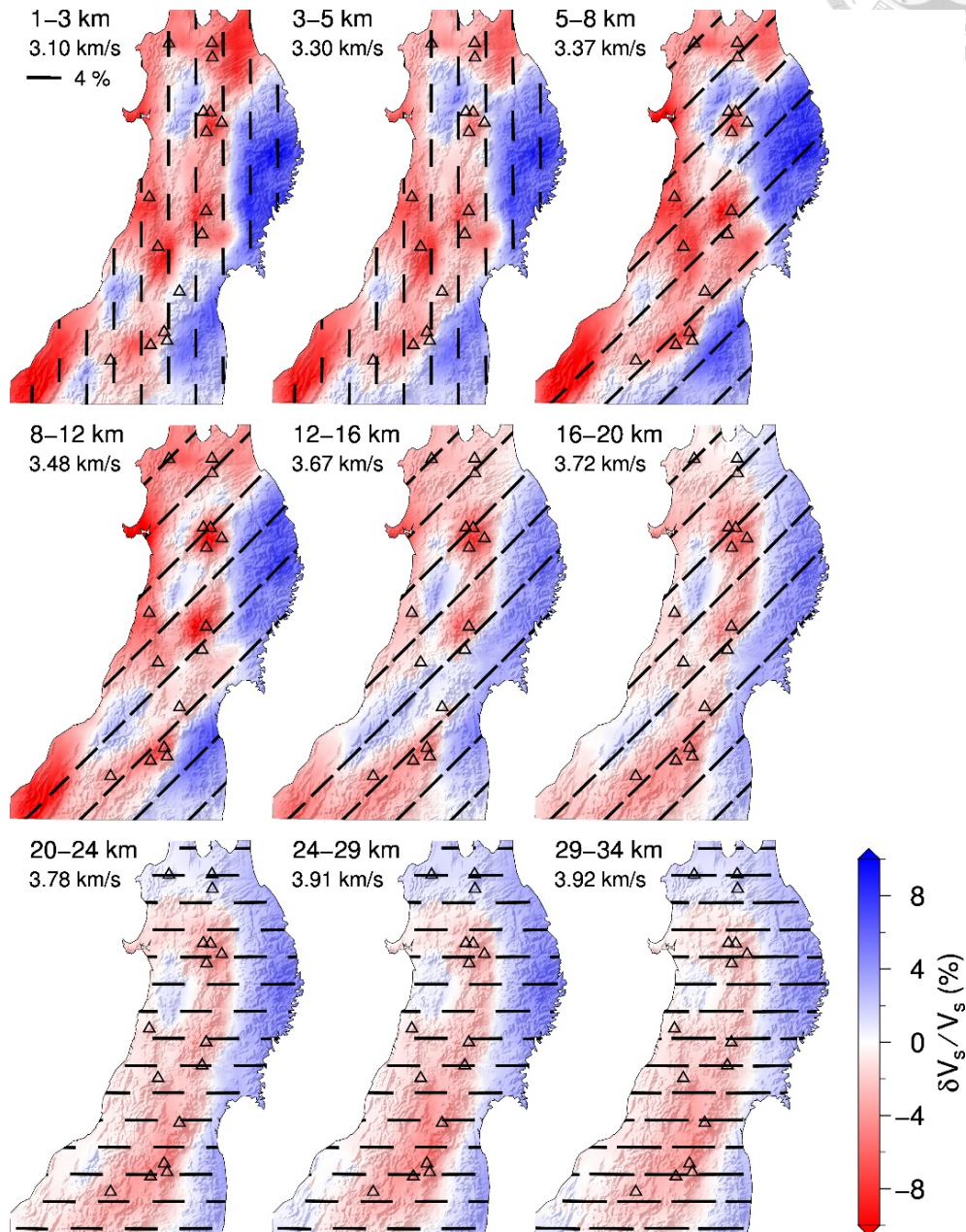
Figure A.1. The input model for the recovery test. Three patterns of anisotropy are assumed at different depth ranges. The synthetic traveltimes as a function of periods are calculated using the kernels corresponding to this model, and 2.5% error is randomly blended into the traveltimes. The inversion follows exactly the routine performed for the real data.

45
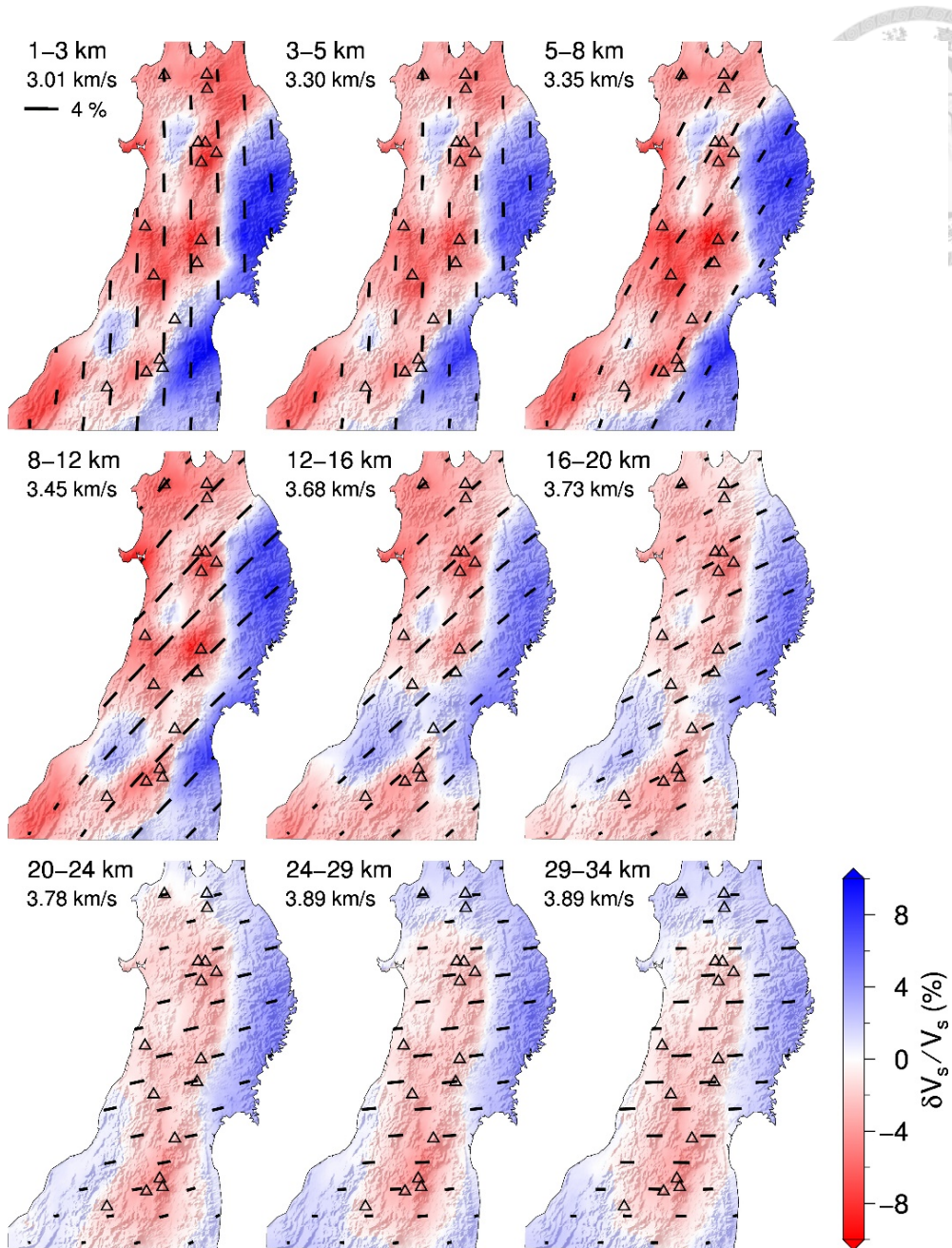
Figure A.2. Output model of the recovery test with the input in Figure A.1. Major patterns of Vs and anisotropy are resumed well. The variance reductions (output relative to input models) for $\delta Vs/Vs$ for layers from top to bottom are 88, 88, 89, 87, 83, 82, 83, 85, 85%, respectively.

2.6.3 Checkerboard resolution test

The checkerboard test addresses the variability of resolution with respect to the scale of velocity variations, utilizing patterns of alternating positive-negative anomaly assigned to a uniform grid model. It is a convenient tool to illustrate the trend of how the model performance degrades in mapping details. We provide two checkerboard tests with alternating pattern of $\pm5\%$, bell-shaped Vs anomalies on horizontal scales of 70 and 35 km, corresponding to the scales at levels 3-4 and 4-5, respectively. These patterns of anomaly were assigned to the 9 layers between 1 and 34 km depth, and shifted horizontally by half of the horizontal scale over every three model layers. Thus, the input model has 3 sets of consistent pattern over the depth ranges of 1-8, 8-20, and 20-34 km. The thicknesses of these 3 layers are 7, 12, and 14 km, respectively, which are all smaller than the horizontal scales tested. As in the recovery test, 2.5% normally distributed random errors are blended in the synthetic traveltimes calculated from the input models. The damping used in these tests are the same as that for the real model. Figure A.3 shows the input and output models for the two checkerboard tests. One can conclude that the model retains a resolution of roughly 70 km to a 30 km depth, and that the resolution of 35 km remains in the upper crust but degrades rapidly in the lower crust. Note that the low-Vs anomaly bodies resolved in the upper crust distributed along the active volcanic arc have dimensions of roughly 50 km and the mountain ranges in eastern Tohoku have larger dimensions (see Figure 2.13). Both features are robust ones in the model.

47
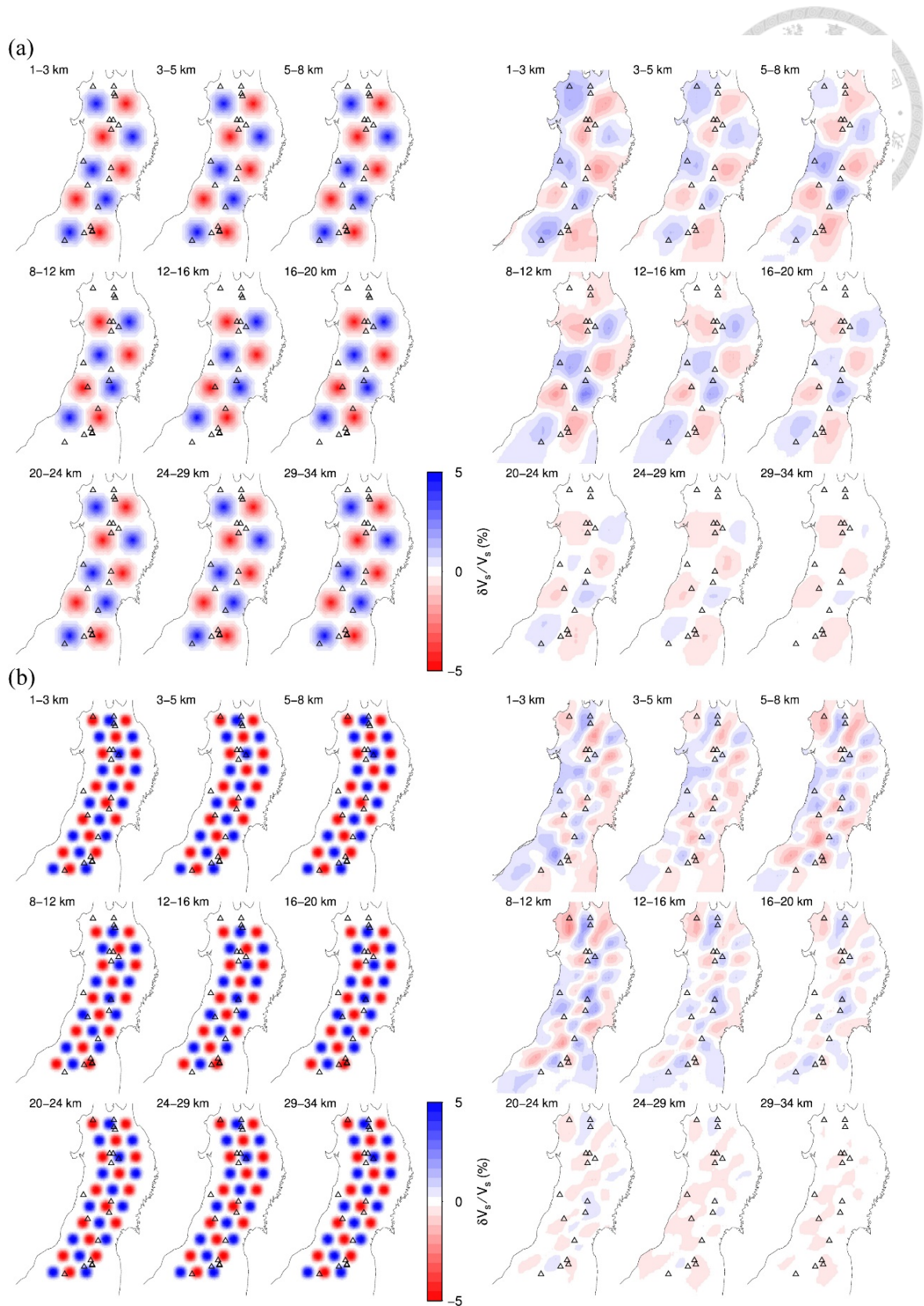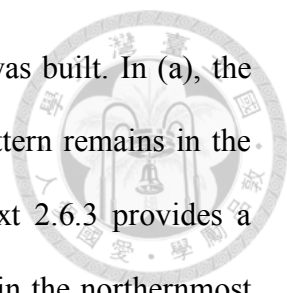
Figure A.3. Checkerboard test for alternating anomalies of scale (a) 70 and (b) 35 km.

70 and 35 km correspond to levels 3-4 and 4-5, respectively, in the multiscale inversion

used in the present work. See text 2.6.3 for how the input model was built. In (a), the pattern can be largely reproduced in the lower crust. In (b), the pattern remains in the upper crust while progressively vanishes below 20 km depth. Text 2.6.3 provides a discussion of the checkerboard test. The lack of EW crossing rays in the northernmost area is reflected in the recovered NNE-SSW trending pattern connecting initially separated anomalies.

One has to be cautious in interpreting the results of the checkerboard resolution test. The test is sensitive to the ratio of the assumed magnitude of the velocity anomaly to the assumed error in the measurement. The test tends to perform better when this ratio is large. The parameters we used, i.e., 5% anomaly and 2.5% data error, are not far from reasonable but still ad hoc. Another issue with the checkerboard is that the tightly spaced patterns of anomaly rarely happen in reality. Lastly, the checkerboard scales, like 70 or 35 km tested above, are not to be confused with the local resolution, as horizontal resolution is always heterogeneous. In this study, the multiscale inversion employs to higher level wavelet coefficients, i.e., to levels 6 and 7 with grid spacing of 12 and 6 km, respectively, which allow to "patch" the region where data constraint is better than elsewhere. These are the points to note about the checkerboard test.

2.6.4   The binomial distribution and t-test

The binomial distribution has a probability mass function as follow

$$BDP(x) = \frac{n!}{x! \times (n-x)!} \times p^x \times q^{(n-x)} \qquad \text{(A.6)}$$

which states the probability of getting x successes in n trials. In this formula p is the probability of an event turning out to be a success and q is the probability of failure, or 1-

p. The binomial distribution has a mean of *np* and a variance of *npq*. In this study, volcano landing in negative δVs/Vs region is a success, and therefore if volcanic activity occurs randomly in space, *p* reflects the ratio of the area of negative δVs to the total area. For the threshold δVs/Vs = -0.2%, *p* = 0.5 (not exactly zero perturbation as it depends on the strengths of the negative Vs. the positive anomalies). *p* decreases with increasing threshold of the negative perturbation |δVs/Vs|. It is a matter of whether the observed number of "successes" *x* is significantly different from that expected from the null hypothesis, i.e., *np*.

To estimate the confidence interval of the expected number of successes corresponding to the given *p*, i.e., *np*, under the null hypothesis we follow the Wald-approximation in which the BDP is approximated by a normal distribution. This is usually not suggested for samples of small size or *p* being close to 0 or 1, which likely encounters high skewness or coverage problem. However, we see no point to explore more sophisticated methods because *p* in this study is always equal to or less than 0.5 and the observed numbers of successes are always on the larger side of *np*, where the confidence interval approximates that calculated from other approximations better than the Wald. At the same time, we show results with a minimum *p* of 0.1, as a comparison. This minimum value prevents us from testing the cases with strongly negative perturbations (therefore too small a *p*), which are sensitive to the regularization of the inversion. We employ the *t*-test with degrees of freedom *n*-1, with the *t*-value constructed as

$$t = \frac{x - np}{\sigma} \tag{A.7}$$

where x is the observed number of successes and σ is the standard deviation of the binomial distribution, i.e., $\sigma = \sqrt{npq}$. The critical *t*-value at 95% confidence level for degrees of freedom 15 is 2.131. If the calculated *t* value exceeds the critical *t*-value, we

50

reject the null hypothesis at the corresponding confidence level. The maximum $|\delta V_s/V_s|$ for the rejection of null hypothesis for each model layer is plotted in Figure 2.14. Similar binomial test has been applied to the correlation between the presence of the plumes at the core-mantle boundary and the low Vs in the D'' zone (Kuo and Wu, 1997). Figure A.4 illustrates a few cases in which the null hypothesis is either rejected or not rejected in this study.
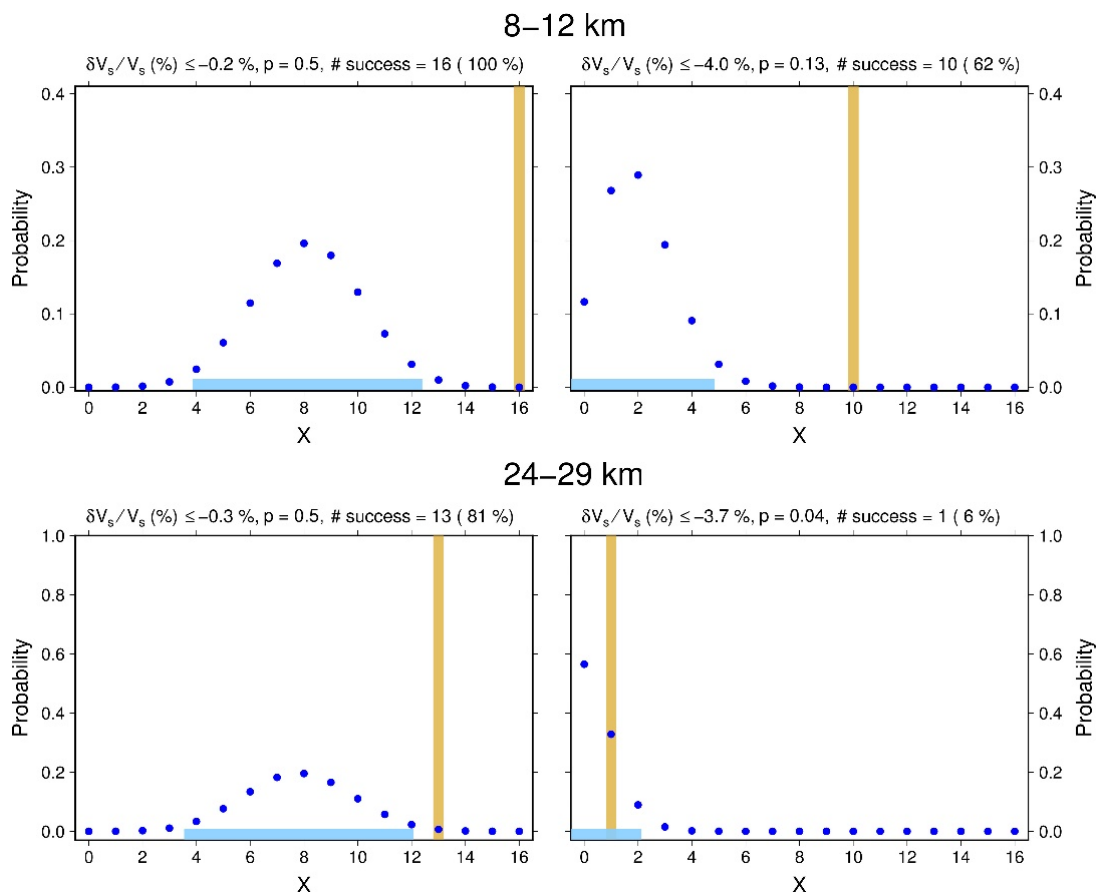
Figure A.4. Example of the t-test for the binomial distribution of the volcanoes in relationship with low Vs. In each panel, horizontal axis is the number of volcanoes x, and the vertical axis is the calculated binomial distribution probability (dots) for the 16 "trials." Horizontal bar in light blue represents the 95% confidence interval of the expected mean of *np*. Vertical bar in yellow is the observed number of "success," i.e., number of volcanoes falling into the low Vs with the given *p*. On top of each panel listed the limit

of δVs/Vs, its corresponding p, and the number of success. Top row: 8-12 km layer. bottom row: 24-29 km layer. Only the case in the lower right panel indicates a failure, i.e., the number of successes does not exceed the expected value by a comfortable margin for error.
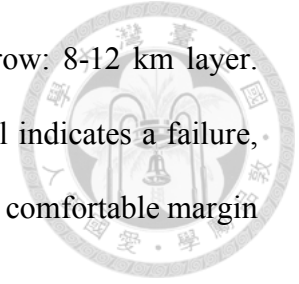
2.6.5 Bootstraps experiments

We apply bootstrap test to estimate the Vs and Vs anisotropy uncertainties. In total, 50 experiments were conducted by randomly selecting 70 % of total data at each period for the inversion. The results of anisotropy from these 50 experiments are shown in Figure A.5.
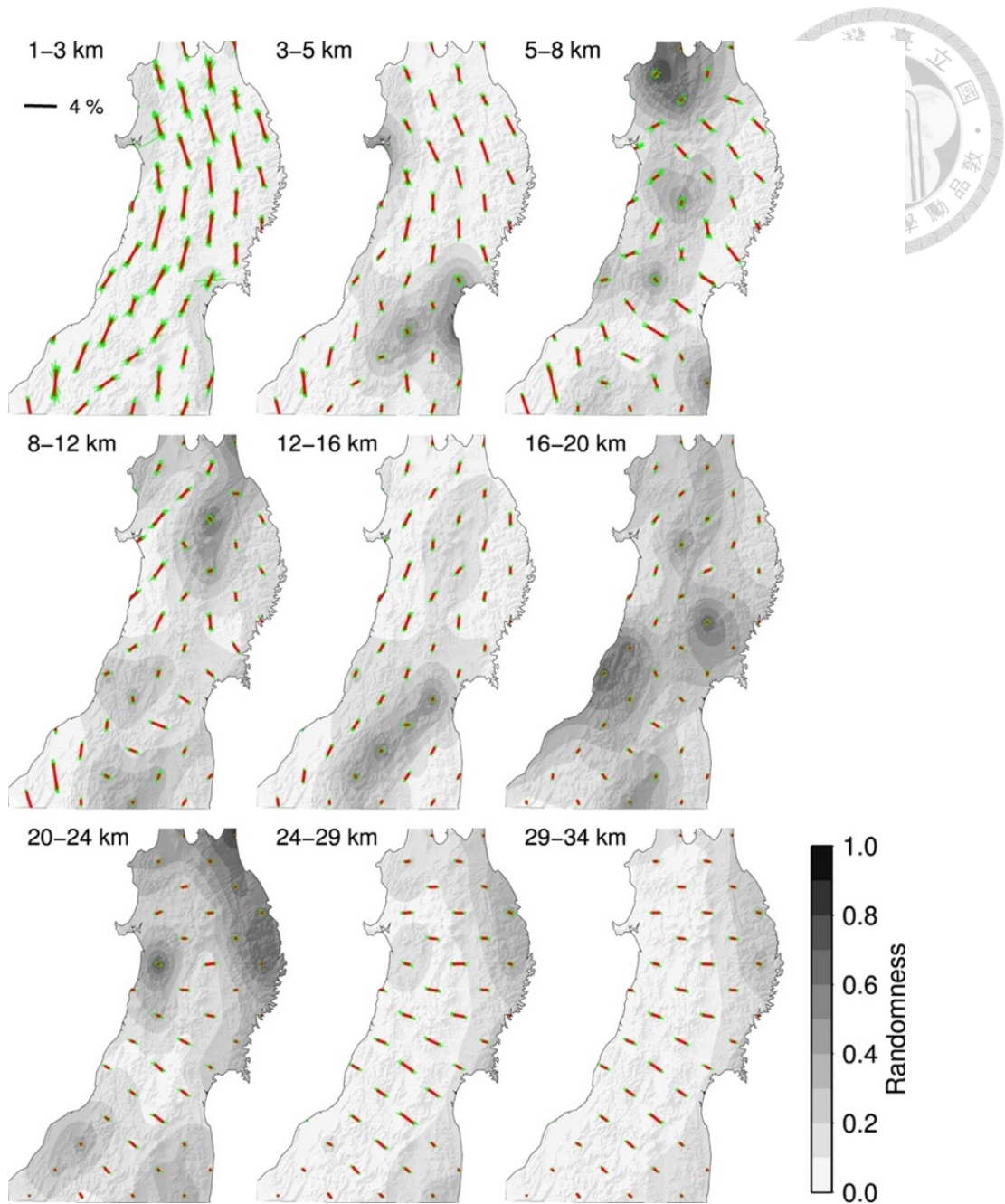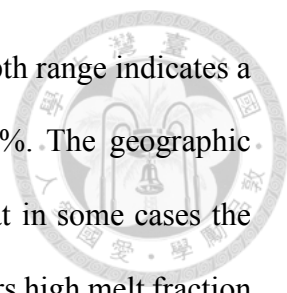
Figure A.5. Results of bootstrap test consisting of 50 inversions each with a subset of data randomly picked from 70% of the original data. Green bars represent anisotropy fast directions and strengths from these 50 experiments and red bar is the average, at selected nodes. Circular variance, or the randomness, is shown in the background. Randomness is high when the strength of anisotropy is low (short bar). In general, the large scale patterns discussed in text 2.2 are robustly recovered.

Chapter 3   Imaging crustal melt beneath northeast Japan with Ps receiver functions

To investigate crustal structures related to melt storage, Ps converted waves were used to image crustal velocity discontinuities across the Tohoku region of northeast Japan. Ps receiver functions from 127 permanent seismic stations were migrated to depth, accounting for variations in crustal velocity structure. In the 5-15 km depth range, negative Ps phases indicative of velocity decreases with depth are prevalent in central and western Tohoku, where Holocene volcanoes occur and surface wave tomography indicates low crustal velocities. Large negative Ps phases are largely absent in the crust of the old mountain terranes in eastern Tohoku where crustal velocities are higher. In central and western Tohoku, velocity gradients inferred from Ps phases and shear velocity anomalies are consistent with models for crustal melt storage that involve trans-crustal zones of crystal-melt mush where the highest concentrations of melt are localized at the top of the mush column. Negative Ps phases are concentrated at depths of 5-10 km, and many correlate with the upper margins of localized low velocity zones beneath volcanoes. These correlated features are consistent with the roofs of high melt fraction layers. At depths of 10-30 km, positive Ps phases are consistent with gradual velocity positive gradients that correspond to decreasing melt fraction with depth in the mush column, although some groups of deeper negative Ps phases at depths of 10-20 km may reflect local maxima in melt fraction. The amplitudes of the negative Ps phases at 5-10 km depth vary significantly. In a higher amplitude example, waveform modeling of Ps receiver functions from a station near Hijori volcano indicates a $16\% \pm 5\%$ Vs drop at 10 km depth, implying melt fractions of $10\% \pm 3\%$ if Gassmann's equations are assumed, above a velocity increase from 10 to 20 km that indicates decreasing melt fractions with depth.

55

However, modeling of lower amplitude Ps phases in the 5-10 km depth range indicates a 7% ± 3% velocity drop and a maximum melt fraction of 5% ± 2%. The geographic distribution of apparent melt fraction at 5-10 km depth suggests that in some cases the same upper crustal source can supply multiple volcanoes, and in others high melt fraction zones are significantly laterally offset from the nearest volcano. This abstract and the following subchapters are from Chen et al. (2020).

3.1　Introduction

3.1.1　Crustal magma storage

The structure and behavior of crustal magmatic systems, particularly in the upper crust, are key to understanding the last stages of magma evolution and transport before volcanic eruption. Views of crustal melt storage have evolved towards models involving "mush" zones in which crystals form an interconnected lattice with the remaining volume filled by melt and volatiles (e.g. Bachmann and Bergantz, 2004; Hildreth, 2004; Huber et al., 2009). In these models, most crustal melt is stored in the middle and lower crust, with basaltic melts prevalent in the deep crust and progressively more silicic compositions at shallower depths (e.g. Bachman and Huber, 2016; Cashman et al., 2017; Jackson et al., 2018; Sparks et al., 2019). Melt fractions that are high enough to be eruptible (>~50%, Bachman and Huber, 2016; >~40%, Cashman et al., 2017) accumulate only near the top of these systems and are thought to be ephemeral and/or too small to image by geophysical methods. While trans-crustal mush models assume that melt is distributed throughout the crust, some models imply that larger-scale melt-rich lenses exist at all depths (Cashman et al., 2017; Sparks et al., 2019) versus two or three typical depths where melt fractionation is concentrated (Bachman and Huber, 2016). Recent thermo-

mechanical modeling indicates magma chambers that are able to grow and persist while also being tapped by eruptions will exist only in a narrow pressure range of 1.5 to 2.5 kbar (Huber et al., 2019). This model predicts that particularly low seismic velocities should be concentrated in the 5-10 km depth range.

While melt fractions inferred from tomographic imaging tend to be significantly lower than the eruptible limit (e.g. Huang et al., 2015; Kiser et al., 2018), consistent with the idea that zones with high melt fractions are ephemeral or small, some converted body waves studies have found evidence for larger reductions in seismic velocity associated with potential magma storage (Nakamichi et al., 2002; Bannister et al., 2004; Chu et al., 2010; Janiszewski et al., 2013; Ward et al., 2014). In this study we use Ps converted waves to study crustal structure and its implications for transcrustal mush models and the distribution of crustal melt beneath the Tohoku region of Japan.

3.1.2 Subduction, the Tohoku arc and crustal velocity structure

In northeast Japan, or the Tohoku region, the Pacific plate subducts westward underneath the Eurasian plate at a rate of ~8-9 cm/yr, and its geometry has been revealed by numerous seismic studies (e.g. Zhao et al., 1992; Chen et al., 2005; Kawakatsu and Watada, 2007). Holocene arc volcanoes dominate central Tohoku and occur more sporadically in the west (Figure 3.1), lying above low velocity regions in the mantle wedge (e.g. Zhao et al., 1992, 2015; Nakajima et al., 2001; Kawakatsu and Watada, 2007). In contrast, in northeastern and southeastern Tohoku the Kitakami and Abukuma mountains are composed of Cretaceous sedimentary and plutonic rocks (e.g. Ozawa et al., 1988; Finn, 1994).
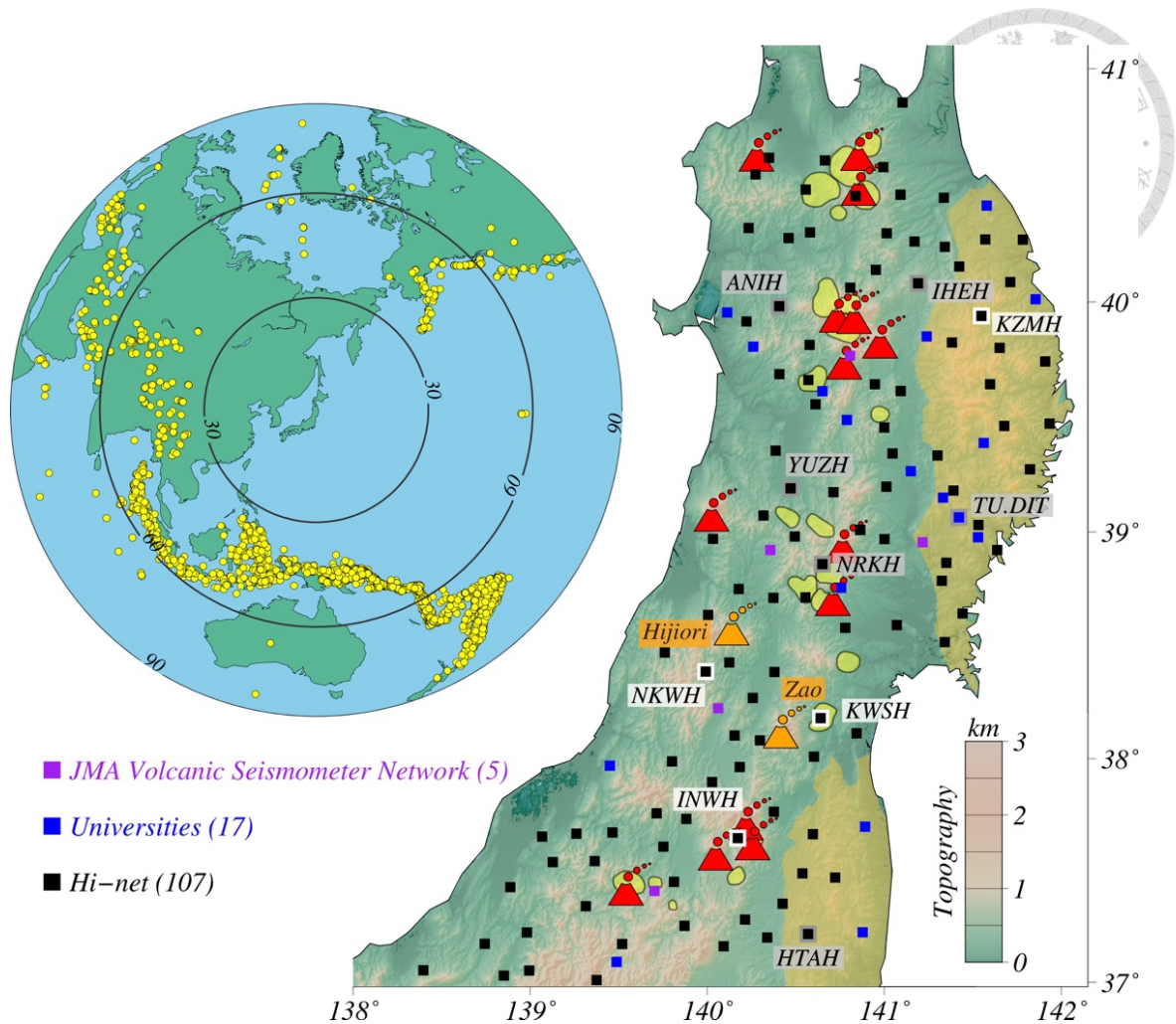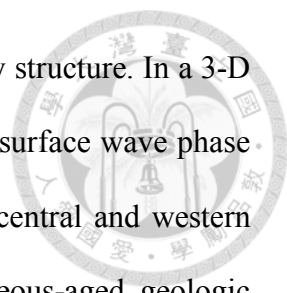
Figure 3.2 (Right) The Tohoku region and seismic stations. Purple/blue/black squares: seismic stations used in this study maintained by the JMA/Universities/NIED, respectively. Stations shown in Figure 3.3 are labeled with white backgrounds, and those in Figure 3.4 are labeled with gray backgrounds. Volcano-shaped marks: Holocene volcanoes (orange for Zao and Hijiori; red for the others). Light-yellow patches: Pliocene to Quaternary calderas (Yoshida et al., 2014; Zellmer et al., 2019). Translucent yellow patches: Cretaceous Kitakami and Abukuma mountains. (Left) Map of teleseismic events (yellow dots). A total of 1773 events with magnitudes of 5.7 or more and epicentral distances of 35°-85°, occurring from October 2004 to July 2018 were used for Ps receiver functions, and 70% of these are in the 130°-255° back-azimuth range.

This variation in magmatic activity is reflected in crustal velocity structure. In a 3-D crustal Vs model obtained by inverting 3-16 s period ambient noise surface wave phase velocities, Chen et al. (2018) found low crustal velocities beneath central and western Tohoku, whereas higher velocities correlate well with the Cretaceous-aged geologic terranes containing the Kitakami and Abukuma mountains. Below most of the active volcanoes, Vs anomalies of up to −10% are concentrated around 10 km depth, and Chen et al. (2018) interpreted these features as shallow magma reservoirs for the Holocene magmatic system. The depths of these anomalies correlate with a minimum in azimuthal anisotropy.

Zellmer et al. (2019) combined the Chen et al. (2018) crustal Vs model, volcano eruption records, and geological data to infer a contrast in magma transport processes between most volcanic centers, which are underlain by low Vs anomalies, and Zao volcano, where crustal velocities are higher. Beneath Zao volcano, which has erupted more frequently in the last 2 kyr, magma may rise more directly from the deeper crust though fault-enabled pathways. Under other volcanoes, hotter and more ductile plutonic bodies and crystal mush zones could have developed in the upper crust by repeated intrusive activity, indicating shallow magma storage before transport to the surface.

Because of their ability to image localized vertical velocity gradients, converted body wave phases have potential to delineate the boundaries of melt-rich regions in the crust. A number of studies have used converted body waves to study intra-crustal discontinuities beneath Tohoku (Nakamichi et al., 2002; Igarashi et al., 2011; Bianchi et al., 2015; Porritt and Yoshioka, 2017) including a low velocity layer associated with crustal melt beneath a localized group of volcanoes in the north (Nakamichi et al., 2002). However, much remains to be learned about crustal structure and its relationship to magma storage across the Tohoku region as a whole. In this study, we probe intra-crustal discontinuities across
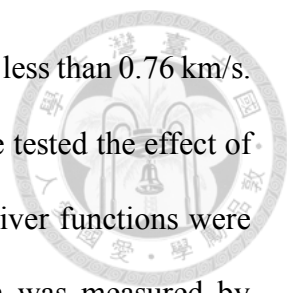
all of Tohoku using Ps phases and integrate these findings with the Chen et al. (2018) constraints on crustal shear velocities. This work provides new insight on the depths of magma storage and its proximity to volcanic centers.
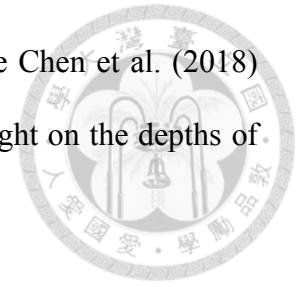
3.2 Data and Methods

For events with magnitudes of 5.7 or more and epicentral distances between 35° and 85°, occurring from October 2004 to July 2018 in the USGS NEIC global catalog, we collected data recorded by multiple seismic networks, including 126 NIED (National Research Institute for Earth Science and Disaster Prevention) Hi-net stations (Obara et al., 2005), 66 stations of the JMA (Japan Meteorological Agency) volcanic seismometer network and 56 stations deployed and maintained by Tohoku University, Tokyo University, and Hirosaki University. This dataset includes 1773 events in total, and 70% of these are in the 130°-255° back-azimuth range.
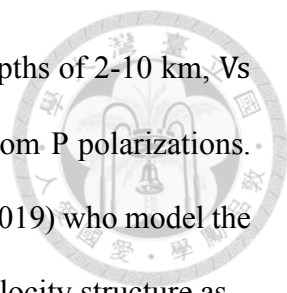
In order to calculate Ps receiver functions, P and SV waveform components were obtained using a series of processing steps. First, direct P arrivals (filtered with a 0.33-30.0 s period bandpass) were picked by an automated array-based procedure (Lekic and Fischer, 2014). Second, to accurately recover the parent (P) and daughter (SV) waveforms, Z-N-E components were rotated into Z-R-T and then transformed into P-SV-SH using the free-surface transform (Kennett, 1991). As pointed out by Park and Ishii (2018), P arrival polarizations are only sensitive to free surface Vs. In this step, an automated search was performed to find the free surface Vs value for each set of Z-R waveforms that minimized the amplitude of the P phase on the SV component in a short window around the P phase arrival time (e.g. Abt et al., 2010). The free surface Vs for each station was estimated by taking the median of individual free surface Vs values for the station. Free surface Vp was obtained by multiplying free surface Vs by 1.77, since Vp cannot be constrained by P

phases alone. Most stations had free surface Vs standard deviations of less than 0.76 km/s. For a few stations with larger free surface Vs standard deviations, we tested the effect of adding ± 0.5 km/s to the median free surface Vs. The resulting receiver functions were very similar. Third, the signal-to-noise ratio for each P waveform was measured by dividing the mean amplitude of the envelope function in a 5 s time window after the P arrival by the mean amplitude of the envelope function in a 20 s time window before the P arrival. Fourth, a slightly more restricted bandpass filter (0.5-30.0 s period) was applied to the P and SV components. This filter was chosen empirically to provide receiver functions with better signal-to-noise ratios.

Ps receiver functions were calculated by deconvolving the P component from the SV component using iterative time-domain deconvolution (e.g. Ligorria and Ammon, 1999). Deconvolution was performed over 75 s windows, which are long enough to capture direct arrivals from the crust and their reverberations, using 100 iterations but stopping when the improvement in fit between iterations was less than 1%. The deconvolved impulse response was convolved with a Gaussian function, whose half-width of 0.5 s was chosen to be narrow enough to minimize additional filtering of the signal as a result of deconvolution.

The resulting receiver functions were migrated to depth using station-specific 1-D velocity models that incorporated a number of geophysical observations, with a particular focus on the uppermost crust where the Chen et al. (2018) Vs model lacks resolution because the minimum period of its phase velocities was 3 s. In the velocity models used for migration, a 2 km thick low velocity layer (Vp of 2.5 km/s), which could represent sediments, is included based on the results of seismic reflection surveys and shallow earthquake travel-time data (Yoshii and Asano, 1972; Hasegawa et al., 1994), as well as the widespread presence of a positive phase at ~2 km in the Ps receiver functions. A

61

Vp/Vs ratio of 2 was assigned to this layer (Chen et al., 2005). At depths of 2-10 km, Vs was assumed to be the free-surface Vs determined for the station from P polarizations. This assumption is broadly consistent with the results of Park et al. (2019) who model the frequency-dependent sensitivity of free-surface velocities to shear velocity structure as a function of depth. At depths of 10-40 km, shear velocities were increased from 3.5-4.4 km/s, values that are broadly consistent with average Vs values from regional body wave tomography (Matsubara et al., 2017) and ambient noise tomography (Chen et al., 2018). At depths greater than 40 km, shear velocity was fixed at 4.4 km/s. Over depths of 2-40 km, Vp/Vs was estimated by averaging the crustal model of Matsubara et al. (2017) in separate low (< −1%), intermediate (−1% to 1%), and high (>1%) velocity regions of Tohoku defined according to the Chen et al. (2018) model; the resulting Vp/Vs values are 1.77, 1.76, and 1.73, respectively. With these customized, station-specific 1-D velocity models (e.g. Figure 3.2), time domain receiver functions were then migrated to depth.
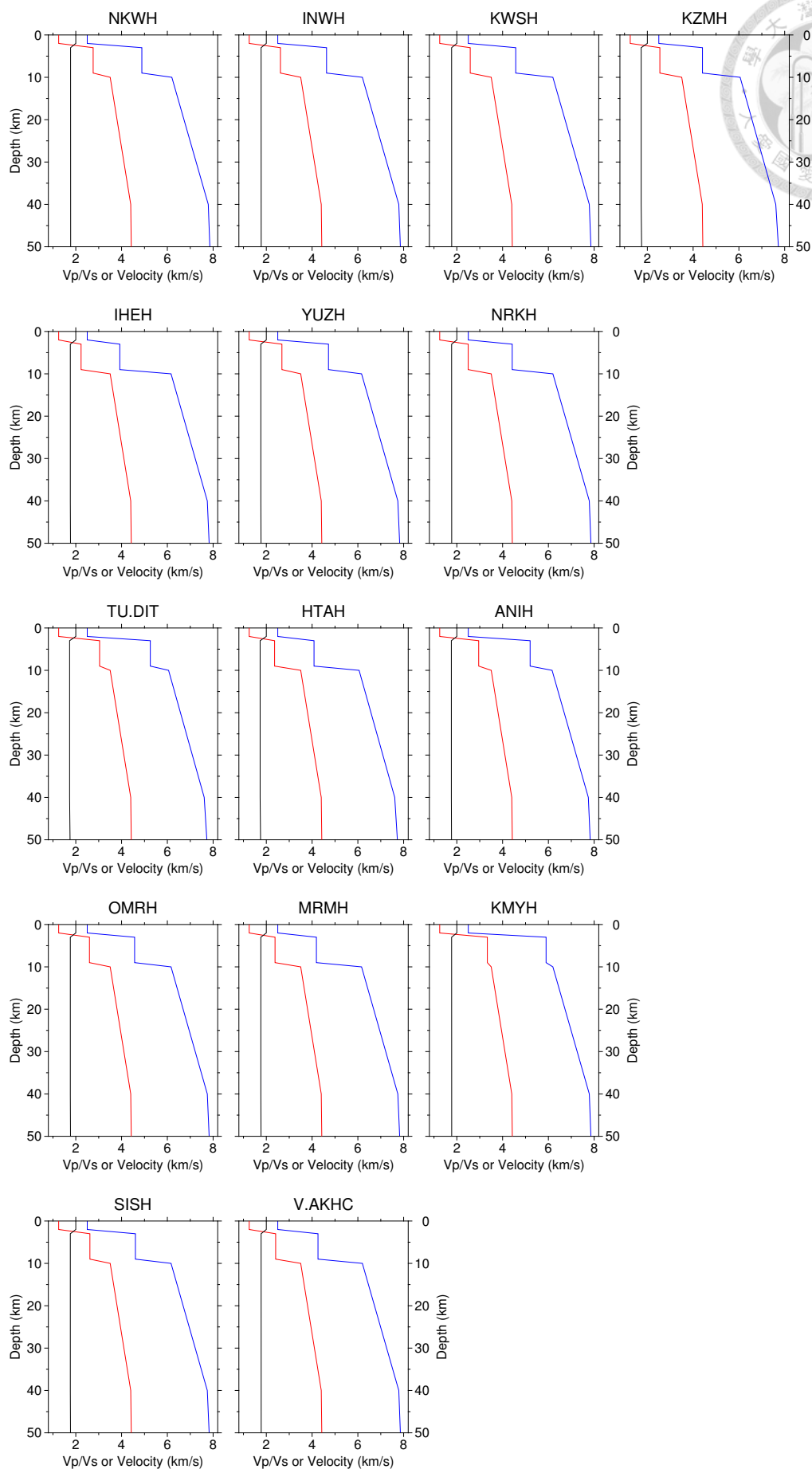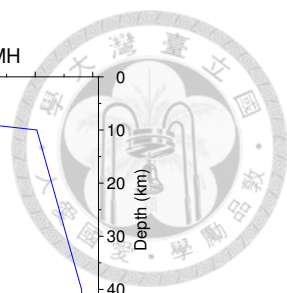
63

Figure 3.3 Station-specific 1-D velocity models for depth migration for stations shown in this study. In each panel, Vp, Vs, and Vp/Vs ratio are represented by blue, red, and black lines, respectively. Velocity models in the first row are for the stations shown in Figure 3.3; second and third rows: the six stations shown in Figure 3.4; and fourth and fifth rows: the five stations in Figure 3.6.

Migrated receiver functions were assessed for quality and binned by back-azimuth. Because most events lie at back-azimuths of 130° -255°, we focused on this range. (Examples of receiver functions for 0°-360° back-azimuths are shown in Figures. 3.8-3.11) All receiver functions with a signal-to-noise ratio larger than 3 were binned in 2° back-azimuth intervals, and stations where the binned receiver functions were typically noisy or stable in only a limited back-azimuthal range were discarded. 87% of Hi-net stations but only 18% of stations from other two networks were retained, reflecting the low-noise borehole environments of Hi-net stations. The distribution of retained stations is shown in Figure 3.1.

Examples of migrated receiver functions in 2° back-azimuth bins are shown in Figure 3.3 for Hi-net stations NKWH, INWH, KWSH, and KZMH. In these examples, only the bins with 5 or more receiver functions are included. Red (blue) phases indicate velocity increases (decreases) with depth; right panels show the stack for the 130°-255° back-azimuth range. The first three of these stations show positive, negative and then positive Ps phases from the near surface to 40 km depth. At stations NKWH, INWH, and KWSH, the negative Ps phase is consistently observed at depths of 8-10 km, indicating a decrease in velocity at these depths. In contrast, at station KZMH, which lies in the Kitakami terrane in eastern Tohoku, a statistically significant negative Ps arrival in the shallow crust is not observed. The prevalence of shallow crustal negative Ps phases in

central and western Tohoku is also reflected in the receiver function stacks for stations IHEH, YUZH, NRKH (Figure 3.4), although the absence of a shallow negative phase at station ANIH shows that such phases are not ubiquitous in this region. Stations TU.DIT and HTAH, which lack a shallow negative phase, are more typical of the eastern Kitakami and Abukuma terranes. Receiver functions as a function of back-azimuth for the Figure 3.4 stations appear in Figure 3.5 and Figure 3.10. Receiver functions for additional stations appear in Figure 3.6.
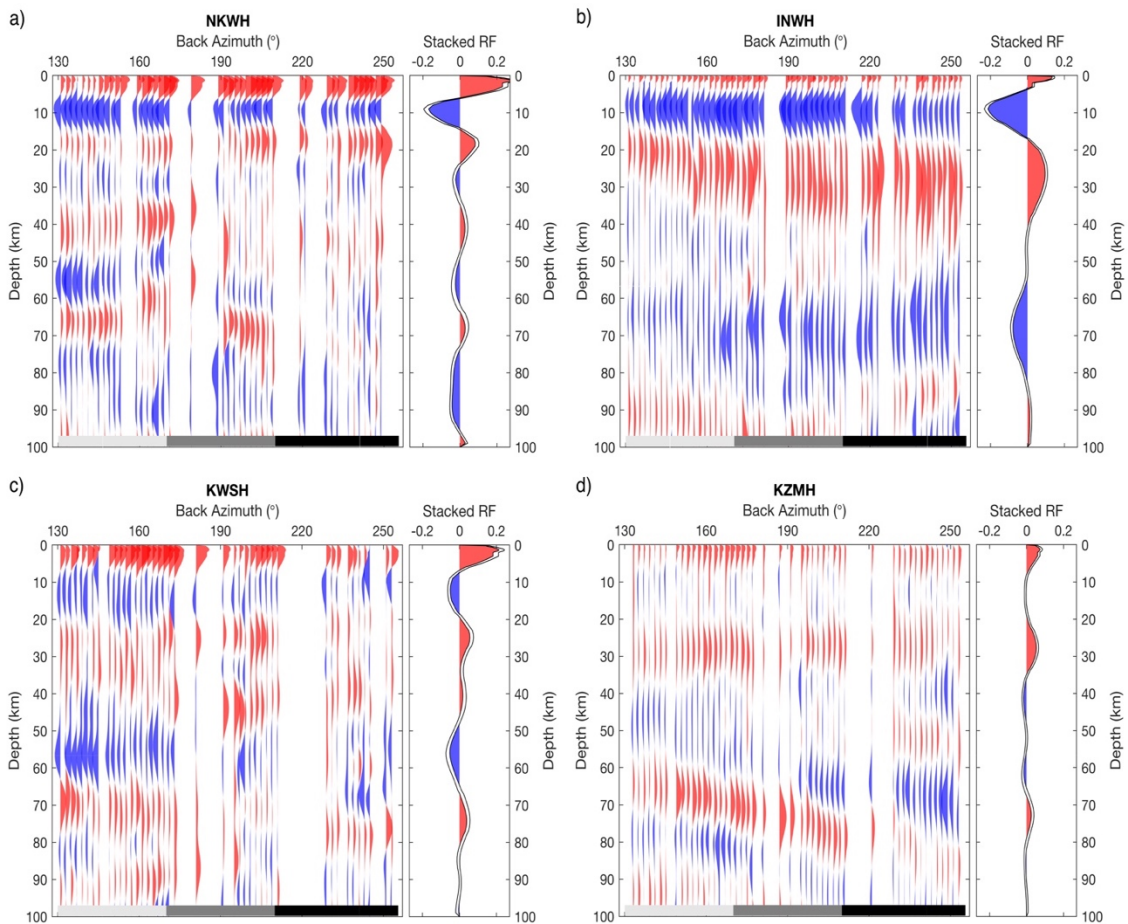
Figure 3.4   Examples of migrated Ps receiver functions in 2° back-azimuth bins for Hi-net stations NKWH, INWH, KWSH, and KZMH. In these examples, only bins with 5 or more receiver functions are included. Red (blue) phases indicate velocity increases (decreases) with depth; right panels show the stack (with two standard deviation

65

uncertainties shown by black lines) for the entire 130°-255° back-azimuth range. At the bottom of the left panels, light-gray, dark-gray, and black bars denote three different back-azimuth ranges: 130°-170°, 170°-210°, and 210°-255°. At NKWH, INWH, and KWSH, negative Ps phases indicate a decrease in velocity at 8-10 km. KZMH, in the Kitakami terrane in eastern Tohoku, does not show a negative Ps arrival in the shallow crust.

66
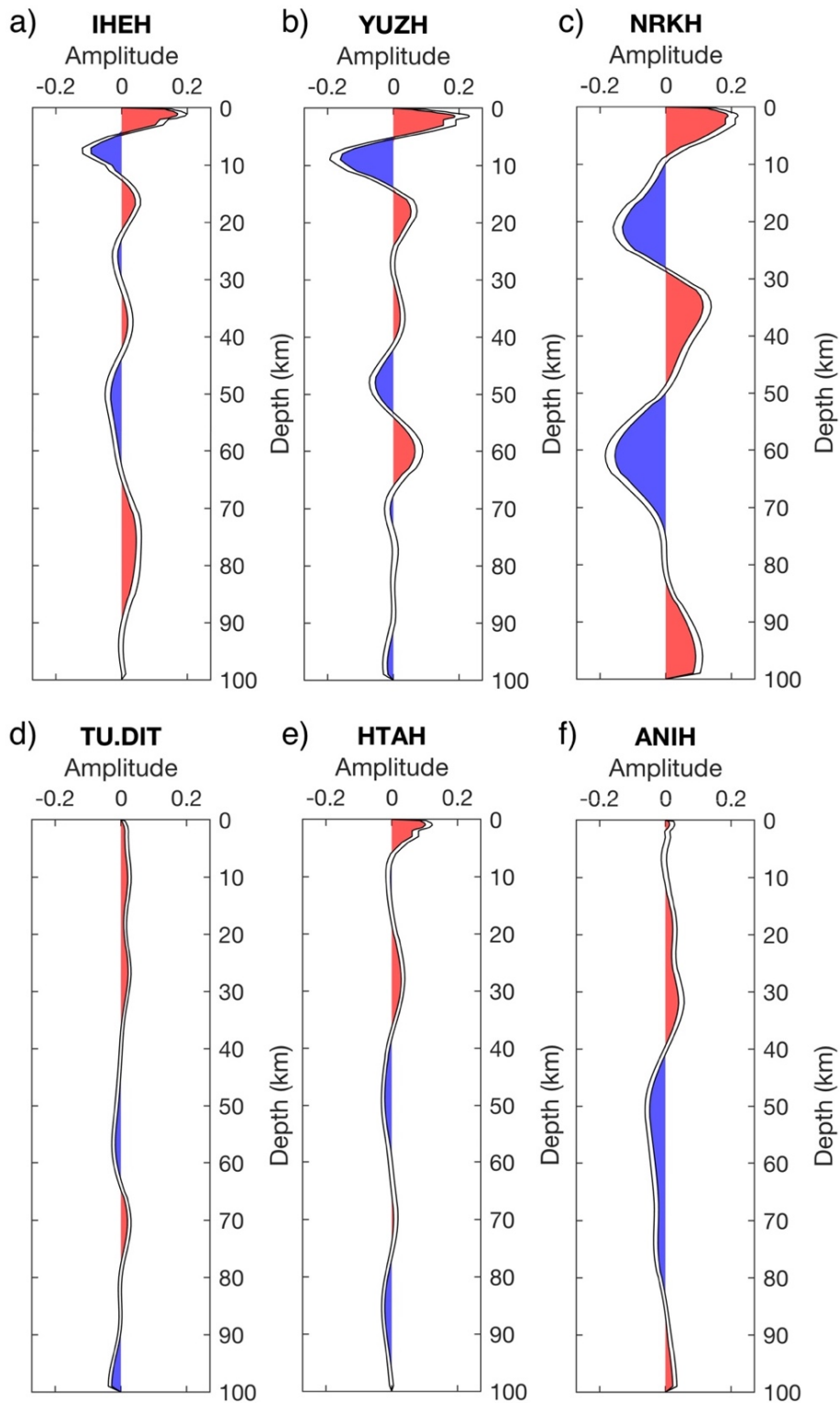
Figure 3.5 Examples of migrated, stacked Ps receiver functions for 130°-170° back-azimuths for stations in the central volcanic belt, (a) IHEH, (b) YUZH, and (c) NRKH; the fore-arc region, (d) TU.DIT, (e) HTAH; and the back-arc region, (f) ANIH. In each

panel, red (blue) phases indicate velocity increases (decreases) with depth; two standard deviation uncertainties shown by black lines. Stations are labeled with gray backgrounds in Figure 3.1. IHEH and YUZH (near Pliocene-Quaternary calderas) show negative phases in the 5-15 km depth range. NRKH shows a broader negative phase with peak at 20 km, resulting from averaging of negative phases at ~20 km and ~8 km at back-azimuths of 130° -210° and 210° -250°, respectively (Figure 3.5b); this variation is consistent with significant lateral variations in the depth of the corresponding discontinuity. TU.DIT, HTAH, and ANIH are not close to volcanic centers and lack negative phases in the shallow crust.
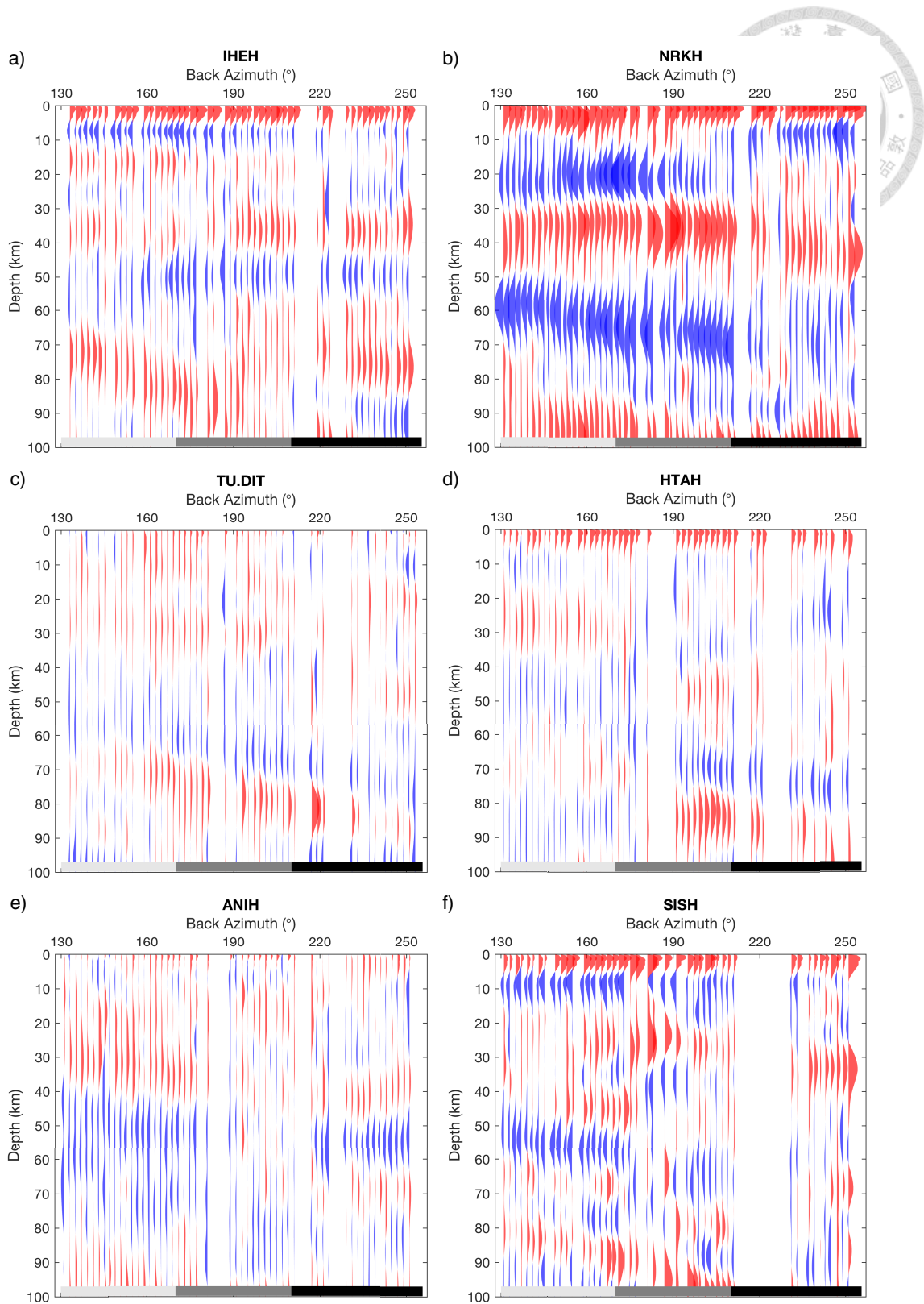
Figure 3.6 Receiver functions as a function of back-azimuth for stations in Figure 3.4:
(a) IHEH, (b) NRKH, (c) TU.DIT, (d) HTAH, (e) ANIH and for a station in Figure 3.6:
(f) SISH.

69
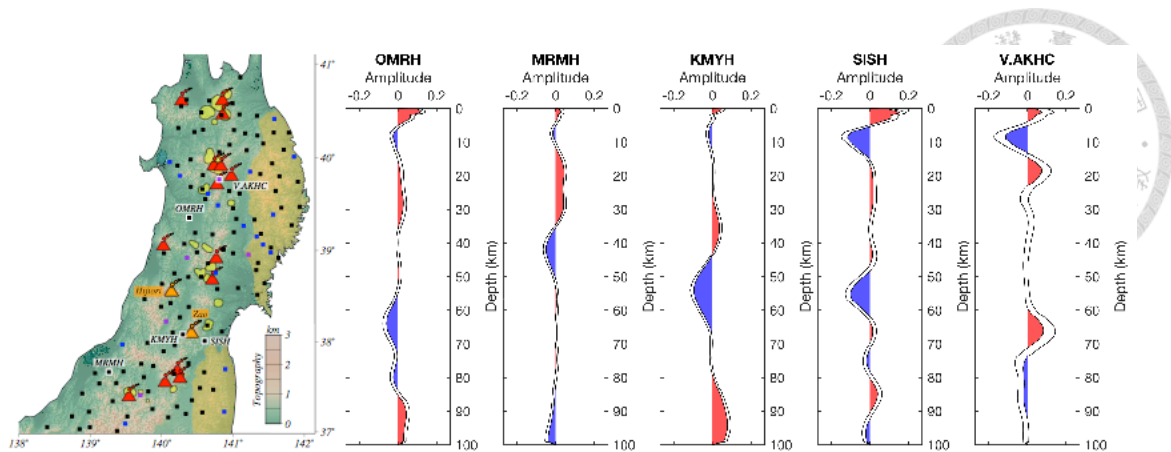
Figure 3.7 Additional examples of migrated, single receiver function stacks from a 130°-175° back-azimuth range. Left panel shows the locations of the five stations. Stations are in: (1) the back-arc region (OMRH and MRMH which both lack of negative phases in shallow crust); (2) near Zao volcano (KMYH which does not show a negative phase); (3) southeast of Zao (SISH whose significant amplitude Ps conversions hint at possible nearby zones of upper-crust melt storage); (4) the northern volcanic group (V.AKHC which shows a negative phase in the upper crust).

To assess the overall depth distribution of both positive and negative phases, including potential depth variations with back-azimuth as shown at station NRKH, receiver functions were binned in three different back-azimuth ranges: 130° -170° , 170° -210° , and 210°-255° (shown by light-gray, dark-gray, and black bars at the bottom of the left panels in Figure 3.3). For a specific station, in each back-azimuth range, at least 150 receiver functions with a signal-to-noise ratio larger than 3 were required for the phases to be picked. The depth distribution of all picked phases is shown in Figure 3.7. Phase depths are reported only if the absolute amplitude of the phase is greater than twice the standard deviation of the amplitude.
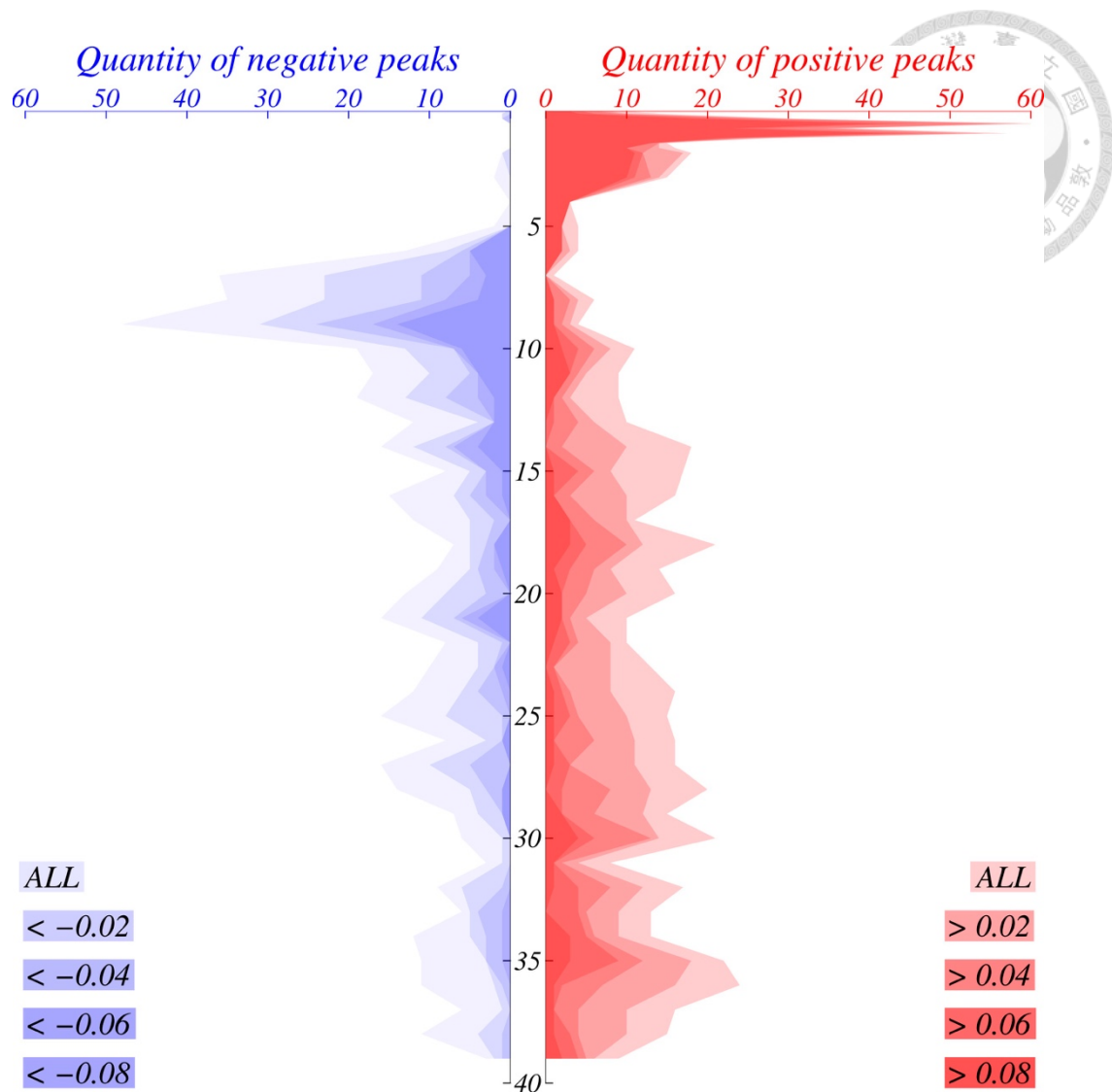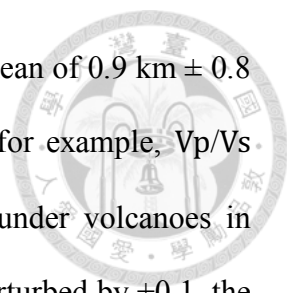
Figure 3.8   Distribution of Ps phases versus depth. The count of phases picked from the three back-azimuthal bins at all stations that meet quality criteria, with warm(cool) colors for positive(negative) Ps phases. The intensities of shading correspond to different phase amplitude thresholds. At depths of less than 5 km strong positive peaks are prevalent, at depths of 5-10 km negative phases are dominant, and at greater depths, both positive and negative phases are observed.

Uncertainties in discontinuity depths for the observed crustal phases were estimated by perturbing the velocity model used in the migration. If Vs at 2-10 km (taken from the free surface velocity analysis) is perturbed by ± 0.5 km/s, the corresponding shifts in

discontinuity depth for all discontinuities deeper than 2 km have a mean of 0.9 km ± 0.8 km (one standard deviation). Vp/Vs in the crust can vary widely; for example, Vp/Vs values of more than 1.9 Vp/Vs have been inferred for the crust under volcanoes in Kamchatka (Koulakov et al., 2017). If Vp/Vs between 2-40 km is perturbed by ±0.1, the mean depth shift for discontinuities deeper than 2 km is 2.2 km ± 1.8 km, and for the negative discontinuities in the 2-15 km depth range the mean shift is 1.1 km ± 0.6 km. Thus the depths of the discontinuities are likely accurate to within a few kilometers.

A question that arises when interpreting Ps receiver function phases is whether they are influenced by the presence of azimuthal anisotropy or a significant dip on the discontinuity that produces them. To assess these factors, we compared the SV receiver functions to SH receiver functions obtained by deconvolving P from SH components over back-azimuths of 0°-360° (e.g. Figures. 3.8-3.11). Dipping discontinuities and azimuthal anisotropy will generate phases on SH receiver functions at depths comparable to those on SV receiver functions (e.g. Schulte-Pelkum and Mahan, 2014). For stations NKWH (Figure 3.8), KWSH (Figure 3.9) and YUZH (Figure 3.10), energy on the SH receiver functions in the 5-15 km depth range is small, and the negative SV receiver function phases at NKWH and KWSH show little variation in amplitude with back-azimuth, all of which is consistent with largely isotropic velocity decreases at horizontal boundaries. In contrast, SH receiver functions at station INWH (Figure 3.11) contain larger amplitudes in the 5-15 km depth range, and back-azimuthal variations in both SH and SV amplitudes are consistent with predictions for a dipping isotropic discontinuity (Schulte-Pelkum and Mahan, 2014).

72

Figure 3.9 (Upper) Receiver functions over 0°-360° back-azimuths for (a) SV and (b) SH components for station NKWH. In these 2° back-azimuth bins, only the bins with 5 or more receiver functions are included. The number of receiver functions in each 30° back-azimuth range is shown below the back-azimuth axis. (Lower) Peak amplitudes within the 5-15 km depth range are shown by blue(red) dots for negative(positive) phases. At depths of 5-15 km, NKWH shows relatively stable negative amplitudes on SV receiver functions and typically weak amplitudes on SH receiver functions, suggesting a horizontal isotropic interface with a velocity decrease.

Figure 3.10 (Upper) Receiver functions over 0°-360° back-azimuths for (a) SV and (b) SH components for station KWSH. In these 2° back-azimuth bins, only the bins with 5 or more receiver functions are included. The number of receiver functions in each 30° back-azimuth range is shown below the back-azimuth axis. (Lower) Peak amplitudes within the 5-15 km depth range are shown by blue(red) dots for negative(positive) phases. At depths of 5-15 km, KWSH SV receiver functions contain consistently negative phases, and SH receiver functions have much smaller amplitudes at most back-azimuths. Based on this comparison, the KWSH phases were modeled with a horizontal, isotropic interface with a velocity decrease.
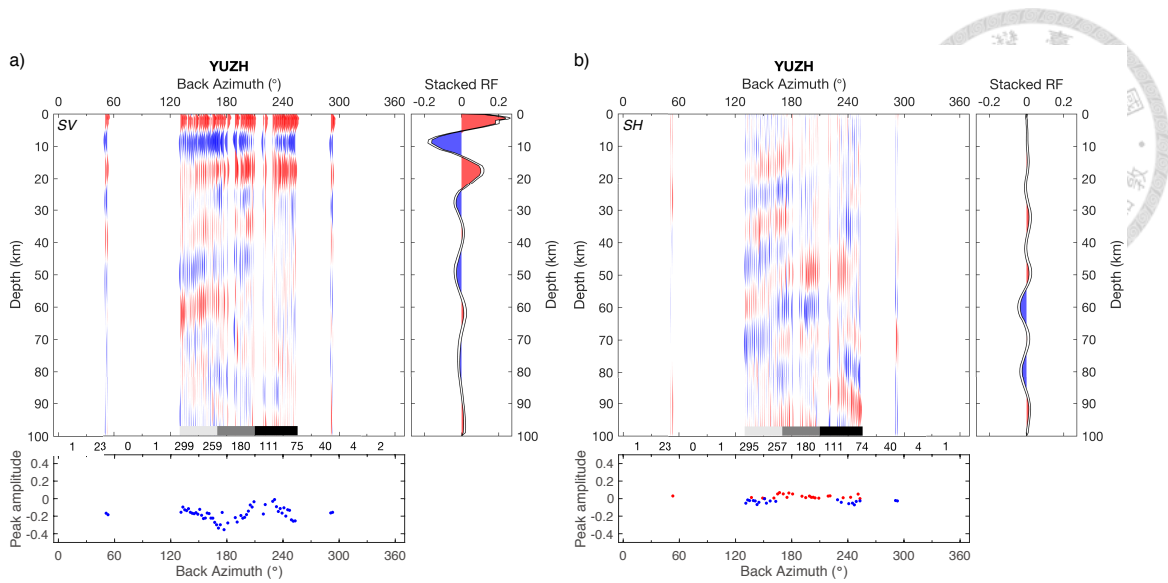
Figure 3.11 (Upper) Receiver functions over 0°-360° back-azimuths for (a) SV and (b) SH components for station YUZH. In these 2° back-azimuth bins, only the bins with 5 or more receiver functions are included. The number of receiver functions in each 30° back-azimuth range is shown below the back-azimuth axis. (Lower) Peak amplitudes within the 5-15 km depth range are shown by blue(red) dots for negative(positive) phases. At depths of 5-15 km, YUZH SH receiver functions have minimal amplitudes. SV receiver functions show some amplitude variation, but the absence of significant SH phases indicates that the SV amplitude variation is not due to anisotropy or a dipping interface, but rather to interference with adjacent phases. A horizontal isotropic interface with a velocity decrease is inferred for this station.
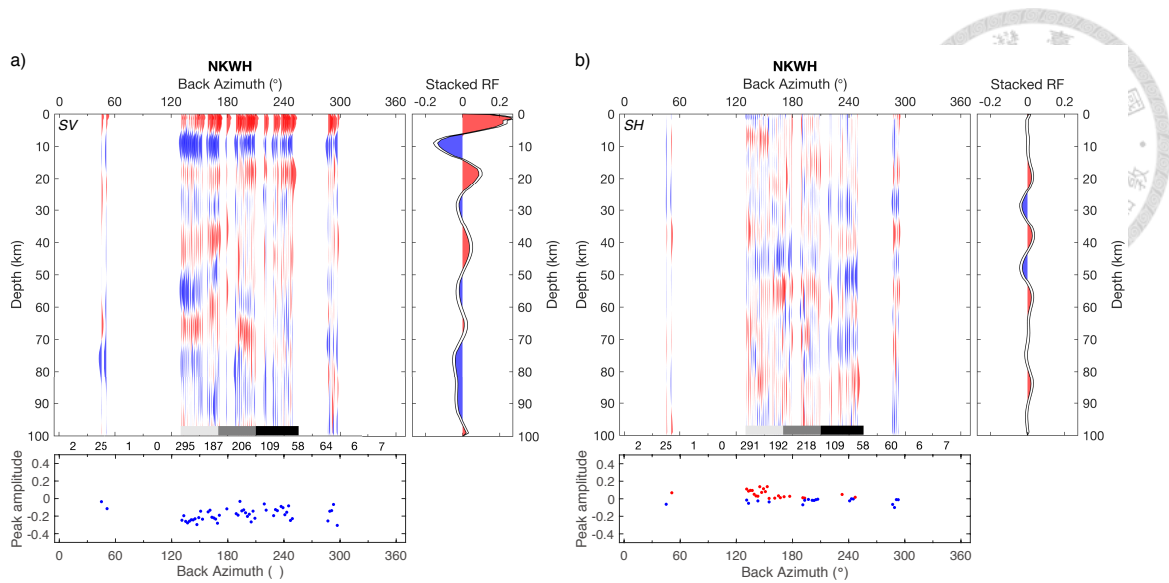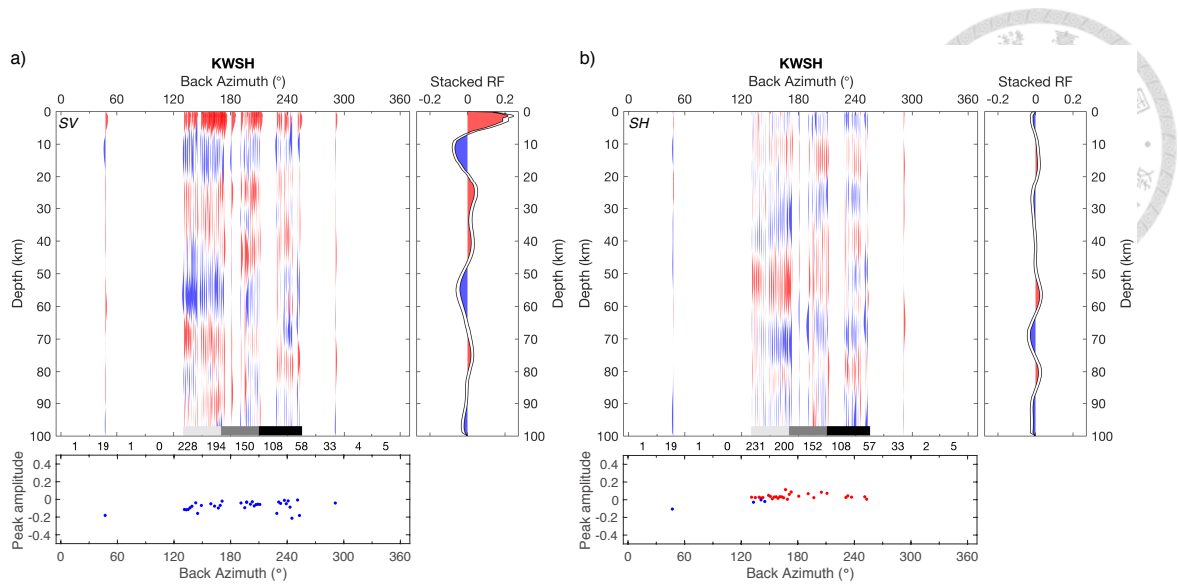
75
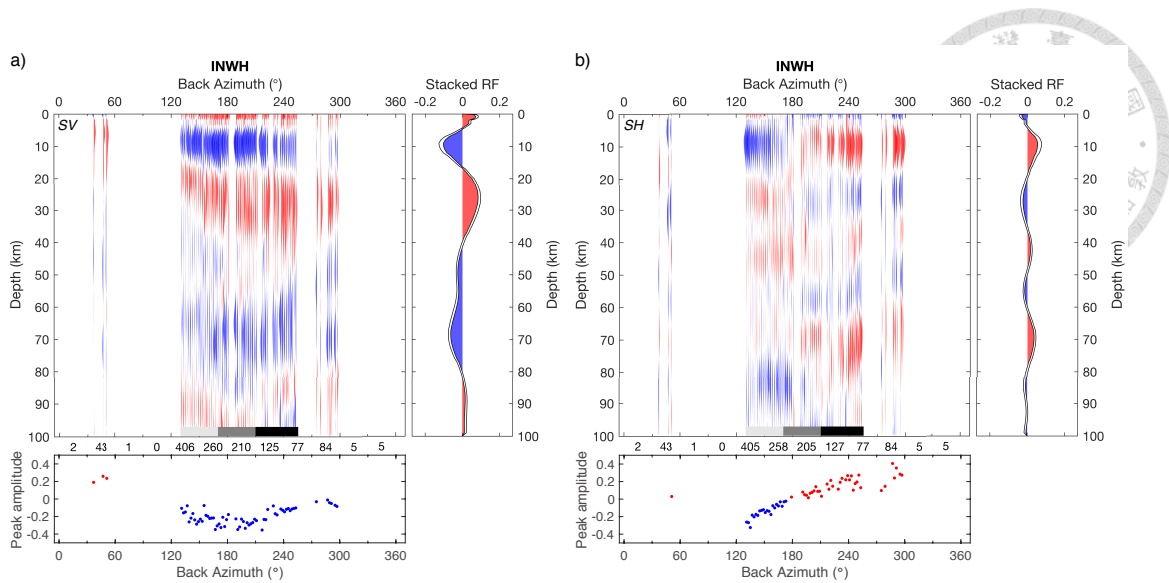
Figure 3.12 (Upper) Receiver functions over 0°-360° back-azimuths for (a) SV and (b) SH components for station INWH. In these 2° back-azimuth bins, only the bins with 5 or more receiver functions are included. The number of receiver functions in each 30° back-azimuth range is shown below the back-azimuth axis. (Lower) Peak amplitudes within the 5-15 km depth range are shown by blue(red) dots for negative(positive) phases. At depths of 5-15 km, both SV and SH receiver functions manifest strong and consistent amplitude variations, including polarity shifts, as a function of back-azimuth. These patterns, and the presence of a SH phase at the surface whose polarity is the opposite of the SH phase at 5-15 km, are consistent with a dipping isotropic interface (Schulte-Pelkum and Mahan, 2014).

3.3 Results: observed crustal discontinuities and their origin

The crustal discontinuities observed in the binned receiver functions show a distinctive distribution with depth. In Figure 3.7, the number of phases picked from the three back-azimuthal bins at all stations in 1 km depth bins are indicated by warm(cool) colors for positive(negative) Ps phases. The intensities of shading correspond to different phase amplitude thresholds. At depths of less than 5 km, strong positive peaks are

76

dominant. In contrast, negative phases are more common in the 5-13 km depth range, and are particularly dominant at depths of 5-10 km. At greater depths, both positive and negative phases are observed.

To further decipher the origin of the observed Ps phases, in Figure 3.12 phases are separated into four depth ranges (0-5, 5-15, 15-30, 30-40 km) and plotted at the location of the Ps conversion point (assuming the migration velocity model) on top of the vertically-averaged Vs for that layer from Chen et al. (2018). Separate plots of receiver function phases and Vs anomalies appear in Figure 3.13, and a plot comparable to Figure 3.12 but with absolute shear velocities is in Figure 3.14. Positive(negative) phases are shown by translucent white(black) circles whose radii are proportional to the peak phase amplitude. The positive phases that dominate at 0-5 km (left panel) are distributed across Tohoku, consistent with a widespread low velocity layer near the surface. These arrivals are consistent with the base of a shallow low velocity layer that has been widely imaged in the Tohoku region (e.g. Yoshii and Asano, 1972; Hasegawa et al., 1994) and that in many places can be attributed to sedimentary layers. At depths of 30-40 km, positive phases are more prevalent. Some of the positive Ps energy at depths of 30-40 km is likely related to the crust-mantle boundary, given that active source and earthquake studies indicate Moho depths around 30 km along the eastern and western coasts with depths up to 40 km observed beneath the central volcanic belt (Iwasaki et al., 2013). However, as shown later in this paper, at some stations reverberations from shallower discontinuities may complicate Ps conversions from the Moho.
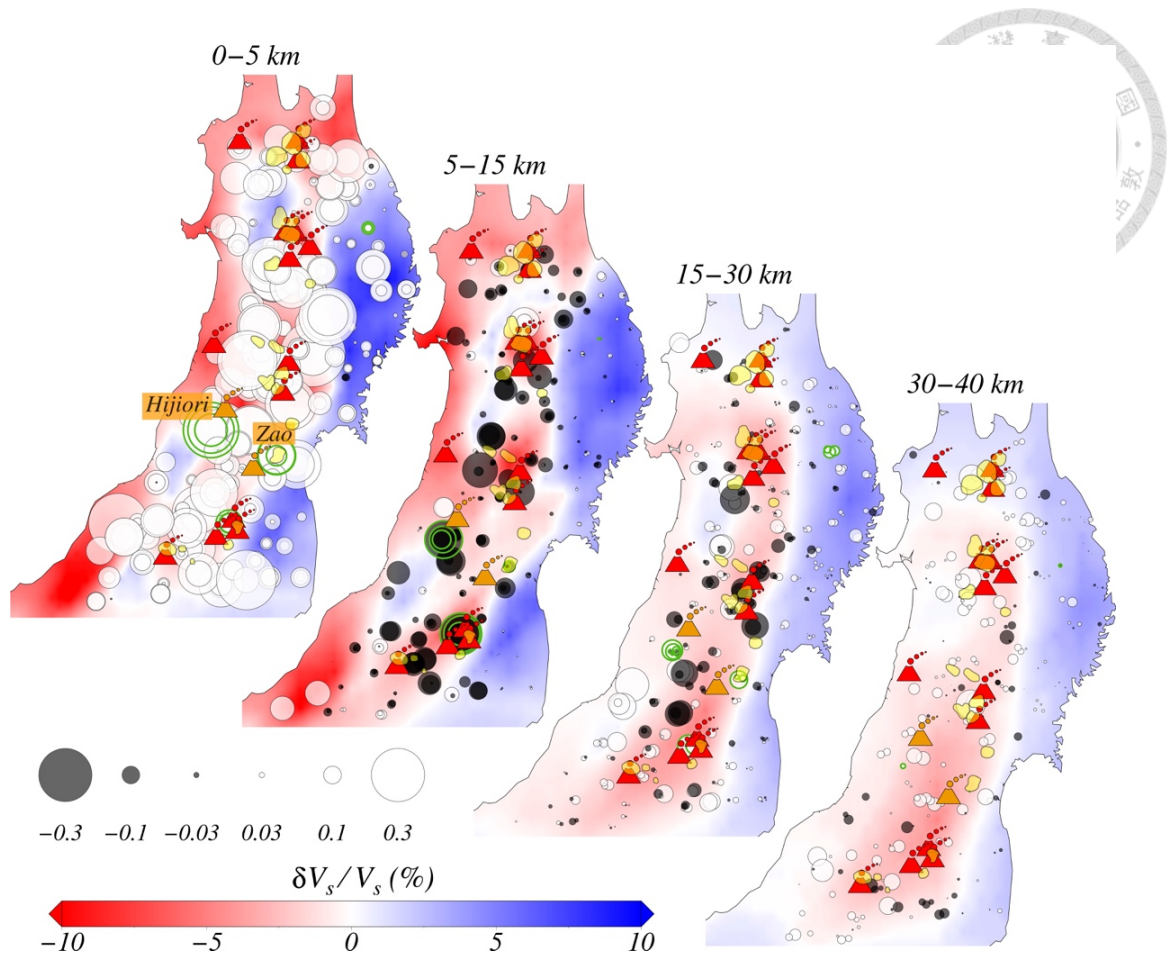
Figure 3.13 Geographic distribution of Ps phases. Ps amplitudes plotted at conversion points, grouped into four depth ranges (0-5, 5-15, 15-30, 30-40 km) and superimposed on the vertically-averaged Vs anomaly for that layer from Chen et al. (2018). Positive(negative) phases are shown by translucent white(black) circles whose radii are proportional to peak phase amplitude. Phases for stations NKWH, INWH, KWSH, and KZMH are highlighted by green outlines. Volcano-shaped marks: Holocene volcanoes (orange for Zao and Hijiori; red for the others). Light-yellow patches: Pliocene to Quaternary calderas (Yoshida et al., 2014; Zellmer et al., 2019). At 0-5 km (left panel) positive phases are distributed across Tohoku, consistent with a widespread shallow low velocity layer. At 5-15 km the largest negative phases lie in the central volcanic belt, while in the high velocity terranes in eastern Tohoku phase amplitudes are typically small or phases are absent. At 15-30 km, a mix of positive and negative phases are observed, but
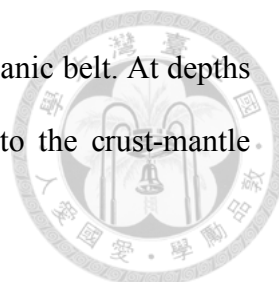
again the largest negative phases are concentrated in the central volcanic belt. At depths of 30-40 km, positive phases are more prevalent and may relate to the crust-mantle boundary.
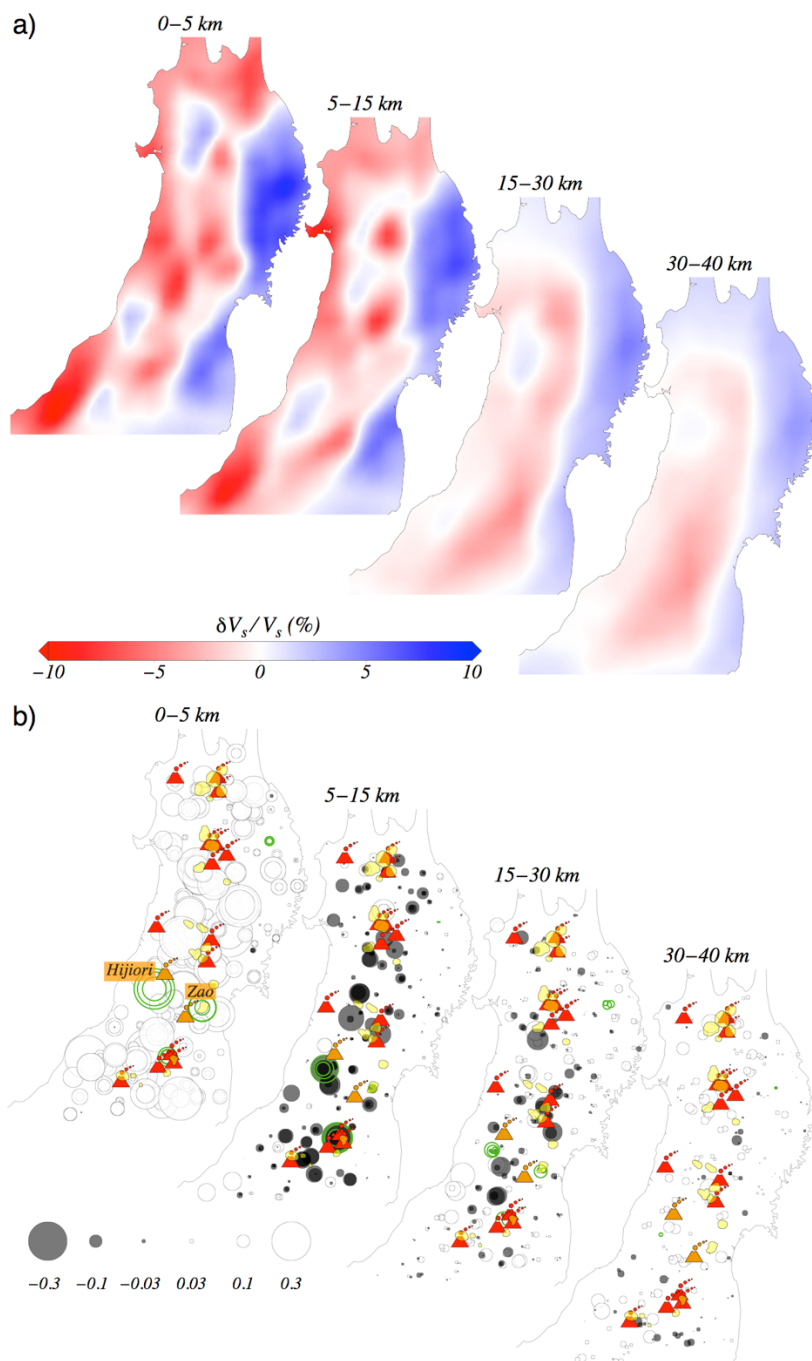
Figure 3.14   The same as Figure 3.12 except showing (upper) shear velocity anomalies and (lower) receiver function peak amplitudes with other symbols in four depth ranges.

79
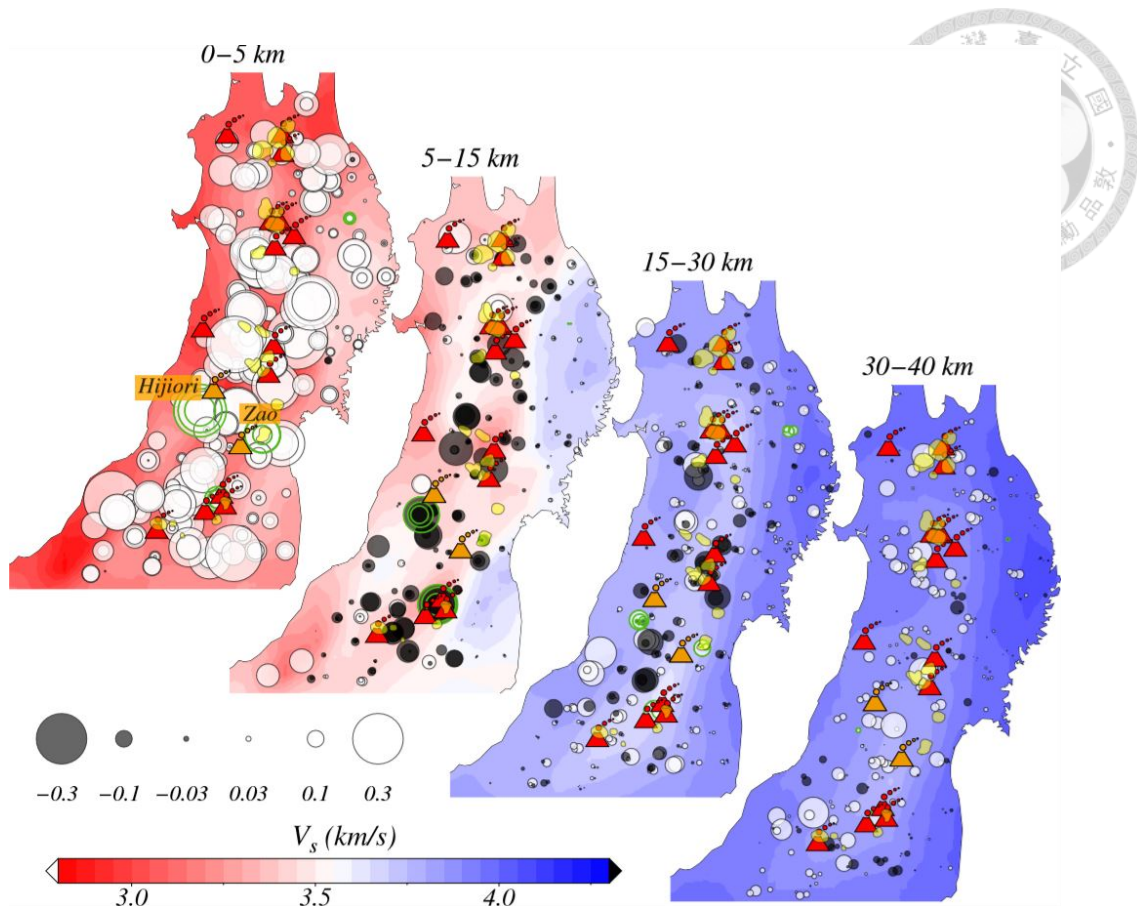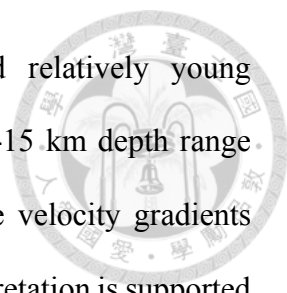
Figure 3.15 The same as Figure 3.12 except showing absolute shear velocity in the background.

Negative Ps phases in the 5-30 km depth range largely occur in the low velocity regions of central and western Tohoku. In the 5-15 km depth range, where negative phases are dominant, 65% of negative phases (and 73% of negative phases with an absolute amplitude >0.04) have conversion points in regions of Tohoku where the Chen et al. (2018) Vs model indicates negative velocity anomalies. The largest negative phases largely lie in the central volcanic belt. In contrast, in the high velocity terranes in eastern Tohoku phase amplitudes are typically small or phases are absent in the 5-15 km depth range; only 44% of stations show negative phases and their average amplitude is merely −0.02. At depths of 15-30 km, a mix of positive and negative phases is observed, but again the largest negative phases are concentrated in the central volcanic belt.

80

Their strong association with low velocity anomalies and relatively young magmatism provides evidence that the negative Ps phases in the 5-15 km depth range represent conversions from vertically-localized downward negative velocity gradients that mark the upper boundaries of melt-rich crustal layers. This interpretation is supported by the spatial relationships of the observed Ps phases (here shown with absolute amplitudes of more than 0.05) and the Chen et al. (2018) velocity anomalies in three profiles (Figure 3.15; see Figure 3.16 for a version with absolute velocities). Negative phases at depths of 5-10 km are mostly located at the upper margins of pronounced low velocity bodies beneath volcanic centers that are consistent with zones of upper crustal melt storage (e.g. Chen et al., 2018; Huber et al., 2019; Zellmer et al., 2019). Examples include profile A-A′ at distances of 50-75 km, profile B-B′ at distances of 100-110 km, and profile C-C′ at distances of 20-40 km, 110-150 km, 190-225 km, and 340-365 km. In some cases the nominal conversion depth of the negative Ps phase does not exactly align with the maximum negative vertical velocity gradient at the top of the low Vs zones in the Chen et al. (2018) model. However, considering that Ps depths have uncertainties of a few kilometers and the vertical resolution in the Chen et al. (2018) model is limited by the ~2 km thicknesses of the upper four model layers, these independent observations agree.
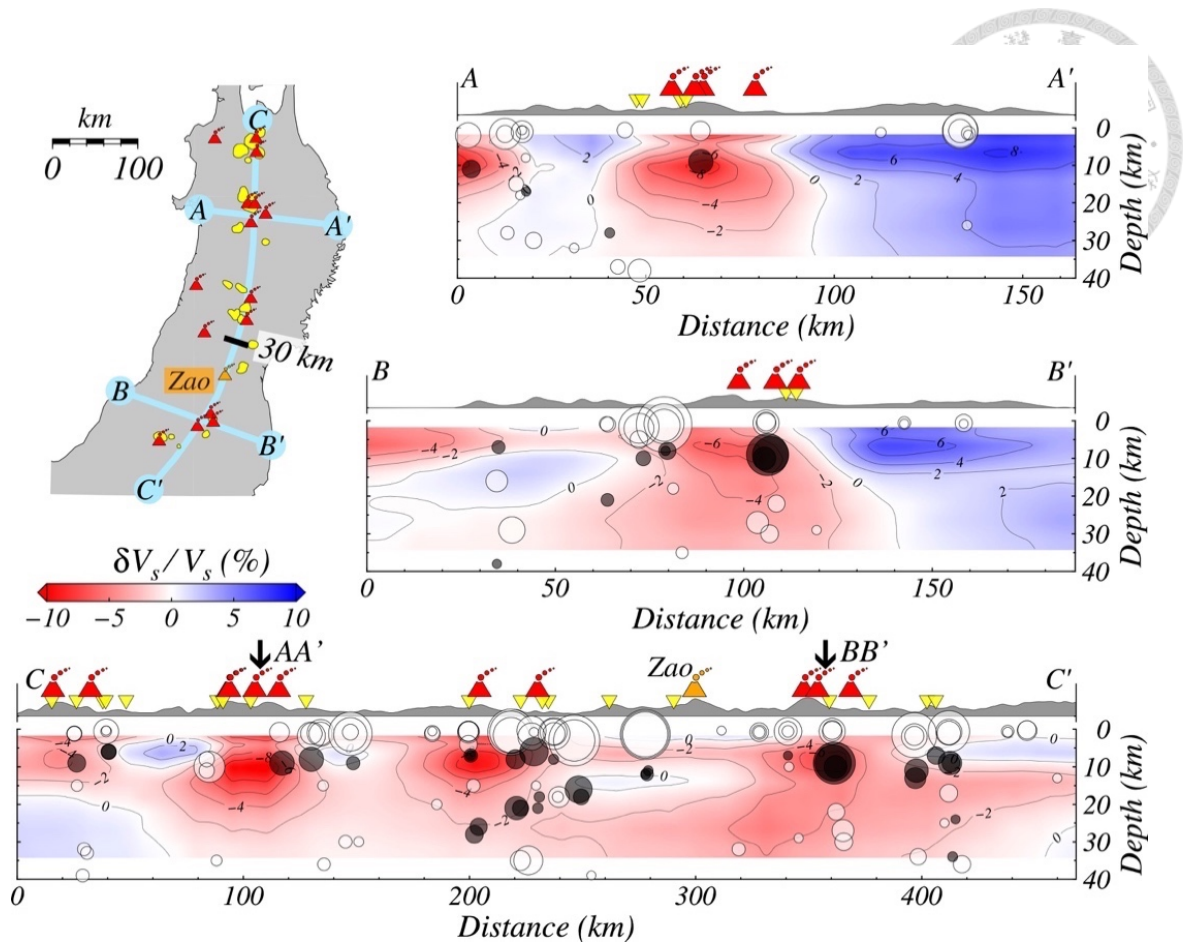
Figure 3.16 Vertical cross-sections showing Ps amplitudes and the Chen et al. (2018) velocity model. Map in upper left panel shows the locations of the three cross-sections (light-blue lines). Profiles A-A′ and B-B′ retain true horizontal/vertical ratio, but in Profiles C-C′ the ratio is reduced to 0.6 for illustration purposes. Ps phase amplitudes are shown if their absolute amplitudes are more than 0.05 and their conversion points lie within 15 km of the profile. Positive(negative) phases are shown by translucent white(black) circles whose radii are proportional to peak phase amplitude. Volcano-shaped marks: Holocene volcanoes (orange for Zao; red for others). Pliocene-Quaternary calderas (Yoshida et al., 2014; Zellmer et al., 2019) are shown by light-yellow patches in left-top map and also by inverted-triangles in three vertical cross-sections. The strong association of low velocity anomalies and young volcanoes provides evidence that the negative Ps phases in the 5-15 km depth range represent conversions from the upper

82

boundaries of melt-rich crustal layers. Negative Ps phase depths and maximum negative vertical velocity gradients at the top of the low Vs zones agree well, taking into account depth uncertainties.
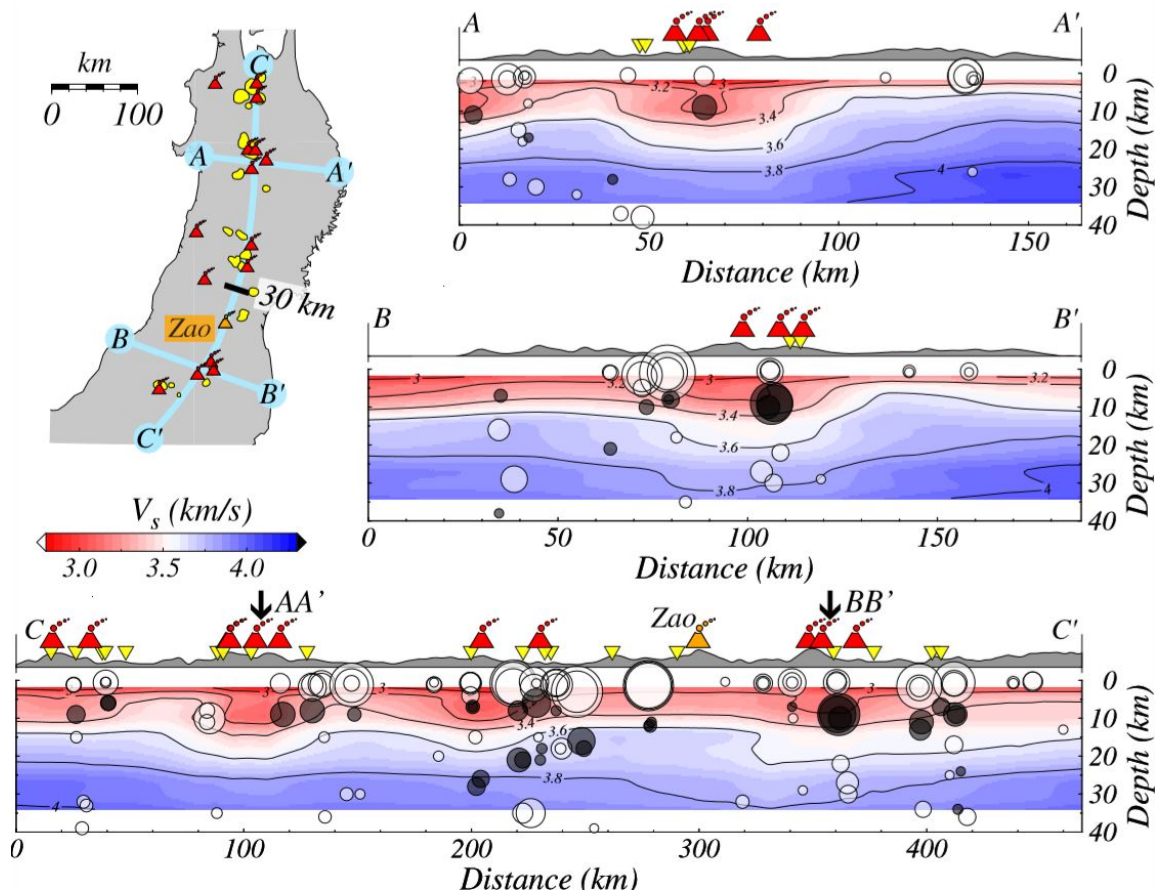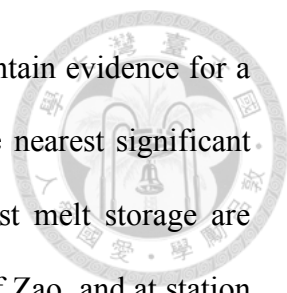
Figure 3.17 The same as Figure 3.15 except showing absolute shear velocity in the background.
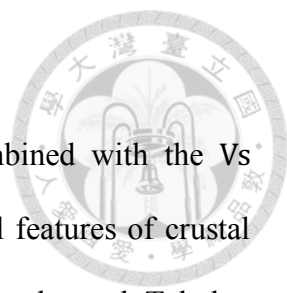
Zao volcano (profile C-C′ at a distance of 300 km) is an exception in that it lacks clear evidence for a zone of high melt fraction at depths of 5-10 km. As previously mentioned, Zellmer et al. (2019) interpret the absence of a low velocity anomaly in the Chen et al. (2018) tomography to represent the absence of a large melt-rich zone beneath Zao. This interpretation is supported by the Ps conversions closest to Zao (KMYH, Figure

83

3.6) which show at most a very small negative phase and do not contain evidence for a large vertically-localized velocity reduction in the upper crust. The nearest significant amplitude Ps conversions that indicate nearby zones of upper-crust melt storage are recorded at station SISH (Figures. 3.5 and 3.6), ~40 km to the SE of Zao, and at station KWSH (Figures. 3.3c and 3.9), which coincides with a young caldera ~60 km to the NE of Zao (e.g. the 5-15 km map in Figure 3.12). Chokaisan volcano (Figure 3.12, about 50 km to the NNW of Hijiori) is likely also an exception given that the station directly to its south lacks a significant negative phase at depths of 5-15 km.

The Ps phases reveal additional nuances of crustal structure that may also reflect crustal melt storage. In several cases, most notably on profile B-B′ at distances of 60-80 km and profile C-C′ at distances of 390-415 km, negative Ps phases in the 10-20 km depth range lie on a significant negative velocity gradient that is located 20-40 km away from the nearest volcanic center. These features may represent the margins of deeper crustal melt storage zones. The velocity reductions in the Chen et al. (2018) model associated with these phases are small, possibly because of modest melt fractions. In addition, a second and deeper (15-30 km) band of negative Ps conversions on profile C-C′ (distances of 200-250 km) could represent the top of a deeper zone of melt storage. Although the Chen et al. (2018) model does not contain a clear, correlated negative Vs gradient, the absence of such a gradient may be due to a lack of resolution in the model. Finally, some of the positive Ps conversions, which are largely observed at depths of 15 km or more, could represent the lower reaches of low velocity layers created by the presence of melt. This interpretation is particularly applicable to positive phases at depths that are too shallow to be consistent with regional Moho depths (Iwasaki et al., 2013) (e.g. positive phases observed at depths of <25 km on profile C-C′).
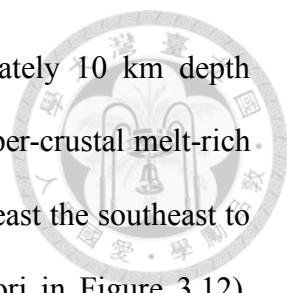
3.4   Discussion

To summarize, crustal Ps conversions beneath Tohoku, combined with the Vs tomography from Chen et al. (2018), provide constraints on several features of crustal structure that have implications for how melt is distributed in the crust beneath Tohoku. The most robust result is the correlation of negative Ps phases with the upper boundaries of low velocity zones at depths of 5-10 km. These features likely represent the upper boundaries of melt-rich layers, while deeper positive phases may represent more gradual velocity gradients at the lower boundaries of these layers. Although less common and consistent, some groups of deeper negative Ps phases at depths of 10-30 km indicate negative velocity gradients that may reflect zones of melt storage at greater depths and larger distances from volcanic centers. In this section we: (1) model the velocity structure implied by Ps conversions at two Tohoku stations; (2) calculate bounds on crustal melt implied by this velocity structure; and (3) explore the implications of crustal structure across Tohoku for models of crustal melt storage.

3.4.1   Modeling velocity structure

To obtain constraints on shear velocity that can serve as a benchmark for the interpretation of the observed Ps phases, we modeled the Ps receiver functions at station NKWH which lies near Hijiori volcano in central Tohoku and station KWSH which lies near a Pliocene-Quaternary caldera 20 km to the NE of Zao volcano (Figure 3.1). These stations were selected because their negative Ps phases at 8-10 km depth are examples of larger (NKWH) and smaller (KWSH) amplitudes, and because comparisons of SV and SH receiver functions at each station demonstrate that the negative Ps phases can be interpreted as relatively flat isotropic velocity decreases (Figures. 3.8 and 3.9).

At station NKWH, the negative (SV) Ps phases at approximately 10 km depth (Figures. 3.3a and 3.8) suggest that the station is underlain by an upper-crustal melt-rich layer that is wide enough to be sampled by phases coming from at least the southeast to the west (Figures. 3.3a and 3.8; groups of green circles near Hijori in Figure 3.12). Positive Ps phases occur at depths of approximately 20 km.

The velocity structure beneath station NKWH was modeled by comparing synthetic receiver functions for trial velocity structures to the observed Ps receiver function that combines data from back-azimuths of 130°-255° (black line in right panel of Figure 3.17). Synthetic receiver functions were calculated with the propagator matrix method (Keith and Crampin, 1977). In the real data, the dominant period of the direct P wave was 3-5 s, and the source-time function used for the synthetics had a 4 s period. Synthetics were calculated for the ray parameter range represented in the real data (0.048-0.078 s/km), and the synthetic receiver functions were calculated using the same process that was applied to the real data. Because Ps phases can only constrain velocity gradients and discontinuities, we used the migration model as an initial structure and iteratively perturbed model parameters until the predicted receiver functions fit the observed stack within its uncertainties.
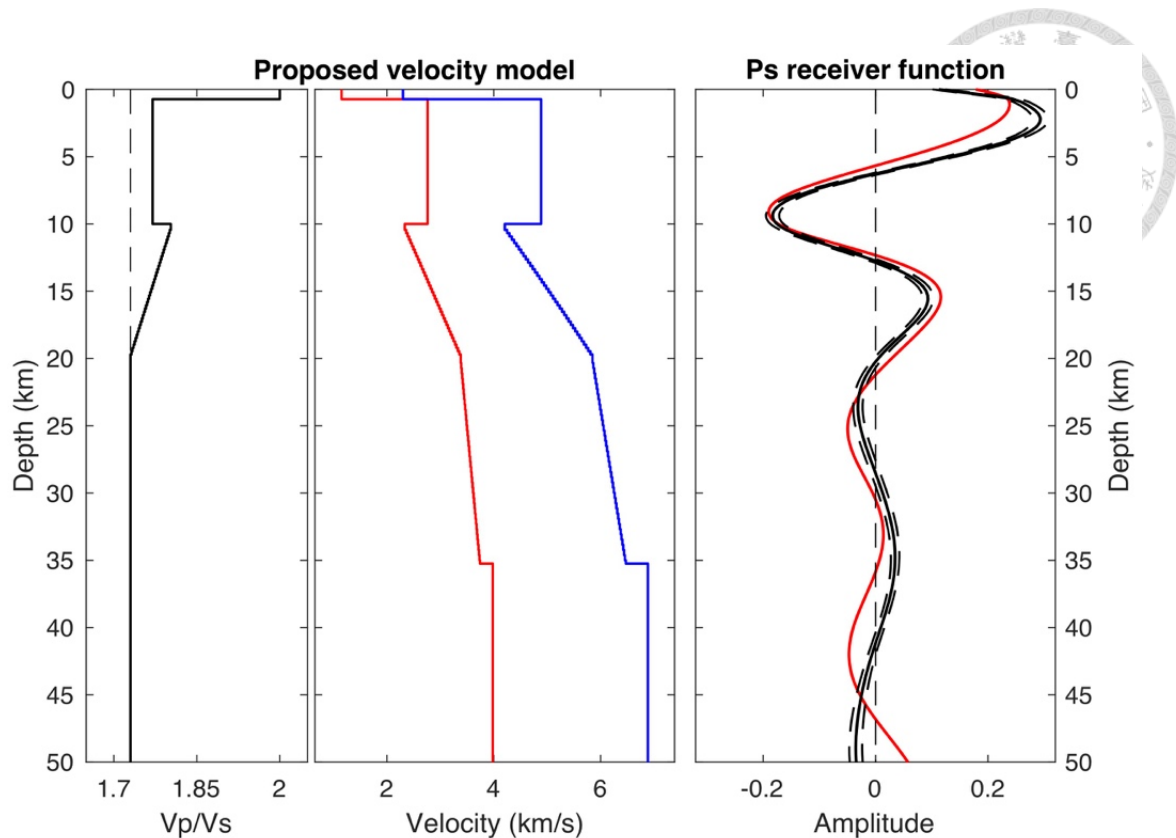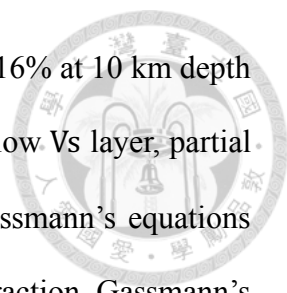
Figure 3.18 Modeling of Ps stacks for station NKWH. The best-fitting velocity structure (left panel: Vp/Vs ratio; middle panel: Vp (blue) and Vs (red)) beneath station NKWH. The model contains a thin sediment layer that is 0.7 km thick, a velocity decrease of 16% at 10 km depth followed by an increase in velocity to 3.38 km/s at 20 km depth. Right panel: Ps receiver function stack that combines data within the 130°-255° back-azimuth range (black line, with two standard deviation uncertainties shown by dashed lines) and synthetic receiver functions predicted for ray parameters of 0.048-0.078 s/km at 0.01 increments (red lines). Only the first three phases in the NKWH receiver function were modeled because reverberations overprint later arrivals.

The observed (black) and predicted (red) receiver functions for the proposed velocity model show acceptable agreement in the 0-30 km depth range (Figure 3.17). In the proposed velocity model that yields the predicted stack, three features are necessary: a

87

thin sediment layer that is 0.7 km thick, a shear velocity decrease of 16% at 10 km depth followed by a gradual velocity gradient to a depth of 20 km. In this low Vs layer, partial melt fraction was estimated from observed Vs reductions using Gassmann's equations (Gassmann, 1951), as described in section 4.3. Assuming this melt fraction, Gassmann's equations were used to predict Vp/Vs for the layer. Note that real Ps phase depths in Figure 3.17 differ from those in Figure 3.3a because in Figure 3.17 the data is migrated with the final velocity model obtained from the modeling (left and center panels in Figure 3.17). Trade-offs exist between model parameters, and we perturbed both the depth of the top of the low velocity and the velocity drop at this boundary to estimate how much these parameters could vary while still providing acceptable fits to the observed receiver functions. Uncertainty in the depth of the top of the low velocity layer is less than 0.7 km, and the velocity drop at this boundary can vary by no more than 5%.

We also tested whether a less vertically localized upper boundary to the low velocity layer is possible. A velocity decrease over 2 km in depth can adequately fit the negative Ps phase at NKWH, but the match of the synthetics to the positive phase at 15 km depth is reduced (Figure 3.18a), even when the positive velocity gradient deeper in the low velocity layer is adjusted (Figure 3.18b). A velocity decrease over 10 km increases misfit by reducing the depth of the negative Ps phase (Figure 3.18c).
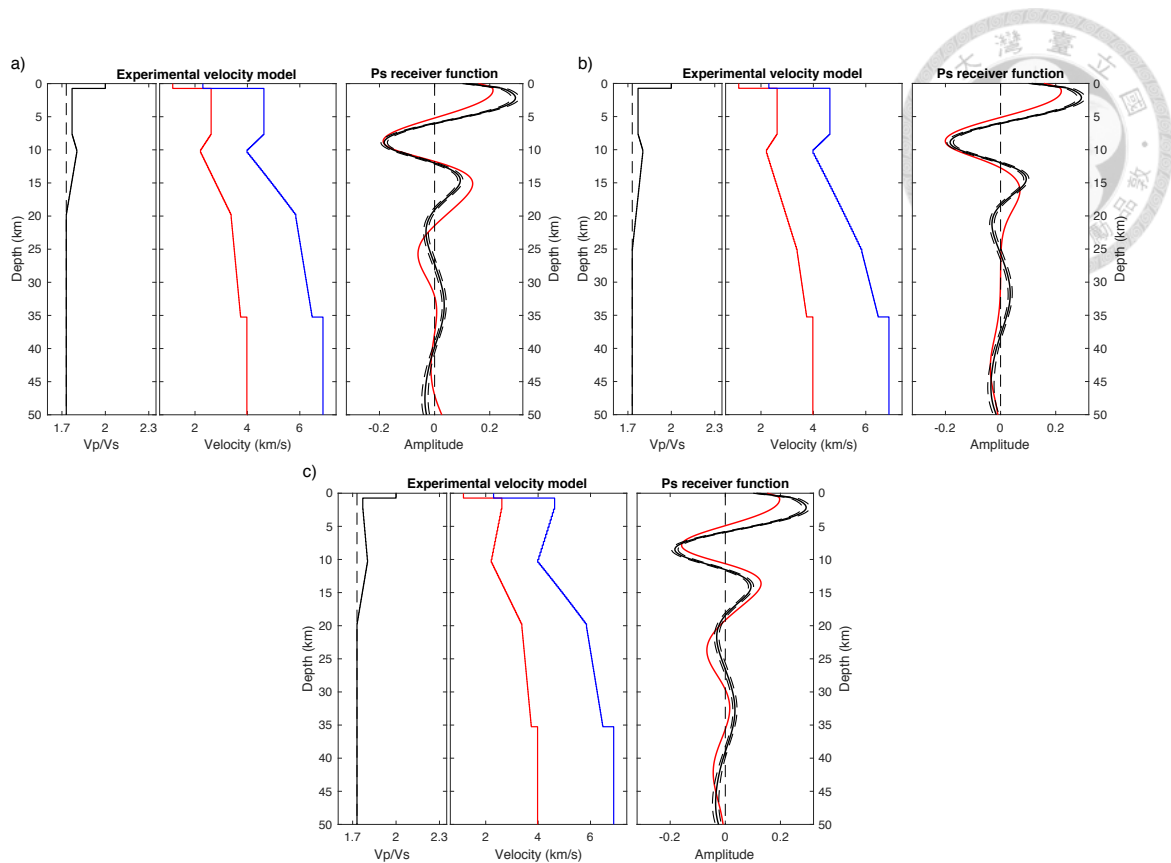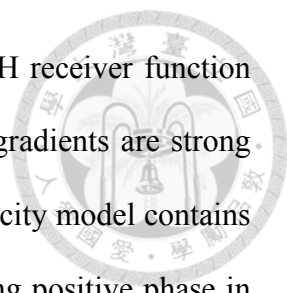
Figure 3.19 Tests with less vertically localized upper boundaries to the low velocity layer below station NKWH. Velocity structure (left panel: Vp/Vs ratio; middle panel: Vp (blue) and Vs (red)). Right panel: Ps receiver function stack that combines data within 130°-255° back-azimuth range (black line, with two standard deviation uncertainties shown by dashed lines) and synthetic receiver functions predicted for ray parameters of 0.048-0.078 s/km at 0.01 increments (red lines). (a) A velocity decrease over 2 km in depth at the upper boundary of the low velocity layer can adequately fit the negative Ps phase at NKWH, but the match of the synthetics to the positive phase at 15 km depth is reduced. (b) The same as (a) except that the positive velocity gradient deeper in the low velocity layer is distributed over a greater depth range. (c) A velocity decrease over 10 km at the upper boundary of the low velocity layer. None of these models predict receiver functions that fit the data as well as the model shown in Figure 3.17.

In practice we modeled only the first three phases in the NKWH receiver function because the reverberations from these velocity discontinuities and gradients are strong and overprint later arrivals. For example, although the proposed velocity model contains a velocity increase at a trial Moho at 36 km depth, the corresponding positive phase in the synthetic receiver function stack is obscured by interference with reverberations from shallower structure.

Similar waveform modeling was also carried out for station KWSH whose shallow negative Ps arrival lies at the lower amplitude end of well-constrained examples of this phase (Figures. 3.3c and 3.9). At station KWSH, a velocity drop of 7% ± 3% at 8.5 km was obtained (Figure 3.19). Station YUZH (Figures. 3.4b and 3.10) which lies near a Pliocene-Quaternary caldera, has a shallow negative Ps phase that is similar to the case at NKWH, suggesting a comparable velocity drop near the same depth (10 km).

90
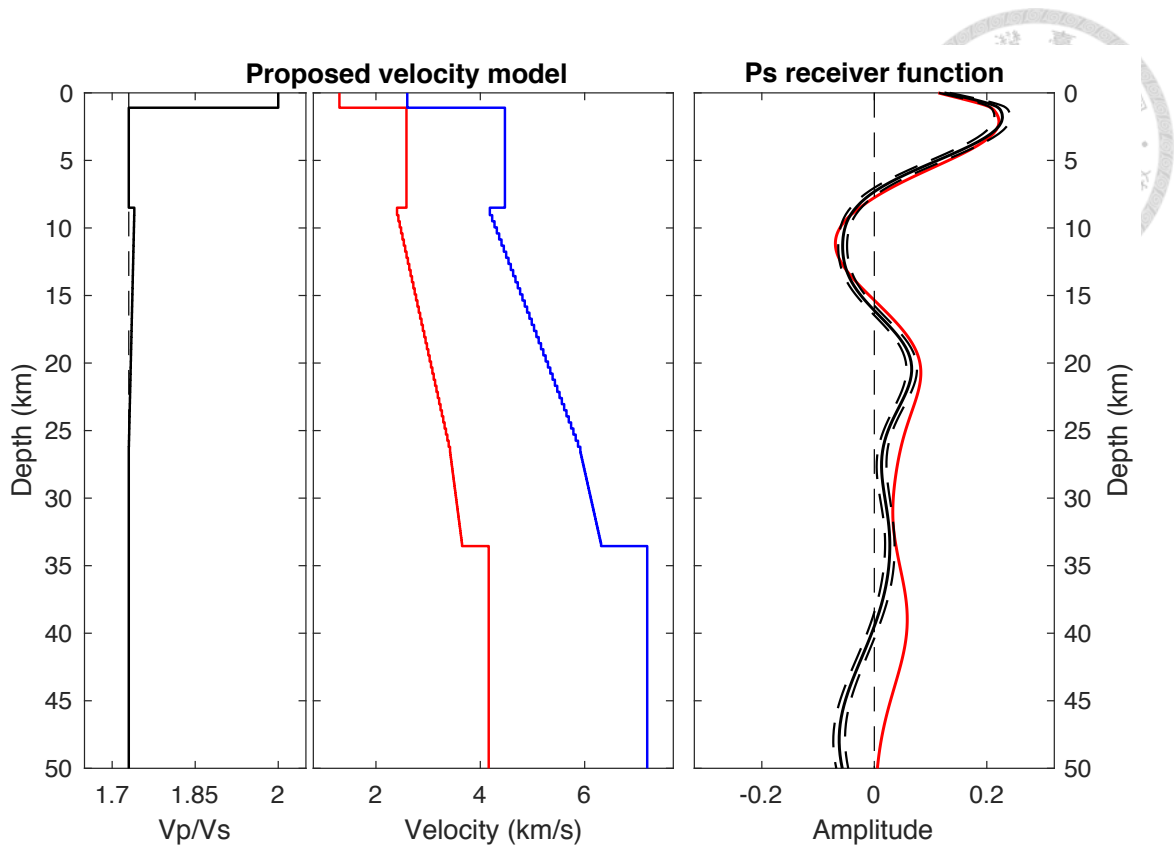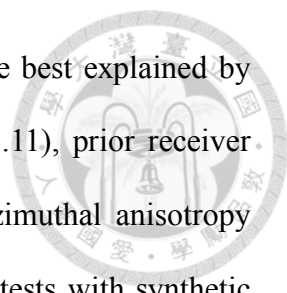
Figure 3.20 Modeling of Ps stacks for station KWSH. The best-fitting velocity structure (left panel: Vp/Vs ratio; middle panel: Vp (blue) and Vs (red)) beneath station KWSH. The model contains a thin sediment layer that is 1.3 km thick, a velocity decrease of 7% at 8.5 km depth followed by an increase in velocity to 3.42 km/s at 26 km depth. Right panel: Ps receiver function stack that combines data within 130°-255° back-azimuth range (black line, with two standard deviation uncertainties shown by dashed lines) and synthetic receiver functions predicted for ray parameters of 0.048-0.078 s/km at 0.01 increments (red lines). Only the first three phases in the KWSH receiver function were modeled because reverberations overprint later arrivals. The velocity drop at the top of the low velocity layer is among the smaller values observed for stations in Tohoku with clear negative Ps phases in the shallow crust.

91

Although Ps receiver functions at numerous Tohoku stations are best explained by isotropic structure in the 5-15 km depth range (e.g. Figures. 3.8-3.11), prior receiver function modeling (Bianchi et al., 2015) detected evidence for azimuthal anisotropy beneath some Tohoku stations. We therefore conducted a series of tests with synthetic seismograms to assess potential effects of anisotropy. The ambient noise tomography of Chen et al. (2018) indicated the presence of azimuthal anisotropy with amplitudes of up to 2.5%. This magnitude of anisotropy is comparable to, or exceeds, the majority of the best-constrained azimuthal anisotropy values estimated from Ps receiver functions by Bianchi et al. (2015). We first tested whether the vertical variations in azimuthal anisotropy and isotropic Vs from the Chen et al. (2018) model at NKWH could produce the crustal phases observed at this station. In the synthetic receiver functions for this model, phase amplitudes are small compared to the amplitudes of the observed Ps phases (Figure 3.20), indicating that the azimuthal anisotropy is insufficient to explain the data and a large isotropic velocity decrease at 10 km depth is indeed required. Second, we added the Chen et al. (2018) azimuthal anisotropy to the proposed velocity model for NKWH, and the resulting predicted receiver functions still adequately fit the observed Ps stack, indicating that azimuthal anisotropy of this magnitude would not significantly affect the results of the isotropic Vs modeling. Third, we tested the effects of allowing the fast symmetry axes of anisotropy to plunge at 45° (Figure 3.21b), relative to horizontal symmetry axes (Figure 3.21a), with no vertical variations in isotropic structure in these cases. Although the case with plunging symmetry axes produces larger Ps amplitudes, the synthetic amplitudes are still much weaker than the observed Ps phases.
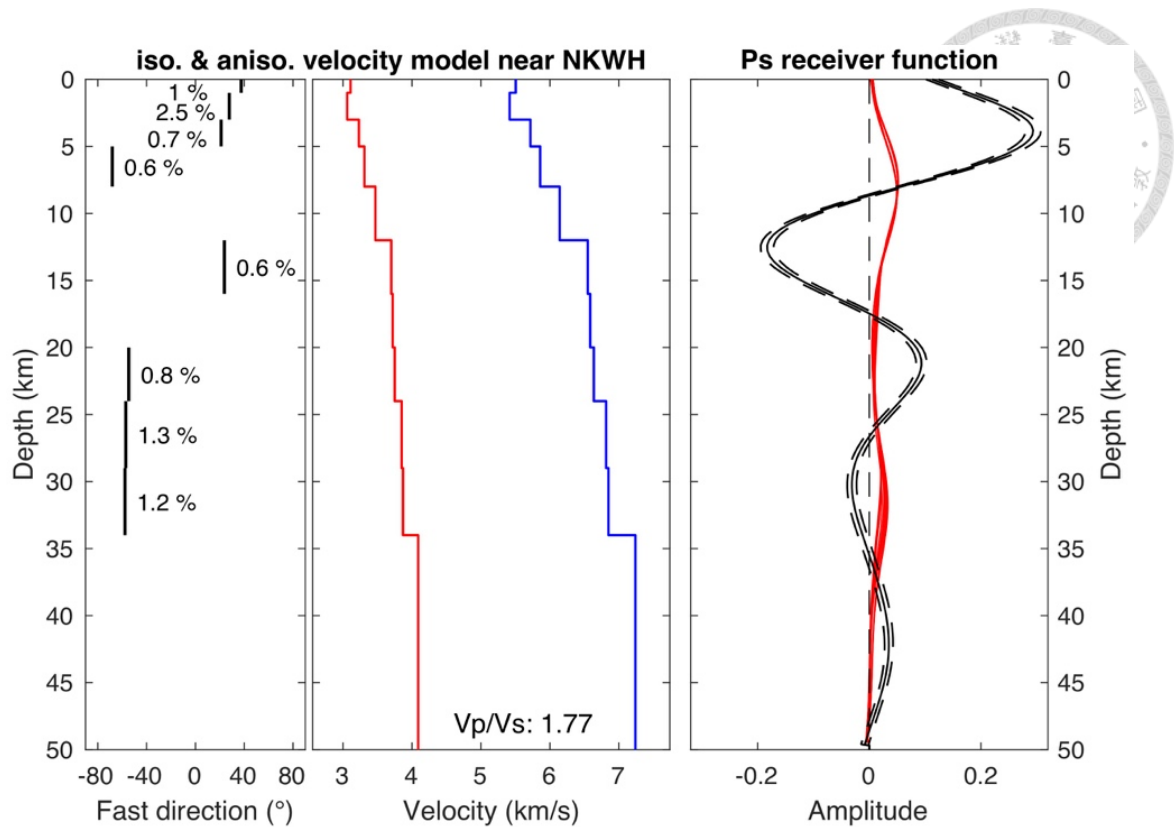
Figure 3.21 Test of anisotropic structures. Left panel: Fast directions of azimuthal anisotropy in different depth ranges from the Chen et al. (2018) model at NKWH; strengths of anisotropy are labeled. Weaker anisotropy in other depth ranges was ignored. Middle panel: Isotropic Vs (red) at NKWH from Chen et al. (2018), with Vp (blue) assuming Vp/Vs is fixed to 1.77. Right panel: Ps receiver function stack that combines data within 130°-255° back-azimuth range (black line, with two standard deviation uncertainties shown by dashed lines) and synthetic receiver functions predicted for the model in left and middle panels for ray parameters of 0.048-0.078 s/km at 0.01 increments (red lines). The amplitudes of the predicted phases are small and do not match the observed Ps stack at NKWH.
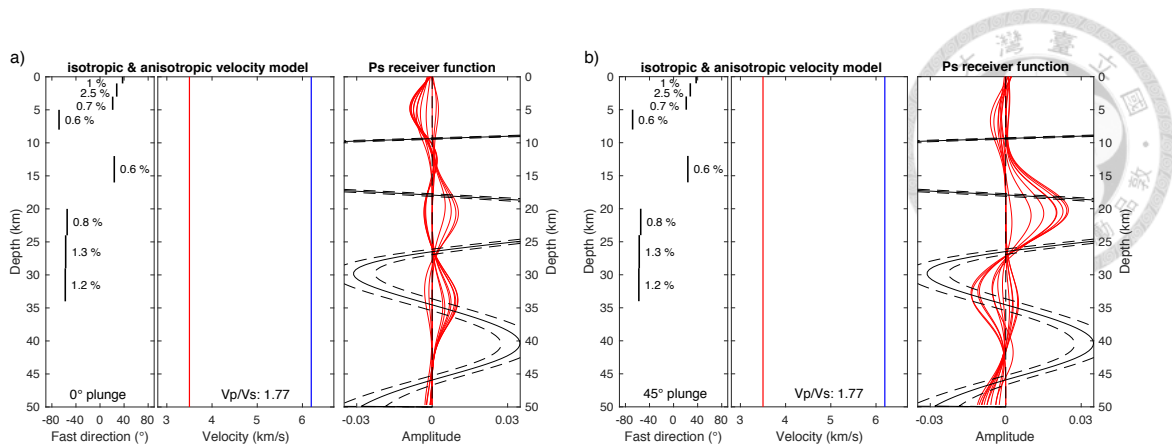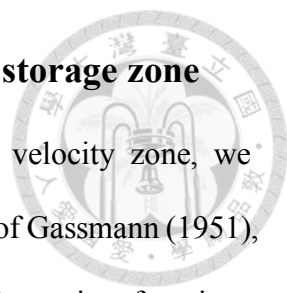
Figure 3.22 Tests of anisotropic structure with (a) horizontal and (b) 45° plunging fast symmetry axes. Left panel: Fast directions of azimuthal anisotropy in three different depth ranges from the Chen et al. (2018) model at NKWH; strengths of anisotropy are labeled. Weaker anisotropy in other depth ranges ignored. Middle panel: a 3.5 km/s Vs (red) assuming Vp/Vs is fixed to 1.77. Right panel: Ps receiver function stack that combines data within 130°-255° back-azimuth range (black line, with two standard deviation uncertainties shown by dashed lines) and synthetic receiver functions predicted for the model in left and middle panels for ray parameters of 0.048-0.078 s/km at 0.01 increments (red lines) within the same back-azimuth range. (b) Same as (a), except with 45° plunging fast symmetry axes. Although the case with a plunging symmetry axes produces larger Ps amplitudes, the synthetic amplitudes (< 0.03) are still much weaker than the observed Ps phases (> 0.2).

The key result of the waveform modeling at stations NKWH and KWSH is the presence of a low velocity layer with a vertically sharp upper boundary, a minimum Vs at 8-10 km depth, and a more gradual positive velocity gradient at greater depths. This structure is consistent with a melt storage layer in the crust where the highest melt fractions are at its top at a depth of 8-10 km, and the ratio of melt to crystals increases with depth (e.g. Bachman and Huber, 2016; Cashman et al., 2017). Given that negative

94

Ps phases at depths of 5-10 km are widespread in the magmatically active regions of Tohoku, a low velocity layer with its top at comparable depths is expected to be common, although not ubiquitous. As shown by the differences in the velocity models obtained for these two stations, because the amplitude of this negative phase is variable, the velocity reduction within this layer also varies.

This velocity structure is similar to a low velocity layer at depths of 11-20 km beneath Iwate volcano in northern Tohoku imaged with receiver function inversion (Nakamichi et al., 2002) and with the top of a low velocity layer inferred beneath other Tohoku volcanoes (Igarashi et al., 2011). The structure is also comparable in depth to the results of receiver function studies in other subduction zones. Bannister et al. (2004) inverted Ps receiver functions and found a similar low velocity layer beneath the Taupo Volcanic zone in the New Zealand North Island subduction zone; there the top of the low velocity layer lies at depths of 7-11 km. Ward et al. (2014) jointly inverted receiver functions and surface wave phase velocities beneath the Altiplano-Puna volcanic complex in the South American subduction zone and found a low velocity layer with a sharp top at 6-11 km that extended to depths of 20-25 km. Receiver function studies beneath Akutan volcano in the Aleutian arc (Janiszewski et al., 2013) and beneath Mt. Vesuvius in the Campanian arc (Agostinetti and Chiarabba, 2008) also found low velocity layers with upper boundaries at 7-9 km and ~6 km depth, respectively. However, these low-velocity layers were inferred to be only a few kilometers thick, as opposed to the more gradual positive velocity gradients inferred in this study and in Nakamichi et al. (2002), Bannister et al. (2004), and Ward et al. (2014).
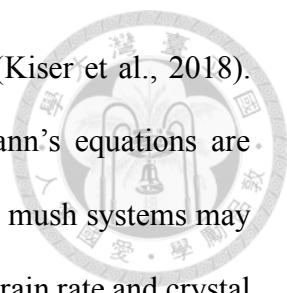
3.4.2 Bounds on melt-fraction in the shallow magma storage zone

To estimate possible melt fraction in the shallow crustal low velocity zone, we calculated Vs reduction as a function of melt fraction using the theory of Gassmann (1951), and compared these values to the Vs models obtained from modeling Ps receiver functions. We related Vs reduction (as opposed to absolute Vs) to melt porosity, thus reducing the dependence on melt composition, temperature and pressure (e.g. Yu and Lee, 2016), and because Vs is the velocity that is directly constrained by the receiver function modeling. We employed a silica-rich composition, temperature (780 ° C) and pressure (82 ± 60 MPa) appropriate for crustal melts beneath Hijiori volcano (Miyagi et al., 2017), where station NKWH is located, but because we compare velocity reduction to melt fraction, parameters for other Tohoku volcanoes would yield a very

similar scaling relationship. Elastic moduli and densities for crystals and melt at standard temperature and pressure were taken from Bass (1995) and Levy et al. (2000). We adopted a critical melt porosity (Nur et al., 1998) of 35%, based on studies that estimate this parameter at 30-35% (Van der Molen and Paterson, 1979; Yu and Lee, 2016).

Comparison of Vs reduction due to melt porosity predicted by the Gassmann's equations to the $16\% \pm 5\%$ Vs decrease at the top of the low velocity layer in the NKWH velocity model yields a maximum melt fraction of $10\% \pm 3\%$. The increase in velocity at greater depth in the low velocity layer could represent a decreasing melt fraction, reaching a value of ~3% at 20 km. A similar comparison to the $7\% \pm 3\%$ velocity decrease at the upper boundary of the low velocity layer at station KWSH implies a maximum melt fraction of $5\% \pm 2\%$. These maximum melt fractions are less than the value estimated beneath the Yellowstone magmatic system based on receiver functions (32%) (Chu et al., 2010), and the intermediate melt fraction at NKWH is comparable to the value inferred

96

beneath Mt. St. Helens based on active source tomography (12%) (Kiser et al., 2018). However, while these comparisons between regions using Gassmann's equations are useful, an important caveat is that the rheological behavior of crystal mush systems may be more complex, including dependence of critical melt fraction on strain rate and crystal shapes, sizes and orientations (e.g. Costa et al., 2009). The 3% partial melt estimated for depths near 20 km beneath Hijiori volcano falls within the range of partial melt fractions inferred by Nishimoto et al. (2008) for the lower crust beneath the Tohoku arc at more northern latitudes (39° -40°).

3.4.3 Implications for polybaric crustal melt storage

The Ps phases observed in this study, combined with the Chen et al. (2018) Vs model, are consistent with polybaric melt storage in a trans-crustal mush zone (e.g. Bachman and Huber, 2016; Cashman et al., 2017; Jackson et al., 2018). First, the laterally widespread, vertically localized velocity decrease implied by the negative Ps phases at depths of 5-10 km in volcanic regions of Tohoku, which lies near the top of low velocity anomalies in the Chen et al. (2018), is consistent with the concentration of higher melt fractions near top of the mush zone. Observed variations in negative Ps phase amplitudes suggest that melt fraction, along with other properties such as volatile content and temperature, are laterally variable. Second, increasing velocities below this depth, as seen in the shear velocity models for stations NKWH (Figure 3.17) and KWSH (Figure 3.19) and from Chen et al. (2018) (Figure 3.15), and as implied by the presence of positive Ps phases at depths of 15-30 km at other stations, are consistent with an overall decrease in melt fraction in the deeper crust. Third, some localized bands of negative Ps arrivals (Figure 3.15) hint at local maxima in melt fraction at depths of 10-30 km. The spatial distribution of these deeper Ps arrivals does not resolve the issue of whether the mush column contains

melt-rich lenses distributed throughout the middle and lower crust (Cashman et al., 2017; Sparks et al., 2019) or at two to three depths where most melt fractionation takes place (Bachman and Huber, 2016). In some cases, the deeper zones of negative Ps phase do not occur directly beneath volcanic centers.

The 5-10 km depths of the widespread negative Ps phases and the largest low velocity anomalies in the Chen et al. (2018) tomography agree strikingly well with the predictions of the Huber et al. (2019) thermo-mechanical modeling. In these models, magma chambers with enough melt to be potentially eruptible will grow and persist over time only at depths of 5-10 km. At depths greater than ~10 km, where crustal viscosities are higher, large non-eruptible zones of melt storage develop, providing a source of melt that can re-charge the shallower eruptible zones. At depths less than ~5 km, lower pressures enhance volatile exsolution, and eruptions efficiently remove magma at a rate faster than it can be re-supplied, leading to magma chambers that are small and short-lived. Low velocities induced by persistent zones with eruptible fractions of melt thus are predicted in the 5-10 km depth range, consistent with the widespread, large negative Ps phases and low shear velocities at these depths. Taken at face value, the 10% ± 3% melt fraction obtained with the Gassmann's equations for the top of the low velocity layer beneath station NKWH (section 4.2) does not reach the eruptible range of 40-50% (Huber and Backman, 2016; Cashman et al., 2017). However, given uncertainties in the assumptions made in this calculation, higher melt fractions cannot be ruled out. In any case, the widespread distribution of negative Ps phases in the 5-10 km depth range near volcanic centers in Tohoku suggests that melt storage in this depth range is not temporally ephemeral.

A further implication for shallow crustal melt storage is that the low velocity, higher melt fraction zones whose upper boundaries lie at 5-10 km depth are not solely localized

98

beneath individual volcanoes (Figure 3.12). Counting only negative Ps phases at 5-10 km depth with absolute amplitudes of more than 0.1, the mean distance between phase conversion points and the nearest Holocene volcano is 26 ± 13 km. In some cases, clusters of large amplitude negative Ps conversions sample an area that encompasses several volcanoes and young (Pliocene-Quaternary) calderas, suggesting that adjacent magmatic centers share the same upper crustal melt storage zone. This possibility is supported by the observation that magmatic centers associated with the same potential crustal reservoir (as defined by clusters of negative Ps phases) have similar Nd-Sr ratios (Yoshida et al., 2014) while in some cases different clusters (i.e., potential crustal reservoirs) have contrasting Nd-Sr ratios (Figure 3.22).
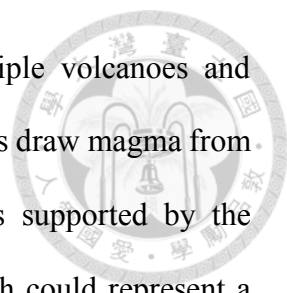

99
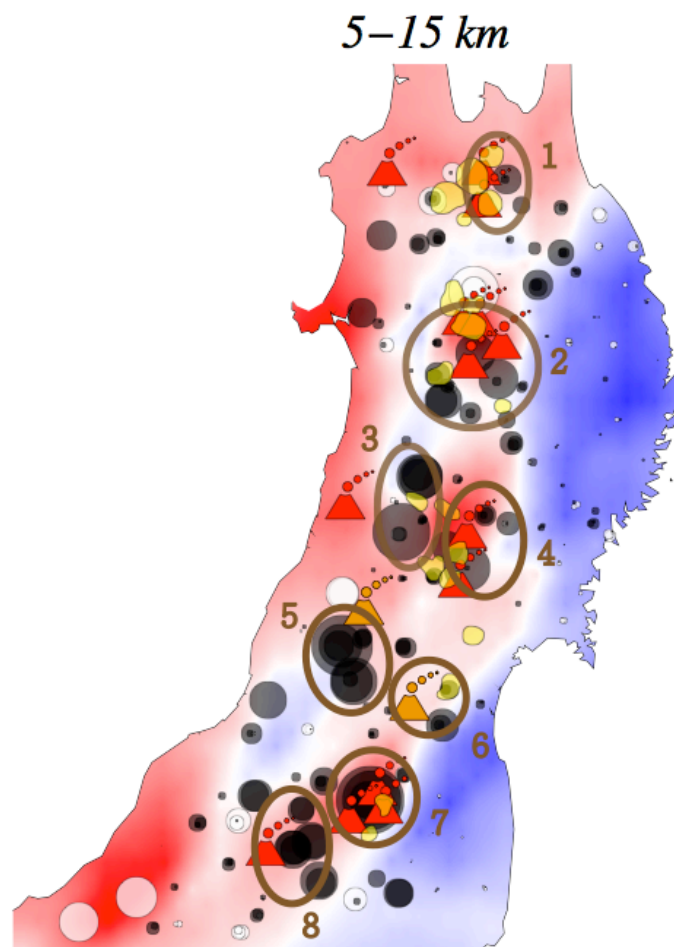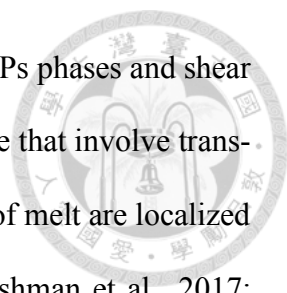
Figure 3.23 Clusters of negative Ps phases that surround multiple volcanoes and calderas (e.g. brown circles) suggest that these volcanoes and calderas draw magma from the same melt-rich zone in the shallow crust. This possibility is supported by the observation that within a given cluster of negative Ps phases, which could represent a single potential crustal reservoir, magmatic centers have similar Nd-Sr ratios (Yoshida et al., 2014). In some cases different Ps phase clusters (potentially different crustal reservoirs) have contrasting Nd-Sr ratios.

Some volcanoes are significantly laterally offset from the nearest conversion points corresponding to large amplitude Ps phases. Some of these examples may reflect an absence of a nearby seismic station with sufficient high quality receiver functions, but others suggest that the roofs of melt-rich bodies may not lie directly beneath the volcanoes that they supply. These latter cases are reminiscent of the apparent reservoir beneath Mount St. Helens that is laterally offset from the volcano by 2-10 km at depths of 4-10 km in Vp and Vp/Vs tomography (Kiser et al., 2016; 2018). Finally, some conversion points with large negative Ps phases are located well away from a Holocene volcano or young caldera, raising the possibility of a melt-rich zone that has not produced a recent eruption

3.5 Conclusions

Ps receiver functions from seismic stations in the Tohoku region of Japan show a pronounced variation in crustal discontinuity structure between central and western regions that contain low shear velocity anomalies (Chen et al., 2018) and Holocene volcanoes versus northeastern and southeastern regions containing the Cretaceous Kitakami and Abukuma mountains where crustal velocities are higher.

In central and western Tohoku, velocity gradients inferred from Ps phases and shear velocity anomalies are consistent with models for crustal melt storage that involve trans-crustal zones of crystal-melt mush where the highest concentrations of melt are localized at the top of the mush column (e.g Bachman and Huber, 2016; Cashman et al., 2017; Jackson et al., 2018). Negative Ps phases are widespread in volcanic regions at depths of 5-10 km and they correlate with the upper boundaries of low shear velocity zones from tomography. These features are consistent with the roofs of high melt fraction layers, and their depths match the pressures where thermo-mechanical modeling predicts that high melt fraction magma chambers should persist over time (Huber et al., 2019).
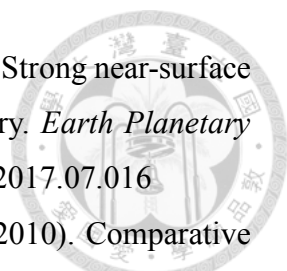
Deeper (10-30 km) positive phases likely represent more gradual velocity positive gradients that correspond to decreasing melt fraction with depth. For example, waveform modeling of Ps receiver functions at station NKWH near Hijiori volcano in central Tohoku indicates a $16\% \pm 5\%$ Vs drop at 10 km depth above a velocity increase to 20 km, corresponding to a maximum melt fraction of $10\% \pm 3\%$ that decreases to 3%. The velocity reduction modeled at station KWSH ($7\% \pm 3\%$) implies a maximum melt fractions of $5\% \pm 2\%$, indicating significant variation in stored crustal melt across Tohoku. Some localized groups of deeper negative Ps phases at depths of 10-20 km indicate negative velocity gradients that may reflect local maxima in melt fraction at greater depths and larger distances from volcanic centers.
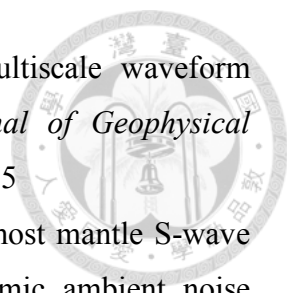
The zones of higher melt fraction at 5-10 km in some cases encompass more than one volcano, suggesting that the same upper crustal source can supply multiple volcanoes. In other cases, high melt fraction zones are significantly laterally offset from the nearest volcano. Together with the deeper zones of potentially higher melt fraction, these results indicate that crustal melt storage may occur at distances of 40-50 km from a volcanic center.

REFERENCES

Ando, M. (1979). The stress field of the Japan islands in the last 0.5 million years (in Japanese). *The Earthquake Monthly Symposium, 7,* 541–546.

Abt, D. L., Fischer, K. M., French, S. W., Ford, H. A., Yuan, H., & Romanowicz, B. (2010). North American lithospheric discontinuity structure imaged by Ps and Sp receiver functions. *Journal of Geophysical Research, 115,* B09301. https://doi.org/10.1029/2009JB006914

Agostinetti, N. P., Chiarabba, C. (2008). Seismic structure beneath Mt Vesuvius from receiver function analysis and local earthquakes tomography: evidences for location and geometry of the magma chamber. *Geophysical Journal International, 175* (3), 1298–1308. http://dx.doi.org/10.1111/j.1365-246X.2008.03868.x.

Arpa, M. C., Zellmer, G. F., Christensou, B., Lube, G., & Shellnutt, G. (2017). Variable magma reservoir depths for Tongariro volcanic complex eruptive deposits from 10,1000 years to present. *Bulletin of Volcanology, 79,* 56. https://doi.org/10.1007/s00445-017-1137-5

Audoine, E., Savage, K., & Gledhill, K. (2004). Anisotropic structure under a back arc spreading region, the Taupo Volcanic Zone, New Zealand. *Journal of Geophysical Research, 109*, B11305. https://doi.org/10.1029/2003JB002932

Bachmann, O., Bergantz, G. W. (2004). On the origin of crystal-poor rhyolites: extracted from batholithic crystal mushes. *Journal of Petrology, 45,* 1565–1582. https://doi.org/10.1093/petrology/egh019.

Bachmann, O., Huber, C. (2016). Silicic magma reservoirs in the Earth's crust. *American Mineralogist, 101*, 2377–2404. https://doi.org/10.2138/am-2016-5675.

Bannister, S., Bryan, C. J., Bibby, H. M. (2004). Shear wave velocity variation across the Taupo Volcanic Zone, New Zealand, from receiver function inversion. *Geophysical Journal International, 159*, 291–310. https://doi: 10.1111/j.1365-246X.2004.02384.x

Ban, M., Sagawa, H., Miura, K., & Hirotani, S. (2008). Evidence for short-lived stratified magma chamber: petrology of Z-To5 tephra layer (c. 5.8 ka) at Zao volcano, NE Japan. In C. Annen, G.F. Zellmer (Eds.), *Dynamics of Crustal Magma Transfer, Storage and Differentiation* (Vol. 304, pp. 149–168). London, Special Publications. https://doi.org/10.1144/SP304.8

Bass, J. D. (1995). Elasticity of Minerals, Glasses, and Melts. Mineral Physics and Crystallography: *A Handbook of Physical Constants, vol. 2*, pp. 45–63. https://doi.org/10.1029/RF002p0045.

Bensen, G. D., Ritzwoller, M. H., Barmin, M. P., LeVshin, A. L., Lin, F. C., Moschetti, M. P., Shapiro, N. M., & Yang, Y. (2007). Processing seismic ambient noise data to obtain reliable broad-band surface wave dispersion measurements. *Geophysical Journal International*, *169*, 1239–1260. https://doi.org/10.1111/j.1365-246X.2007.03374.x

Bianchi, I., Bokelmann, G., Shiomi, K. (2015). Crustal anisotropy across northern Japan from receiver functions. *Journal of Geophysical Research, Solid Earth, 120*, 4998–5012. https://doi.org/10.1002/2014JB011681.

Cashman, K., Sparks, R., Blundy, J. (2017). Vertically extensive and unstable magmatic systems: a unified view of igneous processes. *Science, 355.* https://doi.org/10.1126/science.aag3055. https://doi.org/10. 1126/science.aag3055.

Chen, K. X., Chen, P. F., Chen, L. W., Yao, H., Fang, H., & Su, P. (2016b). South Ilan plain High-Resolution 3-D S-Wave Velocity from Ambient Noise Tomography. *Terrestrial, Atmospheric and Oceanic sciences journal, 27,* 375–385. https://doi.org/10.3319/TAO.2016.01.29.02(TEM)

Chen, K.-X., Fischer, K.M., Hua, J., Gung, Y. (2020). Imaging crustal melt beneath northeast Japan with Ps receiver functions. *Earth and Planetary Science Letters*, *537,* 2020. https://doi.org/10.1016/j.epsl.2020.116173.

Chen, K. X., Gung, Y., Kuo, B. Y., Huang, T. Y. (2018). Crustal magmatism and deformation fabrics in northeast Japan revealed by ambient noise tomography. *Journal of Geophysical Research, Solid Earth, 123,* 8891–8906. https://doi.org/10.1029/ 2017JB015209

Chen, K. X., Kuo-Chen, H., Brown, D., Li, Q., Ye, Z., Liang, W. T., Wang, C. Y., & Yao, H. (2016a). Three-dimensional ambient noise tomography across the Taiwan Strait: The structure of a magma-poor rifted margin. *Tectonics, 35*, 8, 1782–1792. https://doi.org/10.1002/2015TC004097

Chen, L., Wen, L., Zheng, T. (2005). A wave equation migration method for receiver function imaging: 2. Application to the Japan subduction zone. *Journal of Geophysical Research, Solid Earth, 110,* B11310. http://doi.org/10.1029/2005JB003666.
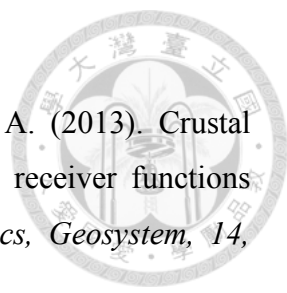
Chen, L. W., Chen, Y. N., Gung, Y., Lee, J. C., & Liang, W. T. (2017). Strong near-surface seismic anisotropy of Taiwan revealed by coda interferometry. *Earth Planetary Science Letters, 475*, 224–230. https://doi.org/10.1016/j.epsl.2017.07.016

Chiao, L. Y., Fang, H. Y., Gung, Y., Chang, Y. S., & Hung, S. H. (2010). Comparative appraisal of linear inverse models constructed via distinctive parameterizations. *Journal of Geophysical Research, 115*, B07305. https://doi.org/10.1029/2009JB006867

Chiao, L. Y., & Kuo, B. Y. (2001). Multiscale seismic tomography. *Geophysical Journal International, 145*, 517–527. https://doi.org/10.1046/j.0956-540x.2001.01403.x

Chiao, L. Y., Lin, J. R., & Gung, Y. (2006). Crustal magnetization equivalent source model of Mars constructed from a hierarchical multiresolution inversion of the MGS data. *Journal of Geophysical Research, 111*, E12010. https://doi.org.10.1029/2006JE002725

Chu, R. S., Helmberger, D. V., Sun, D. Y., Jackson, J. M., Zhu, L. P. (2010). Mushy magma beneath Yellowstone. *Geophysical Research Letters, 37*. http://dx.doi.org/10.1029/ 2009GL041656.

Crampin, S., & McGonigle, R. (1981). The variation of delays in stress-induced anisotropic polarization anomalies. *Geophysical Journal International, 64*, 115–131. https://doi.org/10.1111/j.1365-246X.1981.tb02661.x

Costa, A., Caricchi, L., Bagdassarov, N. (2009). A model for the rheology of particle-bearing suspensions and partially molten rocks. *Geochemistry, Geophysics, Geosystems, 10*, Q03010. https://doi.org/10.1029/2008GC002138.

DeMets, C., Gordon, R. G., & Argus, D. F. (2010). Geologically currentplate motions. *Geophysical Journal International, 181*(1), 1–80. https://doi.org/10.1111/j.1365-246X.2009.04491.x

Finn, C. (1994). Aeromagnetic evidence for a buried Early Cretaceous magmatic arc, northeast Japan. *Journal of Geophysical Research, 99*, 22,165–22,185. https://doi.org/10.1029/94JB00855

Fitch, T. J. (1972). Plate convergence, transcurrent faults, and internal deformation adjacent to Southeast Asia and the western Pacific. *Journal of Geophysical Research, 77*(23), 4432–4460. https://doi.org/10.1029/JB077i023p04432

Gassmann, F., 1951. Über die Elastizität poröser Medien. *Vierteljahrsschr. Naturforsch. Ges. Zürich, 96*, 1–23.

Gung, Y., Hsu, Y., Chiao, L. Y., & Obayashi, M. (2009). Multiscale waveform tomography with two-step model parameterization. *Journal of Geophysical Research, 114*, B11301. https://doi.org/10.1029/2008JB006275

Guo, Z., Guo, X., Shi, H., & Wang, W. (2013). Crustal and uppermost mantle S-wave velocity structure beneath the Japanese islands from seismic ambient noise tomography. *Geophysical Journal International, 193,* 394–406. https://doi.org/10.1093/gji/ggs121

Hasegawa, A., Horiuchi, S., Umino, N. (1994). Seismic structure of the northeastern Japan convergent margin: a synthesis. *Journal of Geophysical Research, Solid Earth, 99,* 22295–22311. https:// doi.org/10.1029/93JB02797.

Hasegawa, A., & Nakajima, J. (2004). Geophysical constraints on slab subduction and arc magmatism. In R. S. J. Sparks, C. J. Hawkesworth (Eds.), *The State of the Planet: Frontiers and Challenges in Geophysics* (Vol. 150, pp. 81–94). American Geophysical Union, Washington, D. C.

Hasegawa, A., Umino, N., & Takagi, A. (1978). Double-planed structure of the deep seismic zone in the northeastern Japan arc. *Tectonophysics, 47*, 43–58. https://doi.org/10.1016/0040-1951(78)90150-6

Hildreth, W. (2004). Volcanological perspectives on Long Valley, Mammoth Mountain, and Mono Craters: several contiguous but discrete systems. *Journal of Volcanology and Geothermal Research, 136,* 169–198. https://doi.org/10.1016/j.jvolgeores.2004.05.019.

Holt, A. F., Becker, T. W., & Buffett, B. A. (2015). Trench migration and overriding plate stress in dynamic subduction models. *Geophysical Journal International, 201*, 172-192. https://doi.org/10.1093/gji/ggv011

Huang, H. H., Lin, F. C., Schmandt, B., Farrell, J., Smith, R. B., & Tsai, V. C. (2015). The Yellowstone magmatic system from the mantle plume to the upper crust. *Science, 348*, 773–776. https://doi.org/10.1126/science.aaa5648

Huang, T. Y., Gung, Y., Kuo, B. Y., Chiao, L. Y., & Chen, Y. N. (2015). Layered deformation in the Taiwan orogeny. *Science, 349*(6249)*,* 720–72. https://doi.org/10.1126/science.aab1879

Huang, T. Y., Gung, Y., Liang, W. T., Chiao, L. Y., & Teng, L. S. (2012). Broad-band Rayleigh wave tomography of Taiwan and its implications on gravity anomalies. *Geophysical Research Letters, 39,* L05305.
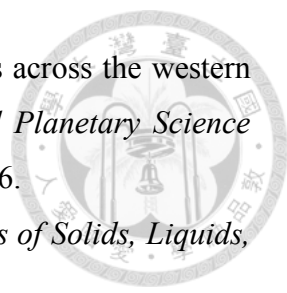
https://doi.org/10.1029/2011GL050727

Huang, Z., Zhao, D., & Wang, L. (2011a). Shear wave anisotropy in the crust, mantle wedge, and subducting Pacific slab under northeast Japan. *Geochemistry, Geophysics, Geosystems, 12,* Q01002, https://doi.org/10.1029/2010GC003343

Huang, Z., Zhao, D., & Wang, L. (2011b). Frequency-dependent shear-wave splitting and multilayer anisotropy in Northeast Japan. *Geophysical Research Letters, 38,* L08302. https://doi.org/10.1029/2011GL046804.

Huber, C., Townsend, M., Degruyter, W., Bachmann, O. (2019). Optimal depth of subvolcanic magma chamber growth controlled by volatiles and crust rheology. *Nature Geoscience, 12*, 762–768. https://doi.org/10.1038/s41561-019-0415-6.

Huber, C., Bachmann, O., Manga, M. (2009). Homogenization processes in silicic magma chambers by stirring and mushification (latent heat buffering). *Earth and Planetary Science Letters, 283* (1-4), 38-47. http://dx.doi.org/10.1016/j.epsl.2009.03.029.

Hung, S. H., Chen, W. P., and Chiao, L. Y. (2011). A data-adaptive, multiscale approach of finite-frequency, traveltime tomography with special reference to P and S wave data from central Tibet, *Journal Geophysical Research, 116*, B06307, doi:10.1029/2010JB008190.

Igarashi, T., Iidaka, T., Miyabayashi, S. (2011). Crustal structure in the Japanese Islands inferred from receiver function analysis. *Journal of the Seismological Society of Japan, 63*, 139–151. https://doi.org/10.4294/zisin.63.139 (in Japanese with English abstract).

Iidaka, T., Muto, J., Obara, K., Igarashi, T., & Shibazaki, B. (2013). Trench-parallel crustal anisotropy along the trench in the fore-arc region of Japan. *Geophysical Research Letters, 41*, 1957–1963. https://doi.org/10.1002/2013GL058359

Iinuma, T., Kato, T., & Hori, M. (2005). Inversion of GPS velocity and seismicity data to yield changes in stress in the Japanese Islands. *Geophysical Journal International, 160*, 417–434. https://doi.org/10.1111/j.1365-246X.2005.02513.x

Iwasaki, T., Levin, V., Nikulin, A., Iidaka, T. (2013). Constraints on the Moho in Japan and Kamchatka. *Tectonophysics, 609,* 184–201. https://doi.org/10.1016/j.tecto.2012.11.023.

Jackson, M. D., Blundy, J., Sparks, R. S. J. (2018). Chemical differentiation, cold storage and remobilization of magma in the Earth's crust. *Nature 564,* 405–409. https://
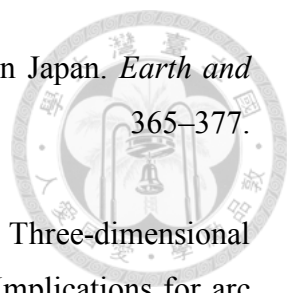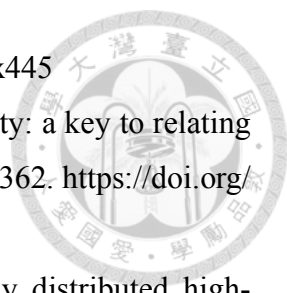
106

doi.org/10.1038/s41586-018-0746-2.

Janiszewski, H. A., Abers, G. A., Shillington, D. J., Calkins, J. A. (2013). Crustal structure along the Aleutian island arc: new insights from receiver functions constrained by active-source data. *Geochemistry, Geophysics, Geosystem, 14,* 2977–2992. https://doi. org/10.1002/ggge.20211.

Jolivet, L., Tamaki, K., & Fournier, M. (1994). Japan Sea, opening history and mechanism: A synthesis. *Journal of Geophysical Research, 99,* 22,237–22,259. https://doi.org/10.1029/93JB03463

Kaminski, É., & Ribe, N. M. (2002). Timescales for the evolution of seismic anisotropy in mantle flow. *Geochemistry, Geophysics, Geosystems, 3*(8). https://doi.org/10.1029/2001GC000222

Kaneko, S. (1966). Transcurrent displacement along the Median Line, southwestern Japan. *New Zealand Journal of Geology and Geophysics, 9,* 45–59. https://dx.doi.org/10.1080/00288306.1966.10420194

Kaneshima, S. (1990). Origin of crustal anisotropy: shear wave splitting studies in Japan. *Journal of Geophysical Research, 95,* 11,121-11,133.

Kaneshima, S., Ando, M., & Crampin, S. (1987). Shear-wave splitting above small earthquakes in the Kinki District of Japan. *Physics of the Earth and Planetary Interiors, 45,* 45–58. https://doi.org/10.1016/0031-9201(87)90196-8

Kano, K., Kato, H., Yanagisawa, Y., & Yoshida, F. (1991). Stratigraphy and geologic history of the Cenozoic of Japan. *Geological Survey of Japan Report, 274,* 114.

Karato, S., Jung, H., Katayama, I., & Skemer, P. A. (2008). Geodynamic significance of seismic anisotropy of the upper mantle: New insights from laboratory studies. *Annual Review of Earth and Planetary Sciences, 36,* 59–95. https://doi.org/10.1146/annurev.earth.36.031207.124120

Katayama, I., Hirauchi, K.-I., Michibayashi, K., & Ando, J.-I. (2009). Trench-parallel anisotropy produced by serpentine deformation in the hydrated mantle wedge. *Nature, 461,* 1114–1117. https://doi.org/10.1038/nature08513

Katsumata, A. (2010). Depth of the Moho discontinuity beneath the Japanese islands estimated by traveltime analysis. *Journal of Geophysical Research, 115,* B04303. https://doi.org/10.1029/2008JB005864

Kawakatsu, H., Watada, S. (2007). Seismic evidence for deep-water transportation in the mantle. *Science, 316* (5830), 1468–1471. https://doi.org/10.1126/science.

1140855.

Keith, C. M., Crampin, S. (1977). Seismic body waves in anisotropic media: synthetic seismograms. *Geophysical Journal of the Royal Astronomical Society, 49,* 225–243. https://doi.org/10.1111/j. 1365-246X.1977.tb03710.x.

Kennett, B. L. N. (1991). The removal of free surface interactions from three-component seismograms. *Geophysical Journal International, 104,* 153–163. https://doi.org/10.1111/j.1365- 246X.1991.tb02501.x.

Kiser, E., Palomeras, I., Levander, A., Zelt, C., Harder, S., Schmandt, B., Hansen, S., Creager, K., Ulberg, C. (2016). Magma reservoirs from the upper crust to the Moho inferred from high-resolution Vp and Vs models beneath Mount St. Helens, Washington State, USA. *Geology, 44* (6), G37591.1. https://doi.org/10.1130/ G37591.1.

Kiser, E., Levander, A., Zelt, C., Schmandt, B., Hansen, S. J. G. (2018). Focusing of melt near the top of the Mount St. Helens (USA) magma reservoir and its relationship to major volcanic eruptions. *Geology, 46,* 775–778. https://doi.org/10.1130/ G45140.1.

Ko, Y. T., Kuo, B. Y., & Hung, S. H. (2012). The southwestern edge of the Ryukyu subduction zone: a high *Q* mantle wedge. *Earth and Planetary Science Letters*, 335-336, 145-153. https://doi.org/10.1016/j.epsl.2012.04.041

Komatsu, M., Osanai, Y., Toyoshima, T., & Miyashita, S. (1989). Evolution of the Hidaka metamorphic belt, northern Japan. In J. S. Daly, R. A. Cliff, B. W. D. Yardley (Eds.), *Evolution of Metamorphic Belts* (Special Publication, 43, pp. 487–493). Geological Society, London. https://doi.org/10.1144/GSL.SP.1989.043.01.45

Koulakov, I., Abkadyrov, I., Al Arifi, N., Deev, E., Droznina, S., Gordeev, E. I., Jakovlev, A., El Khrepy, S., Kulakov, R. I., Kugaenko, Y. (2017). Three different types of plumbing systems beneath the neighboring active volcanoes of Tolbachik, Bezymianny and KlyucheVskoy in Kamchatka. *Journal of Geophysical Research, 122* (5). https:// doi.org/10.1002/2017JB014082.

Kuo, B. Y., & Wu, K. Y. (1997). Global shear velocity heterogeneities in the D" layer: Inversion from Sd-SKS differential travel times, *Journal of Geophysical Research, 102*, 11,775-11,788.

Lawson, C. L., & Hanson, R. J. (1974). *Solving least squares problems*. Englewood Cliffs: Prentice-Hall.

Lekic, V., Fischer, K. M. (2014). Contrasting lithospheric signatures across the western United States revealed by Sp receiver functions. *Earth and Planetary Science Letters, 402,* 90–98. https://doi.org/10.1016/j.epsl.2013.11.026.

Levy, M., Bass, H., Stern, R. (2000). *Handbook of Elastic Properties of Solids, Liquids, and Gases*, Four-Volume Set. Academic Press.

LeVshin, A. L., Yanocskaya, T. B., Lander, A. V., Bukchin, B. G., Barmin, M. P., Ratnikova, L. I., & Its, E. N. (1989). In V. I. Keilis-Borok (Eds.), *Seismic Surface Waves in a Laterally Inhomogeneous Earth*. Kluwer Academic, Norwell, Mass. https://doi.org/10.1007/978-94-009-0883-3_1

Ligorria, J. P., Ammon, C. J. (1999). Iterative deconvolution and receiver-function estimation. *Bulletin of the Seismological Society of America, 89,* 1395–1400.

Lin, S. C., & Kuo, B. Y. (2016). Dynamics of the opposite-verging subduction zones in the Taiwan region: Insights from numerical models. *Journal of Geophysical Research, Solid Earth, 121,* 2174–2192. https://doi.org/10.1002/2015JB012784

Liu, X., & Zhao, D. (2016). Backarc spreading and mantle wedge flow beneath the Japan Sea: insight from Rayleigh-wave anisotropic tomography. *Geophysical Journal International, 207,* 357–373. https://doi.org/10.1093/gji/ggw288

Matsubara, M., Sato, H., Uehira, K., Mochizuki, M., Kanazawa, T. (2017). Three dimensional seismic velocity structure beneath Japanese Islands and surroundings based on NIED seismic networks using both inland and offshore events. *Journal of Disaster Research, 12,* 844–857. https://doi.org/10.20965/jdr.2017.p0844.

Mardia, K. V., & Jupp, P. E. (2000). *Directional Statistics* (pp. 429). John Wiley, Hoboken, N. J. https://dx.doi.org/10.1002/9780470316979

Miyagi, I. (2007). Stratigraphy and volcanic activities of Hijiori volcano, Northeastern Japan arc (in Japanese with English abstract). *Bulletin of the Volcanological Society of Japan, 52*(6), 311–333. https://doi.org/10.18940/kazan.52.6_311

Miyagi, I., Kita, N., Morishita, Y. (2017). The geochemical and petrological characteristics of prenatal caldera volcano: a case of the newly formed small dacitic caldera, Hijiori, Northeast Japan. *Contributions to Mineralogy and Petrology, 172,* 79. https://doi. org/10.1007/s00410-017-1391-8.

Montagner, J.-P., & Nataf, H.-C. (1986). A simple method for inverting the azimuthal anisotropy of surface waves. *Journal of Geophysical Research, 91*(B1), 511–520.

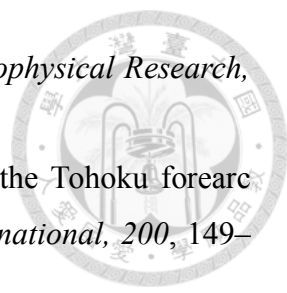Nakajima, J., & Hasegawa, A. (2004). Shear-wave polarization anisotropy and

subduction-induced flow in the mantle wedge of northeastern Japan. *Earth and Planetary Science Letters, 225,* 365–377. https://doi.org/10.1016/j.epsl.2004.06.011

Nakajima, J., Matsuzawa, T., Hasegawa, A., & Zhao, D. (2001). Three-dimensional structure of Vp, Vs, and Vp/Vs beneath northeastern Japan: Implications for arc magmatism and fluids. *Journal of Geophysical Research, 106,* 21, 843–21, 857. https://doi.org/10.1029/2000JB000008

Nakajima, J., Matsuzawa, T., & Hasegawa, A. (2002). Moho depth variation in the central part of northeastern Japan estimated from reflected and converted waves. *Physics of the Earth and Planetary Interiors, 130,* 31–47. https://https://doi.org/10.1016/S0031-9201(01)00307-7

Nakajima, J., Shimizu, J., Hori, S., & Hasegawa, A. (2006). Shear-wave splitting beneath the southwestern Kurile arc and northeastern Japan arc: A new insight into mantle return flow. *Geophysical Research Letters, 33,* L05305. https://doi.org/10.1029/2005GL025053

Nakamichi, H., Tanaka, S., Hamaguchi, H. (2002). Fine S wave velocity structure beneath Iwate volcano, northeastern Japan, as derived from receiver functions and travel times. *Journal of Volcanology and Geothermal Research, 116,* 235–255. https://doi.org/10.1016/ S0377-0273(02)00218-4.

Nakata, N., & Snieder, R. (2012). Estimating near-surface shear wave velocities in Japan by applying seismic interferometry to KiK-net data. *Journal of Geophysical Research, 117,* B01308. https://doi.org/10.1029/2011JB008595

Nishida, K., Kawakatsu, H., & Obara, K. (2008). Three-dimensional crustal S wave velocity structure in Japan using microseismic data recorded by Hi-net tiltmeters. *Journal of Geophysical Research, 113,* B10302. https://doi.org/10.1029/2007JB005395

Nishimoto, S., Ishikawa, M., Arima, M., Yoshida, T., Nakajima, J. (2008). Simultaneous high P-T measurements of ultrasonic compressional and shear wave velocities in Ichinomegata mafic xenoliths: their bearings on seismic velocity perturbations in lower crust of Northeast Japan arc. *Journal of Geophysical Research, 113,* B12212. https:// doi.org/10.1029/2008JB005587.

Niu, X., Zhao, D., & Li, J. (2018). Precise relocation of low-frequency earthquakes in Northeast Japan: new insight into arc magma and fluids. *Geophysical Journal*

International, 212, 1183-1200. https://doi.org/10.1093/gji/ggx445

Nur, A., Mavko, G., Dvorkin, J., Galmudi, D. (1998). Critical porosity: a key to relating physical properties to porosity in rocks. Lead. *Edge, 17,* 357–362. https://doi.org/10.1190/1.1437977.

Obara, K., Kasahara, K., Hori, S., & Okada, Y. (2005). A densely distributed high-sensitivity seismograph network in Japan: Hi-net by National Research Institute for Earth Science and Disaster Prevention. *Review of Scientific Instruments, 76,* 021301. https://doi.org/10.1063/1.1854197

Okada, S., & Ikeda, Y. (2012). Quantifying crustal extension and shortening in the back-arc region of Northeastern Japan. *Journal of Geophysical Research, 117,* B01404. https://doi.org/10.1029/2011JB008355

Ozawa, K., Shibata, K., & Uchiumi, S. (1988). K-Ar ages of hornblende in gabbroic rocks from the Miyamori ultramafic complex of the Kitakami Mountains. *Journal of Mineralogy, Petrology and Economic Geology, 83,* 150–159. https://doi.org/10.2465/ganko.83.150

Pandey, S., Yuan, X., Debayle, E., Tilmann, F., Priestley, K., & Li, X. (2015). Depth-variant azimuthal anisotropy in Tibet revealed by surface wave tomography. *Geophysical Research Letters, 42,* 4326–4334. https://doi.org/10.1002/2015GL063921

Park, S., Ishii, M. (2018). Near-surface compressional and shear wave speeds constrained by body-wave polarisation analysis. *Geophysical Journal International, 213,* 1559–1571. https://doi.org/10.1093/gji/ggy072.

Park, S., Tsai, V. C., Ishii, M. (2019). Frequency-dependent P wave polarization and its subwavelength near-surface depth sensitivity. *Geophysical Research Letters, 46,* 14,377–14,384. https://doi.org/10.1029/2019GL084892.

Porritt, R. W., Yoshioka, S. (2017). Evidence of dynamic crustal deformation in Tohoku, Japan, from time-varying receiver functions. *Tectonics, 36,* 1934–1946. https://doi.org/10.1002/2016TC004413.

Ray, T. W., & Anderson, D. L. (1994). Spherical disharmonics in the earth sciences and the spatial solution: Ridges, hotspots, slabs, geochemistry and tomography corrections. *Journal of Geophysical Research, 99,* 9605–9614. https://doi.org/10.1029/94JB00340

Ribe, N. M. (1992). On the relation between seismic anisotropy and finite strain. *Journal*

of Geophysical Research, 97(B6), 8737–8747. https://doi.org/10.1029/92JB00551

Saito, M. (1988). DISPER80: A subroutine package for the calculation of seismic normal mode solutions. In D. J. Doornbos (Ed.), *Seismological Algorithms: Computational Methods and Computer Programs*, 293–319. New York: Academic Press.

Schulte-Pelkum, V., Mahan, K. (2014). A method for mapping crustal deformation and anisotropy with receiver functions and first results from USArray. *Earth and Planetary Science Letters, 402,* 221–233. https://doi.org/10.1016/j.epsl.2014.01.050.

Seats, K. J., Lawrence, J. F., & Prieto, G. A. (2011). Improved ambient noise correlation functions using Welch's methods. *Geophysical Journal International, 188*, 513–523. https://doi:10.1111/j.1365-246X.2011. 05263.X

Shapiro, N. M., Campillo, M., Stehly, L., & Ritzwoller, M. H. (2005). High-resolution surface-wave tomography from ambient seismic noise. *Science, 307*(5715), 1615–1618. https://doi.org/10.1126/science.1108339

Smith, M. L., & Dahlen, F. A. (1973). Azimuthal dependence of Love and Rayleigh wave propagation in a slightly anisotropic medium. *Journal of Geophysical Research, 78*(17), 3321–3333. https://doi.org/10.1029/JB078i017p03321.

Sparks, R. S. J., Annen, C., Blundy, J. D., Cashman, K. V., Rust, A. C., Jackson, M. D. (2019). Formation and dynamics of magma reservoirs. *Philosophical Transactions of the Royal Society, A 377* (2139). https://doi.org/10.1098/rsta.2018.0019.

Sweldens, W. (1996). The lifting scheme: Accustom-design construction of biorthogonal wavelets, *Applied and Computational Harmonic Analysis 3,* 186-200. https://doi.org/10.1006/acha.1996.0015

Taira, A. (2001). Tectonic evolution of the Japanese island arc system. *Annual Review of Earth and Planetary Sciences, 29*, 109–134. https://doi.org/10.1146/annurev.earth.29.1.109

Tamura, Y., Tatsumi, Y., Zhao, D., Kido, Y., & Shukuno, H. (2002). Hot fingers in the mantle wedge: new insights into magma genesis in subduction zones. *Earth Planetary Science Letters, 197,* 105–116. https://doi.org/10.1016/S0012-821X(02)00465-X

Tatham, D. J., Lloyd, G. E., Butler, R. W. H., & Casey, M. (2008). Amphibole and lower

crustal seismic properties. *Earth Planetary Science Letters, 267,* 118-128. https://doi.org/10.1016/j.epsl.2007.11.042

Ueno, H., Hatakeyama. S., Aketagawa. T., Funasaki. J., & Hamada, N. (2002). Improvement of hypocenter determination procedures in the Japan Meteorological Agency (in Japanese with English abstract). *Quarterly Journal of Seismology, 65,* 123–134.

Umeda, K., Ban, M., Hayashi, S., & Kusano, T. (2013). Tectonic shortening and coeval volcanism during the Quaternary, Northeast Japan arc. *Journal of Earth System Science, 122,* 137–147. https://doi.org/10.1007/s12040-012-0245-z

Van der Molen, I., Paterson, M. S. (1979). Experimental deformation of partially- melted granite. *Contributions to Mineralogy and Petrology, 70,* 299–318. https://doi.org/10.1007/ BF00375359.

Wang, J., & Zhao, D. (2013). P-wave tomography for 3-D radial and azimuthal anisotropy of Tohoku and Kyushu subduction zones. *Geophysical Journal International, 193*, 1166–1181. https://doi.org/10.1093/gji/ggt086

Wang, K. L., Chung, S. L., O' Reilly, S. Y., Sun, S. S., Shinjo, R., & Chen, C. H. (2004). Geochemical constraints for the genesis of post-collisional magmatism and the geodynamic evolution of the northern Taiwan region. *Journal of Petrology, 45*, 975–1011. https://doi.org/10.1093/petrology/egh001

Ward, K., Zandt, G., Beck, S., Christensen, D., McFarlin, H. (2014). Seismic imaging of the magmatic underpinnings beneath the Altiplano–Puna volcanic complex from the joint inversion of surface wave dispersion and receiver functions. *Earth and Planetary Science Letters, 404*, 43–53. https://doi.org/10.1016/j.epsl.2014.07.022.

Xia, S., Zhao, D., Qiu, X., Nakajima, J., Matsuzawa, T., & Hasegawa, A. (2007). Mapping the crustal structure under active volcanoes in central Tohoku, Japan using P and PmP data. *Geophysical Research Letters, 34*, L10309. https://doi.org/10.1029/2007GL030026

Yang, T. Y., Chen, C. H., & Lee, T. (1992). Fission-track dating of Lutao volcanics: implications of partial annealing and eruption history. *Journal of the Geological Society of China, 35*, 19–42. https://doi.org/10.1016/0743-9547(94)00041-C

Yang, Y., Ritzwoller. M. H., Lin. F. C., Moschetti. M. P., & Shapiro, N. M. (2008). Structure of the crust and uppermost mantle beneath the Western United States revealed by ambient noise and earthquake tomography. *Journal of Geophysical*

Research, 113, B12, 1–9. https://doi.org/10.1029/2008JB005833

Yoshida, T., Kimura, J.-I., Yamada, R., Acocella, V., Sato, H., Zhao, D., Nakajima, J., Hasegawa, A., Okada, T., Honda, S., Ishikawa, M., Prima, O.D.A., Kudo, T., Shibazaki, B., Tanaka, A., Imaizumi, T. (2014). Evolution of late Cenozoic magmatism and the crust-mantle structure in the NE Japan Arc. *Geological Society, London, Special Publications, 385*, 335–387. https://doi.org/10.1144/SP385.15.

Yoshii, T., Asano, S. (1972). Time-term analyses of explosion seismic data. *Journal of Physics of the Earth, 20,* 47–58. https://doi.org/10.4294/jpe1952.20.47.

You, S. H., Gung, Y., Chiao, L. Y., Chen, Y. N., Lin, C. H., Liang, W. T., & Chen, Y. L. (2010). Multi-scale ambient noise tomography of short period Rayleigh waves across northern Taiwan. *Bulletin of the Seismological Society of America, 100*(6), 3165–3173. https://doi.org/10.1785/0120090394

Yu, X., Lee, C.-T. A., 2016. Critical porosity of melt segregation during crustal melting: constraints from zonation of peritectic garnets in a dacite volcano. *Earth and Planetary Science Letters, 449,* 127–134. https://doi.org/10.1016/j.epsl.2016.05.025.

Zellmer, G. F., & Annen, C. (2008). An introduction to magma dynamics. In C. Annen and G. F. Zellmer (Eds.), *Dynamics of Crustal Magma Transfer, Storage and Differentiation* (Special Publications 304, pp. 1-13) Geological Society, London. https://doi.org/10.1144/SP304.1

Zellmer, G. F., Chen, K. X., Gung, Y., Kuo, B. Y., Yoshida, T. (2019). Magma transfer processes in the NE Japan arc: insights from crustal ambient noise tomography combined with volcanic eruption records. *Frontiers in Earth Science, 7,* 40. https://doi.org/10.3389/feart.2019.00040.

Zellmer, G. F., Pistone, M., Iizuka, Y., Andrews, B. J., Gómez-Tuena, A., Straub, S. M., & Cottrell, E. (2016). Petrogenesis of antecryst-bearing arc basalts from the Trans-Mexican Volcanic Belt: Insights into along-arc variations in magma-mush ponding depths, H_2O contents, and surface heat flux. *American Mineralogist, 101*, 2405–2422. https://doi.org/10.2138/am-2016-5701

Zhang, S., & Karoto, S. I. (1995). Lattice preferred orientation of olivine aggregates deformed in simple shear. *Nature, 375*, 774–777. https://doi.org/doi:10.1038/375774a0

Zhao, D., Hasegawa, A., & Horiuchi, S. (1992). Tomographic imaging of P and S wave

velocity structure beneath northeastern Japan. *Journal of Geophysical Research, 97,* 19,909–19,928. https://doi.org/10.1029/92JB00603

Zhao, D., Kitagawa, H., & Toyokuni, G. (2015). A water wall in the Tohoku forearc causing large crustal earthquakes. *Geophysical Journal International, 200,* 149–172. https://doi.org/10.1093/gji/ggu381

Zhao, D., Matsuzawa, T., & Hasegawa, A. (1997). Morphology of the subducting slab boundary in the northeastern Japan arc. *Physics of the Earth and Planetary Interiors, 102,* 89–104. https://doi.org/10.1016/S0031-9201(96)03258-X

Zhao, D., Yanada, T., Hasegawa, A., Umino, N., & Wei, W. (2012). Imaging the subducting slabs and mantle upwelling under the Japan Islands. *Geophysical Journal International, 190,* 816-828. http://doi:10.1111/j.1365-246X.2012.05550.x